DEPOSITION OF AEROSOLS IN CYLINDRICAL TUBES AND IN HUMAN LUNG AIRWAYS

A Dissertation

presented to

the Faculty of the Graduate School

at the University of Missouri-Columbia

In Partial Fulfillment

of the Requirements for the Degree

Doctor of Philosophy

---

by

VEERA RAJESH GUTTI

Dr. Sudarshan K. Loyalka, Dissertation Supervisor

December 2010

The undersigned, appointed by the dean of the Graduate School, have examined the dissertation entitled

DEPOSITION OF AEROSOLS IN CYLIDRICAL TUBES

AND IN HUMAN LUNG AIRWAYS

presented by Veera Rajesh Gutti,

a candidate for the degree of doctor of philosophy of Nuclear Engineering,

and hereby certify that, in their opinion, it is worthy of acceptance.

Professor Sudarshan K. Loyalka

Professor Tushar K. Ghosh

Professor Mark A. Prelas

Professor Robert V. Tompson

Professor Dabir S. Viswanath

Professor Rajiv Dhand

Assistant Professor Yash Sethi

ACKNOWLEDGEMENTS

I am indebted to my thesis supervisor and advisor, Dr. Sudarshan Loyalka for his guidance and encouragement throughout the work on this thesis. I also would like to thank my committee members Dr. Robert Tompson and Dr. Tushar Ghosh for their substantial help and advice with experimental work in this research. I am also indebted to Profs. Mark Prelas, Dabir Viswanath and Rajiv Dhand for their advice and help and being on my thesis committee. I specially would like to thank my committee member Dr. Yash Sethi for his help in obtaining chest CT image data (deidentified) from University Hospitals at University of Missouri and his advice with the use of CT data.

I further would like to thank my dear wife Sunita Boddu for her love and support, my friends and family for their support and care for me through my doctoral program.

This research has been supported by Nuclear Energy Research Initiative (NERI-C; Grant # DE-FG07-07ID14892), Innovations in Nuclear Education and Infrastructure (INIE; Grant # DE-FG07-03ID14531), and Global Nuclear Energy Partnership (GNEP; Grant # DE-FG07-07ID14851) grants from the Department of Energy, and I am grateful for this support.

TABLE OF CONTENTS

LIST OF FIGURES

LIST OF TABLES

ABSTRACT

Aerosol transport and deposition is of interest in many industrial and medical applications. This research is focused on two specific topics: deposition of aerosols in cylindrical tubes with emphasis on thermophoresis and deposition in real human lung airways.

A numerical technique and a CFD code FLUENT are explored and used to estimate particle deposition efficiency due to thermophoresis in cylindrical tubes. Discrete phase modeling (DPM) employing Lagrangian particle tracking algorithm in CFD code FLUENT and user defined functions for thermophoretic force were used to predict the fate of the particles and found our results to be in good agreement with available experimental data. Further, limited experiments were conducted to measure the thermophoretic deposition efficiency of carbon nanoparticles in a cylindrical tube.

Real lung airway geometry for computational purposes was developed using Computed Tomography (CT) scan images of chest. Using image segmentation, volume rendering and surface processing tools in two commercially available software programs, the real lung airway surface geometry was extracted with good anatomical detail. Particle deposition was modeled using species transport and reaction modeling for molecular phase radioactive polonium-218 species in air. DPM model was also used to compute deposition of particles inhaled in the real lung airway geometry. The computational models used were verified against available experimental data for simpler single bifurcation geometries. Particle deposition efficiencies were computed using the DPM model for carbon nanoparticles of sizes 100 to 1000 nm.

CHAPTER 1

INTRODUCTION

Aerosols that originate from different sources not only influence various processes in nature, but have a variety of industrial applications. In nuclear industry, radioactive aerosols can originate from core disruptive accidents in fast reactors; accidents during nuclear material transport, or at waste disposal sites, while in health care industry, deposition of aerosol particles has important applications to inhalation aerosol therapy, inhalation toxicology and risk assessment. Understanding the phenomena of aerosol/particulate transport and deposition on surfaces is of particular interest in many such applications. In regard to deposition in primary coolant loops in advanced nuclear reactor designs, particle transport and deposition can be experimentally studied with ease in cylindrical tubes to compare with and verify computational models. For inhalation therapy and toxicology, flow in airways can be compared to flow in tubular structures for initial comparative studies.

In nuclear reactor cores, large amount of heat is released from fission reactions and large thermal gradients can exist near the walls of the reactor and of the primary cooling loops. Such large thermal gradients are also observed in other nuclear operations like nuclear waste management and nuclear material transportation. Thermophoretic force is the force experienced by an aerosol particle in the presence of a temperature gradient [1-9]. The phenomenon in which particles migrate in a temperature gradient under the influence of the thermophoretic force is called thermophoresis, and it is of

importance when high temperature gradients are present, for example in nuclear reactor accidents.

Because of the practical importance of thermophoresis, it has been the subject of extensive studies and applications over the years [1-9]. Particle deposition by thermophoresis has been identified as a working principal of many industrial processes such as fabricating optical wave guide in the chemical vapor deposition (CVD), designing thermal precipitators to remove micro-particles from gas stream, and also micro-contamination controlling in the semi-conductor industry [10]. On the negative side, particle deposition by thermophoresis causes undesirable effects on heat exchanger surfaces and turbine blades such as corrosion, fouling and erosion, which can reduce thermal conductivity of heat-exchanger pipes, production yield of specialty powders which are manufactured in high temperature aerosol reactors. Knowledge about particle transport due to combined convection, diffusion and thermophoresis in laminar or turbulent flows is of interest in applications such as the design of inhalation drugs [11], in aerosol measurement technologies where transport losses have to be controlled, and in nuclear power plants where particle emissions have to be avoided in case of an accident [6]. Further, the impact of thermophoresis on the transport of hot radioactive aerosols generated in a nuclear reactor accident has been recognized as an important factor in understanding reactor safety [5].

Thermophoretic deposition is of even greater significance in Pebble Bed Modular Reactors (PBMR's) where there is continual production of graphite dust in regular operation. To estimate particle deposition efficiencies for complicated geometries like PBMR, one needs to develop models using numerical techniques. It is difficult to conduct

experiments in real PBMR type reactors for particle deposition, as the costs and risks involved are very high. Numerical and computational models can provide insight into the nature of the problem with estimates on the deposition rates and efficiencies.

Aerosol inhalation by humans is mostly unavoidable, and may transport harmful material into the human body [11,12,13]. The respiratory tract serves both as a portal of entry for inhaled materials and as a target organ for effects produced by the inhaled materials. The respiratory tract is a complex and diverse system extending from the nose, down to the alveoli. Inhaled particles can be deposited in all the regions of the respiratory tract and can produce adverse effects depending on the toxicity and the nature of the particles. Deposition of airborne particles in human respiratory tract is governed largely by the aerodynamic and diffusion size characteristics of the particles. The site and magnitude of deposition of particles in the respiratory tract is determined by physical mechanisms and the lung airway anatomical geometry of the individual. The five most significant mechanisms of deposition are sedimentation, impaction, diffusion, interception, and electrostatic precipitation [12]. Deposition by sedimentation and impaction is a function of the inertial aerodynamic size characteristics of the aerosol particles. Deposition by diffusion is a function of the diffusional properties of the aerosol. Deposition by interception occurs when one of the edges of the particle touches the surface of the respiratory tract. Deposition of non-radioactive particles in the respiratory tract by electrostatic precipitation is usually negligible, because suspended particles in air are at equilibrium charge distribution, but charge distribution on radioactive particles is generally not in equilibrium and hence, electrostatic precipitation is important for studying the deposition of radioactive particles.

The breathing patterns of the individual also influence deposition and the two major determinants are the volume of air inhaled as determined by respiratory rate and tidal volume, and the dimensional characteristics of the respiratory tract. Breathing parameters (tidal volume, breathing frequency, minute ventilation, etc.) vary with the physical activity of the individual and also dictate the airflow regime. The airflow rate spans from 100 cm^3s^{-1} at rest to 2000 cm^3s^{-1} or higher for heavy exercise conditions. Breathing rate varies on average from 12 cycles at rest to 40 cycles per minute at exercise conditions. The particle size determines the dominant deposition mechanism, and the region where particles deposit in the respiratory tract. Total and regional deposition are modified further by other physical properties (density and shape) of the inhaled particles (for large particles), and the lung geometry (airspace dimensions).

The amount of mass deposited in the whole or specific regions of the lungs, i.e. the deposition distribution or local distributions (or hot spots signifying large local deposition) determine the occurrence of various lung disease types. Current lung deposition models [11-16,17-19,20] however implicitly assume that gases/particulates deposit uniformly on bronchial airway surfaces, which is equivalent to the assumption that all epithelial cells will receive the same average dose [13]. This assumption is not correct and it is important to estimate and experimentally verify the actual local deposition patterns so that the local doses can be accurately estimated. Such knowledge of the distribution of deposition in the airways also has important practical applications in cancer risk assessment [14-16], in the design of radiopharmaceutical aerosols and nanoparticles as inhalation drugs.

Lung airway models can be used to estimate particulate deposition and patterns. Though several early morphological models were based on symmetric, dichotomously bifurcating systems, [21,22] lung images obtained by CT-based imaging showed that such symmetrical models lack anatomical realism [17]. The detailed anatomical features of the upper respiratory tract like cartilaginous rings [18], and in particular repeating bifurcations trigger turbulence at much lower Re numbers [19]. The anatomy of the tracheobronchial tree is characterized by a three-dimensional asymmetric branching pattern. Therefore, realistic models are preferred over idealized isolated airway bifurcation models [20,23,24,25]. Airflow not only depends strongly on the geometry of the airways but also is intrinsically time-dependent. As a consequence the flow is extremely complex. Use of real lung airway geometry is important for estimation of aerosol deposition efficiency, risk estimation from inhalation of toxic particles, radiation dose from inhaled radioactive particles, and local deposition patterns. The CT-based morphological model could be used as a foundation for accurate computational fluid dynamics simulation of airway flow, particle transport, and particle deposition. Such research would allow us to study the fate of inhaled particles with a wide variety of particle(s) sizes and breathing conditions. Such modeling efforts have potential use in the study of inhaled pollutants and development of aerosol therapies. In addition, the morphological model would facilitate the development of methods for validating computational fluid dynamics studies with CT-based image data.

Idealized and unrealistic models (symmetric and asymmetric) of airways are used by most researchers to study aerosol transport and deposition in lungs. Due to the complexity of the lung airway geometry and variable breathing patterns, it has been

difficult for many researchers to develop accurate lung model morphologically and also deposition models due to complex breathing aerodynamics. The following factors are important to consider for aerosol transport and deposition modeling in human airways.

a) Real airway geometries
b) Oscillatory air flow in a breathing cycle.
c) Expansion and contraction of lungs during the breathing cycle.
d) Inclusion of moisture in the breathing air and moisture in lung airways.
e) Particle resuspension from the lung airway surfaces.

Further, in the design of inhalation drugs, current particle deposition models used are not accurate, as they do not consider the effects of localized particle deposition. While estimating internal radiation dose due to inhalation of radioactive particles, ICRP [12] considers the dose to be uniformly distributed in the airways, which is incorrect. Lung dose models have to be revised, for correct estimation of radiation dose for an average lung (as defined in ICRP).

Scope and Organization

This dissertation is organized as two separate topics i.e. thermophoretic particle deposition in cylindrical tubes and computations of particle deposition in lung airways. Although the two topics of interest are explored in different contexts, the underlying physics and computations have common features.

The first purpose of this research is to explore a numerical technique which appears promising and use of a CFD program to estimate deposition efficiency of particles due to thermophoresis. Results obtained from these methods are compared with some experimental data. A general purpose CFD code FLUENT (Ansys Inc.) was

extensively used to compute thermophoretic deposition efficiencies simulating certain experimental conditions. For the purpose of verification of the computational methods, limited experiments were conducted to study thermophoretic deposition and measure deposition efficiencies in cylindrical tubes.

The second objective of this research was to develop and use real lung airway geometry for estimation of aerosol/particulate deposition efficiency, and local deposition patterns in human lung airways. To achieve this objective, simple geometries for airway bifurcations were first considered to develop particle deposition models. The deposition models are verified against previous experimental data and further used for real human airway geometries. In this research work, deposition models were developed methods that can provide more accurate predictions for aerosol/particle deposition in human airways, which includes methods to reconstruct airway geometries from chest CT data. This would be very helpful in inhalation toxicology studies and design of inhalation therapeutic drugs. This work can be complimented with some experiments by constructing airway model geometries similar to those used in computations and measuring the particle size distributions at inlet and outlets of the airway geometries.

In the second chapter of the dissertation, previous work on thermophoresis and thermophoretic deposition was reviewed. In the third chapter, the methods and results on the present research on thermophoretic deposition are discussed. In the fourth chapter, the available literature on deposition of aerosols/particles in lung airway bifurcations was reiviewed. In the fifth chapter, computational model used for particle deposition was discussed and results for deposition in simple lung airway bifurcation geometries were presented. In the sixth chapter, methods and procedures employed are discussed to obtain

real lung airway geometry from chest CT image data and computations for particle deposition and results. Chapter seven summarizes the results and discusses the conclusions obtained from this research work, and scope of continuing this work for future research.

CHAPTER 2

PREVIOUS WORK ON THERMOPHORETIC DEPOSITION

2.1 Review of Literature

For a non-isothermal system in which the bounding surfaces are relatively cool, thermophoresis generally causes aerosol particles to move towards the surface and deposit. With respect to the calculation of the thermophoretic deposition, one needs to first know the thermophoretic force on a single particle in the gaseous stream, and then have a reliable means for solving the relevant equations of heat and mass transfer (the Navier-Stokes equations).

The first problem i.e., 'thermophoretic force on a single particle' requires solutions of the Boltzmann equation corresponding to thermophoresis problem for the molecular distribution, and single particle experiments to verify the computational results [5,26,27]. Brock [7,28] reported an approximate expression based on the BGK model and use of slip coefficients, and later it was adjusted for the coefficient values by Talbot et al. (1980). These works have been reviewed in Loyalka [26], who also solved numerically the linearized Boltzmann equation (for a rigid sphere gas) for the thermophoretic force. Li and Davis [27] have verified some of Loyalka's results experimentally by using an electrodynamic balance and have found good agreement, but there remains a need for further theoretical and experimental work on the problem.

The second problem, where one assumes that the thermophoretic force is known, requires solving the coupled Navier-Stokes equation with particle transport equation. Stratmann and Fissan [29] described the particle transport in a cooled laminar tube flow due to convection, diffusion, and thermophoresis. Montassier et al. [30,31] experimentally studied aerosol particle deposition in laminar tube flows and proposed correlations following experimental data to predict thermophoretic deposition of submicron and micron-sized particles in an infinitely long tube. He and Ahmadi [32] developed a numerical simulation procedure for studying deposition of aerosol particles in duct flows including the effect of thermal force under laminar and turbulent flow conditions. Shimada et al. [33] reported the nanometer-sized aerosol particle deposition and evaporation in heated pipe flows. Ye et al. [34] used the SIMPLER algorithm to solve the coupled Navier-Stokes, energy and convection-diffusion equation to obtain the velocity, temperature and concentration fields.

It has to be noted that in nuclear codes such as MELCOR, CONTAIN, and VICTORIA, there are concerns with respect to both of the above issues. [35-37] First, the expression of Brock [7,28] has been used, and second, a heat and mass transfer analogy is used for the deposition rate (as based on the Brock expression). This analogy is not valid as there is a double-boundary-layer structure (as opposed to a single layer in the standard heat transfer problem). Thus, careful attention to the numerics is needed even if the thermophoretic expression is fully correct.

Theoretical expression for thermophoretic deposition efficiency calculations used in published literature by some authors is summarized in Table 2.1. There is a need to compute thermophoretic deposition efficiencies in complicated geometries (for example,

pebble bed modular reactors), and it is of interest to have reliable numerical techniques and experimental database. Gutti and Loyalka [38] explored a numerical technique and CFD code FLUENT to estimate thermophoretic deposition efficiency in cylindrical tubes.

Table 2.1 Theoretical expressions for thermophoretic deposition efficiencies from published literature

Byers and Calvert [39]	$\eta_L = 1 - \exp\left(-\frac{\rho C_P f \,\mathrm{Re}\, K\nu}{4dh} \frac{\left(T_{in} - T_w\right)}{\overline{T}} \left(1 - \exp\left(-\frac{4hL}{u_m \rho C_P d} \right) \right) \right)$
Nishio, Kitani & Takahashi [40]	$\eta_L = 1 - \exp\left(-\frac{\rho C_P K \nu \left(T_{in} - T_w\right)}{k_g \overline{T}} \left(1 - \exp\left(-\frac{4hL}{u_m \rho C_P d} \right) \right) \right)$
Walker, Homsy & Geyling [41]	$\eta_\infty = \mathrm{Pr}\, K \frac{\left(T_{in} - T_w\right)}{T_w}$
Batchelor and Shen [42]	$\eta_\infty = \mathrm{Pr}\, K \frac{\left(T_{in} - T_w\right)}{T_{in}} \left(1 + \left(1 - \mathrm{Pr}\, K\right) \frac{\left(T_{in} - T_w\right)}{T_{in}} \right)$
Stratmann, Otto & Fissan [43] (Laminar)	$\eta_\infty = 1 - \exp\left(-0.845 \left(\frac{\mathrm{Pr}\, K + 0.025}{T_w / \left(T_{in} - T_w\right) + 0.28} \right)^{0.932} \right)$
Romay, Takagaki, Pui & Liu [44] (turbulent flow)	$\eta_L = 1 - \left(\frac{T_w + \left(T_{in} - T_w\right) \exp\left(-\pi dhL / \rho Q C_P\right)}{T_{in}} \right)^{\mathrm{Pr}\, K}$
Lin and Tsai [45]	$\eta_\infty = 0.783 \left(\mathrm{Pr}\, K \frac{\left(T_{in} - T_w\right)}{T_w} \right)^{0.94}$
Housiadas and Drossinos [46]	$\eta_\infty = 1 - \left(\frac{T_w}{T_{in}} \right)^{\mathrm{Pr}\, K}$

ρ gas density

ν gas kinematic viscosity

η deposition efficiency

η_L deposition efficiency for pipe length L.

η_∞ deposition efficiency for large pipe lengths where the gas temperature approaches wall temperature

C_p	gas specific heat at constant pressure
d	cylindrical pipe diameter
f	friction factor
h	convective heat transfer coefficient
k_g	thermal conductivity of gas
K	thermophoretic coefficient
L	pipe length
Pr	Prandtl number
Q	volumetric flow rate
Re	Reynolds number
T	temperature
$\overline{T}$	average temperature
T_{in}	gas temperature at entrance/inlet to cooling pipe
T_w	wall temperature
u_m	average flow velocity (radially averaged)

CHAPTER 3

THERMOPHORETIC DEPOSITION IN CYLINDRICAL TUBES

3.1 Thermophoretic deposition: Numerical Method

To verify the numerical solution method employed, the Graetz problem was solved for temperature distribution numerically and compare against the analytical solution. The particle transport equation (with convection, diffusion and thermophoresis) coupled with the energy transport equation (Graetz problem) was solved numerically for the particle concentration and thus particle deposition efficiency. Results obtained here are analyzed and compared with published results in the literature.

It is assumed that the particles enter the tube with a uniform particle concentration n_{in} and temperature T_{in}. The wall temperature of the tube also remains at T_{in} until laminar incompressible flow is fully established. At this axial location (x = 0), the wall temperature decreases to T_w and is kept at T_w. Our purpose is to determine the particle concentration distribution, and more specifically the local as well as the global particle deposition on the tube surface. In this problem cylindrical symmetry is assumed with fully established laminar flow, the velocity profile in the axial direction is considered known:

$$u_x(r) = U\left(1 - \frac{r^2}{R^2}\right)$$

where $u_x(r)$ is the velocity at any radius r, U is the maximum velocity at the cylindrical axis (r = 0) in the direction of flow, and R is the radius of the cylinder.

If the inertial motion of the particle is not large compared to the motion induced by convective gas flow or diffusion and temperature gradients, and external forces, then to develop basic correlations for the deposition currents and deposition rates, one considers the steady state or time averaged continuity equation for particle concentration [5]

$$\nabla \bullet \left(\mathbf{J}_{\mathrm{c}} + \mathbf{J}_{\mathrm{d}} + \mathbf{J}_{\mathrm{T}} \right) = 0 \tag{1}$$

where $\mathbf{J}_{\mathrm{c}}$ is particle current due to convection, $\mathbf{J}_{\mathrm{d}}$ is particle current due to diffusion and $\mathbf{J}_{\mathrm{T}}$ is particle current due to thermophoresis. Further

$$\mathbf{J}_{\mathrm{c}} = n(r,x)\ u_x(r)$$

$$\mathbf{J}_{\mathrm{d}} = -D\ \nabla n(r,x)$$

$$\mathbf{J}_{\mathrm{T}} = -\left(K \frac{\nu}{T(r,x)} \nabla T(r,x) \right) n(r,x)$$

where $n(r,x)$ is the particle concentration, D is the particle diffusion coefficient, ν is kinematic viscosity of the gas, and K is a dimensionless coefficient (also known as the thermophoretic coefficient i.e. same as K_{th}) which is a function of several parameters (particle radius, thermal conductivity, gas properties, gas-surface interaction, etc.).

Eq. (1) can be written as

$$U\left(1 - \frac{r^2}{R^2}\right) \frac{\partial n(r,x)}{\partial x} - D\ \nabla^2 n(r,x) - \nabla \bullet \left(n(r,x) \frac{K\nu}{T(r,x)} \nabla T(r,x) \right) = 0 \tag{2}$$

with the boundary conditions

$$n(r,0) = n_{in} \qquad T(r,0) = T_{in} \qquad T(R,x) = T_w$$

The temperature $T(r,x)$ in the above equation can be obtained by solving the heat transport equation:

$$\nabla \bullet \mathbf{J}_{\mathrm{q}} = 0 \tag{3}$$

where $\mathbf{J}_{\mathrm{q}}$ is the heat current due to heat conduction and convection, and can be written as

$$\mathbf{J}_{\mathrm{q}} = -k\nabla \mathrm{T}(r,x) + \rho c_p \, u_x(r) \; \mathrm{T}(r,x)$$

where ρ, c_p and k are mass density, specific heat capacity and thermal conductivity respectively of the gas.

Equation (3) can be written as

$$-k\frac{1}{r}\frac{\partial}{\partial r}\left(r\frac{\partial T(r,x)}{\partial r}\right) + \rho c_p u_x(r)\frac{\partial T(r,x)}{\partial x} = 0 \tag{4}$$

with the boundary conditions $T(r,0) = T_{in}$, $T(R,x) = T_w$

Equation (4) is the well known Graetz problem which can be solved analytically (series expansion) as well as numerically.

Equations (2) & (4) can be solved numerically for the particle concentration and hence the penetration and deposition efficiencies. This can be done in two ways

(a) Solve the equation for temperature i.e. Eq (4) and substitute the solution for temperature $\mathrm{T}(r,x)$ in Eq. (2) and solve for $n(r,x)$

(b) Solve both Eq. (2) and Eq. (4) simultaneously using numerical techniques.

Equations (2) and (4) can be non-dimensionalized by introducing certain dimensionless quantities $\hat{r}$, $\hat{n}$, $\hat{x}$, $\hat{t}$ and $\hat{T}^*$

$$\hat{r}=\frac{r}{R} \qquad \hat{n}=\frac{n}{n_{in}} \qquad \hat{x}=\frac{x}{R} \qquad \hat{T}\left(r,x\right)=\frac{T\left(r,x\right)-T_w}{T_{in}-T_w} \qquad \hat{T}^*\left(x\right)=\frac{T_w}{T_{in}-T_w}$$

and obtain

$$\begin{aligned}\left(1-\hat{r}^2\right)\frac{\partial\hat{n}\left(\hat{r},\hat{x}\right)}{\partial\hat{x}}-\frac{\mathrm{Pr}}{\mathrm{Pe_{th}}}\frac{1}{\mathrm{Sc}}\left(\frac{1}{\hat{r}}\frac{\partial}{\partial\hat{r}}\left(\hat{r}\frac{\partial\hat{n}\left(\hat{r},\hat{x}\right)}{\partial\hat{r}}\right)\right)\\ -\frac{K\ \mathrm{Pr}}{\mathrm{Pe_{th}}}\frac{1}{\hat{r}}\frac{\partial}{\partial\hat{r}}\left(\hat{r}\left(\frac{1}{\hat{T}\left(\hat{r},\hat{x}\right)+\hat{T}^*\left(\hat{x}\right)}\frac{\partial\hat{T}\left(\hat{r},\hat{x}\right)}{\partial\hat{r}}\right)\hat{n}\right)=0\end{aligned} \tag{5}$$

$$\frac{1}{\hat{r}}\frac{\partial}{\partial\hat{r}}\left(\hat{r}\frac{\partial\hat{T}\left(\hat{r},\hat{x}\right)}{\partial\hat{r}}\right)-\left(\mathrm{Re\,Pr}\right)\left(1-\hat{r}^2\right)\frac{\partial\hat{T}\left(\hat{r},\hat{x}\right)}{\partial\hat{x}}=0 \tag{6}$$

with the boundary conditions

$$\hat{n}\left(\hat{r},0\right)=1 \qquad \hat{T}\left(\hat{r},0\right)=1 \qquad \hat{T}\left(1,\hat{x}\right)=0$$

where Re is the Reynolds number, $\mathrm{Pe_{th}}$ is the thermal Peclet number, Pr is the Prandtl number ν/α, and Sc is the Schmidt number ν/D. The form of Eq. (5) makes it clear that the relative importance of diffusion to thermophoresis is governed by the non-dimensionalized parameters.

Thermophoretic particle deposition efficiency $\eta\left(x\right)$ is given by

$$\eta\left(\hat{x}\right)=1-\frac{\int_0^1 d\hat{r}\ \hat{r}\ v_x\left(\hat{r}\right)\hat{n}\left(\hat{r},x\right)}{\int_0^1 d\hat{r}\ \hat{r}\ v_x\left(\hat{r}\right)\hat{n}\left(\hat{r},0\right)} \tag{7}$$

The boundary layer theory analyses show that in a short tube the thermophoretic particle deposition efficiency η is approximately expressed as [5].

$$\eta\left(\hat{x}\right)=4.07\frac{\mathrm{Pr}\,K}{1+\hat{T}^*\left(\hat{x}\right)}\left(\frac{\hat{x}}{\mathrm{Pe_{th}}}\right)^{2/3} \tag{8}$$

In general however, numerical techniques are required to obtain accurate results. Although some numerical results have been reported elsewhere [41,43,45,47], a different technique is explored in this work which is convenient to use and has led to results of high accuracy.

For the purposes of computations, it is convenient to rearrange Eqns. (5) and (6) as:

$$\frac{\partial \hat{n}\left(\hat{r},\hat{x}\right)}{\partial \hat{x}} = \frac{\mathrm{Pr}}{\mathrm{Pe}_{\mathrm{th}}}\frac{1}{\mathrm{Sc}}\frac{1}{\left(1-\hat{r}^2\right)}\left(\frac{1}{\hat{r}}\frac{\partial}{\partial \hat{r}}\left(\hat{r}\frac{\partial \hat{n}\left(\hat{r},x\right)}{\partial \hat{r}}\right)\right) - \frac{K\ \mathrm{Pr}}{\mathrm{Pe}_{\mathrm{th}}}\frac{1}{\left(1-\hat{r}^2\right)}\frac{1}{\hat{r}}\frac{\partial}{\partial \hat{r}}\left(\hat{r}\left(\frac{1}{\hat{T}\left(\hat{r},x\right)+\hat{T}^*\left(x\right)}\frac{\partial \hat{T}\left(\hat{r},x\right)}{\partial \hat{r}}\right)\hat{n}\right) \tag{9}$$

$$\frac{\partial \hat{T}\left(\hat{r},\hat{x}\right)}{\partial \hat{x}} = \frac{1}{\left(\mathrm{Re}\,\mathrm{Pr}\right)}\frac{1}{\left(1-\hat{r}^2\right)}\frac{1}{\hat{r}}\frac{\partial}{\partial \hat{r}}\left(\hat{r}\frac{\partial \hat{T}\left(\hat{r},x\right)}{\partial \hat{r}}\right) \tag{10}$$

In the numerical technique employed here, the partial differential equations are replaced by a system of coupled ordinary differential equations [48]. The radius of the pipe $\hat{r}$ is discretized into *N+1* parts where $\hat{r}_1$ is the first radial point off the axis, $\hat{r}_0$ is the axis and $\hat{r}_{N+1}$ is the wall. The discretization on $\hat{r}$ is written as

$\hat{r}_i = \hat{r}_{i-1} + \Delta\hat{r}_{i-1}$ and $\hat{r}_0 = 0$,

Let us define,

$$\left(\sigma_T\right)_i = \frac{\left(\hat{T}_i - \hat{T}_{i-1}\right)}{\Delta\hat{r}_{i-1}} \qquad \left(\sigma_n\right)_i = \frac{\left(n_i - n_{i-1}\right)}{\Delta\hat{r}_{i-1}} \qquad \left(\sigma_{th}\right)_i = \frac{\left(n_{i-1}\right)}{\hat{T}_{i-1}+\hat{T}^*}\frac{\left(\hat{T}_i - \hat{T}_{i-1}\right)}{\Delta\hat{r}_{i-1}}$$

In the discretization, the fact that derivative at r=0 is zero and a combination of backward and forward differences with radial points 0, 1, 2,…, *N+1* were used. The

Eqns. (9) and (10) are converted to a discretized system of non-linear ordinary differential equations:

$$\frac{dn_i}{dx} = \frac{1}{\hat{r}_i}\frac{1}{\left(1-\hat{r}_i^2\right)}\frac{\mathrm{Pr}}{\left(\mathrm{P\,e_{th}\,Sc}\right)}\left(\frac{\hat{r}_{i+1}\left(\sigma_n\right)_{i+1} - \hat{r}_i\left(\sigma_n\right)_i}{\left(\Delta\hat{r}_i + \Delta\hat{r}_{i-1}\right)/2}\right) +$$

$$\frac{1}{\hat{r}_i}\frac{1}{\left(1-\hat{r}_i^2\right)}\frac{\mathrm{Pr}}{\mathrm{P\,e_{th}}}K\left(\frac{\hat{r}_{i+1}\left(\sigma_{th}\right)_{i+1} - \hat{r}_i\left(\sigma_{th}\right)_i}{\left(\Delta\hat{r}_i + \Delta\hat{r}_{i-1}\right)/2}\right) \qquad \text{for i} \geq 2$$

$$= \frac{1}{\hat{r}_i}\frac{1}{\left(1-\hat{r}_i^2\right)}\frac{\mathrm{Pr}}{\left(\mathrm{P\,e_{th}\,Sc}\right)}\left(\frac{\hat{r}_1\left(n_2 - n_1\right)}{\Delta\hat{r}_1} - 0\right)/\Delta\hat{r}_0 \; +$$

$$\frac{1}{\hat{r}_i}\frac{1}{\left(1-\hat{r}_i^2\right)}\frac{\mathrm{Pr}}{\mathrm{P\,e_{th}}}K\left(\frac{\hat{r}_1\left(\hat{T}_2 - \hat{T}_1\right)}{\Delta\hat{r}_1}\frac{n_1}{\hat{T}_1 + \hat{T}^*} - 0\right)/\Delta\hat{r}_0 \qquad \text{for i =1} \qquad (11)$$

$$\frac{dT_i}{dx} = \frac{1}{\hat{r}_i}\frac{1}{\left(1-\hat{r}_i^2\right)}\frac{1}{\left(\mathrm{Re\,Pr}\right)}\left(\frac{\hat{r}_{i+1}\left(\sigma_T\right)_{i+1} - \hat{r}_i\left(\sigma_T\right)_i}{\left(\Delta\hat{r}_i + \Delta\hat{r}_{i-1}\right)/2}\right) \qquad \text{for i} \geq 2$$

$$= \frac{1}{\hat{r}_i}\frac{1}{\left(1-\hat{r}_i^2\right)}\frac{1}{\left(\mathrm{Re\,Pr}\right)}\left(\frac{\hat{r}_1\left(\hat{T}_2 - \hat{T}_1\right)}{\Delta\hat{r}_1} - 0\right)/\Delta\hat{r}_0 \qquad \text{for i =1} \qquad (12)$$

Both uniform and non-uniform discretization on $\hat{r}$ are explored, as choice of more grid points in the boundary layer region can reduce the computation time for similar accuracy as compared to the case of uniform discretization.

For uniform discretization

$$\Delta\hat{r}_i = 1/\left(N+1\right)$$

and for non-uniform discretization we have taken

$$\Delta\hat{r}_i = Radius \times \delta^i \times \left(\frac{1-\delta^{N+1}}{1-\delta}\right)^{-1}$$

Combination of different N and δ values were explored here. For N = 50, 100, 500, 1000, and 5000 the respective values for δ are 0.93, 0.965, 0.993, 0.9965, and 0.9993.

3.2 Results from Numerical Method

3.2.1 Verification against Series Solution

For the purpose of the verification of numerical method explored here, the Graetz problem is considered i.e. Eq. (10) for temperature distribution with the boundary conditions $\hat{T}(\hat{r},0)=1$ and $\hat{T}(1,\hat{x})=0$ for the case of RePr = 1. Analytical series solutions of this problem have been described previously in the literature [49-52]. Laguerre functions are used here, with 120 terms and precision of 40 digits and compare the solution obtained with the numerical solution for the temperature distribution. These results are tabulated in Table 3.1 and plotted as shown in Figure 3.1 (as is well known the series expansion is not very accurate at $\hat{x}$=0, as the convergence is slow and there is some oscillation). Temperature is plotted against the non-dimensionalized radius ($\hat{r}$) of the tube for various axial length ($\hat{x}$) positions of the cylindrical tube. The two sets of results are in very close agreement and provide confidence in the use of numerical technique for the computation of particle concentration distributions and thus particle deposition efficiencies.

Table 3.1 Verification of numerical solution with series solution for non-dimensionalized temperature distribution in the radial direction along the length of the tube for the Graetz energy problem

Numerical Solution of Graetz problem for non dimensionalized temperature $\hat{T}$ distribution for RePr = 1

$\hat{r}$ \ $\hat{x}$	***0.1***	***0.2***	***0.4***	***0.5***	***0.6***	***0.8***	***0.9***	***1***
0.1	0.689240	0.335552	0.077719	0.037398	0.017996	0.004167	0.002005	0.000965
0.2	0.654319	0.317498	0.073532	0.035383	0.017026	0.003942	0.001897	0.000913
0.3	0.598531	0.289035	0.066932	0.032207	0.015498	0.003589	0.001727	0.000831
0.4	0.525476	0.252381	0.058436	0.028119	0.013531	0.003133	0.001508	0.000725
0.5	0.439934	0.210202	0.048664	0.023417	0.011268	0.002609	0.001256	0.000604
0.6	0.347371	0.165266	0.038257	0.018409	0.008858	0.002051	0.000987	0.000475
0.7	0.253224	0.120112	0.027802	0.013378	0.006438	0.001491	0.000717	0.000345
0.8	0.162131	0.076772	0.017770	0.008551	0.004115	0.000953	0.000458	0.000221
0.9	0.077301	0.036579	0.008466	0.004074	0.001960	0.000454	0.000218	0.000105
1	0.000147	6.94E-05	1.61E-05	7.73E-06	3.72E-06	8.61E-07	4.14E-07	1.99E-07

Series Solution (Analytical) of Graetz problem for non-dimensionalized temperature $\hat{T}$ distribution for RePr = 1

$\hat{r}$ \ $\hat{x}$	***0.1***	***0.2***	***0.4***	***0.5***	***0.6***	***0.8***	***0.9***	***1***
0.1	0.689342	0.335647	0.077760	0.037422	0.018010	0.004171	0.002007	0.000966
0.2	0.654387	0.317571	0.073566	0.035404	0.017038	0.003946	0.001899	0.000914
0.3	0.598560	0.289084	0.066959	0.032225	0.015508	0.003592	0.001729	0.000832
0.4	0.525465	0.252404	0.058456	0.028132	0.013539	0.003136	0.001509	0.000726
0.5	0.439883	0.210200	0.048675	0.023425	0.011273	0.002611	0.001257	0.000605
0.6	0.347286	0.165242	0.038260	0.018413	0.008861	0.002052	0.000988	0.000475
0.7	0.253112	0.120071	0.027799	0.013379	0.006438	0.001491	0.000718	0.000345
0.8	0.162000	0.076718	0.017761	0.008548	0.004114	0.000953	0.000459	0.000221
0.9	0.077159	0.036515	0.008454	0.004068	0.001958	0.000453	0.000218	0.000105
1	0	0	0	0	0	0	0	0

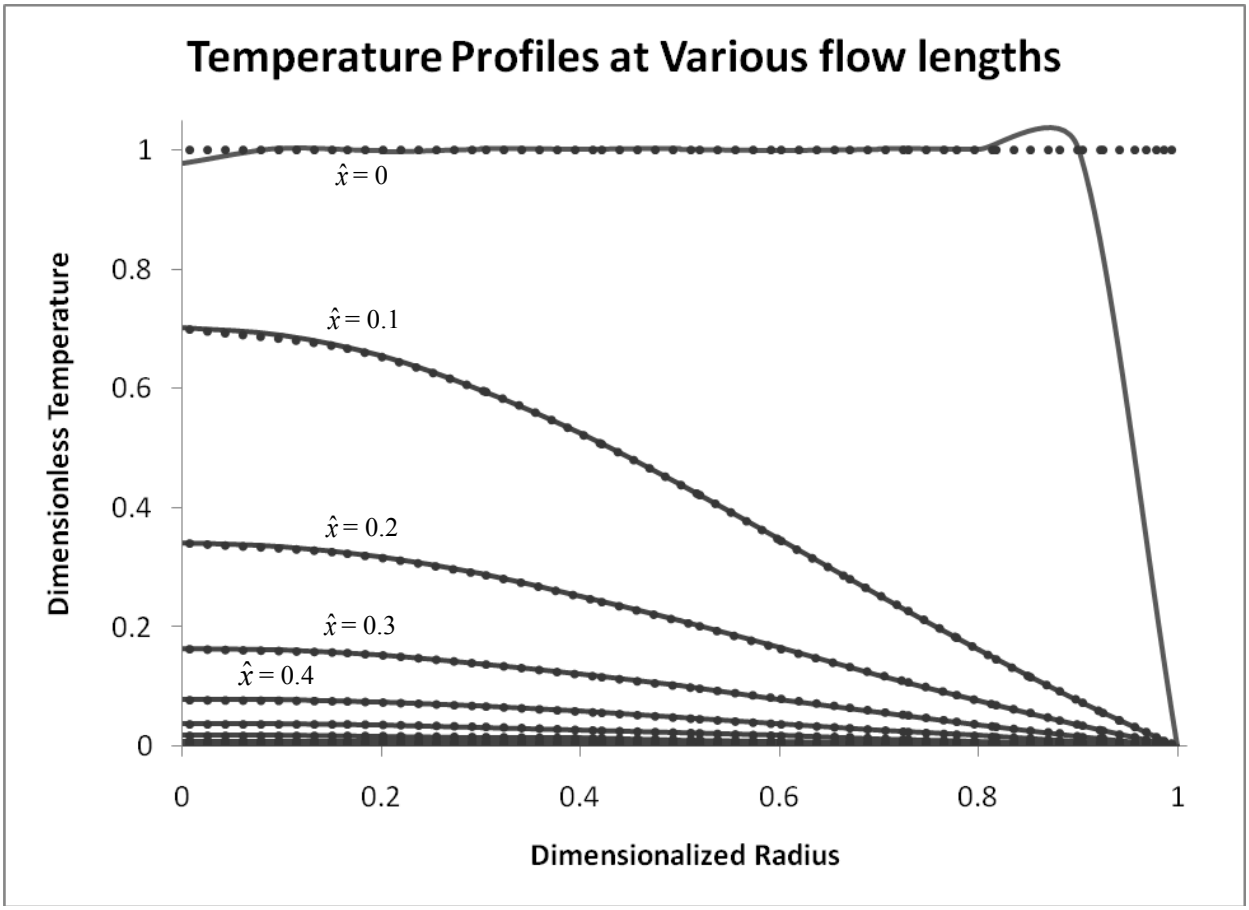

Figure 3.1: Comparison of series solution (solid curves) and numerical solution (dotted curves) for the temperature profiles for various lengths along the flow direction of the cylindrical tube for the case of RePr = 1. The tube length here is the non-dimensionalized length ($\hat{x}$ = *x*/R)

3.2.2 Parametric Studies & Further Verification

As can be seen from Eq. (11), particle transport due to combined convection, diffusion and thermophoresis depends on the dimensionless numbers Pe_{th}, Pr, Re, Sc, and *K*. Considering the case with RePr = 1, Pr*K* = 1 and Sc=10^4, the results obtained for the particle deposition efficiencies at various lengths ($\hat{x}$) of the cylindrical tube are summarized in Table 3.2 and Table 3.3. In Table 3.2 the numerical results are obtained for uniform discretization on $\hat{r}$ with different values of *N* ranging from 50 to 5000.

Table 3.2 Thermophoretic deposition efficiency $\eta(\hat{x})$ with RePr = 1; and for particles with PrK = 1; and Sc = 10^4 in a cylindrical tube of radius = 1 (non-dimensionalized radius) with uniform discretization on $\hat{r}$

$\hat{x}$	***Short-tube Eq. (8)***	***Present Work***						
		N = 50	N = 100	N = 500	N = 1000	N = 2000	N = 4000	N = 5000
0.00001	0.0011807	0.000979	0.001120	0.0011636	0.0011647	0.0011648	0.0011648	0.0011648
0.0001	0.0054803	0.005172	0.005295	0.0053267	0.0053264	0.0053259	0.0053255	0.0053254
0.0005	0.0160246	0.015168	0.015256	0.0152601	0.0152564	0.0152542	0.015253	0.0152527
0.001	0.0254375	0.023868	0.023924	0.0239044	0.0238977	0.023894	0.023892	0.0238917
0.01	0.118070	0.102834	0.102603	0.102362	0.102328	0.102310	0.102302	0.102300
0.1	0.548034	0.379816	0.378840	0.377925	0.377802	0.377740	0.377709	0.377703
0.2	0.869950	0.508143	0.507244	0.506335	0.506209	0.506145	0.506113	0.506106

Table 3.3 Thermophoretic deposition efficiency $\eta(\hat{x})$ with RePr = 1; and for particles with PrK = 1; and Sc = 10^4 in a cylindrical tube of radius = 1 (non-dimensionalized radius) with non-uniform discretization on $\hat{r}$ as a geometric series with the common ratio as mentioned

$\hat{x}$	***Short-tube Eq. (8)***	***Present Method***						
		N = 50	N = 100	N = 500	N = 1000	N = 2000	N = 4000	N = 5000
		$\delta = 0.93$	$\delta = 0.965$	$\delta = 0.993$	$\delta = 0.9965$	$\delta = 0.9982$	$\delta = 0.9991$	$\delta = 0.9993$
0.00001	0.0011807	0.0011649	0.0011649	0.00116488	0.00116484	0.00116481	0.00116480	0.00116480
0.0001	0.0054803	0.0053341	0.0053288	0.0053257	0.00532542	0.00532525	0.00532517	0.00532515
0.0005	0.0160246	0.0152897	0.0152666	0.0152543	0.0152530	0.0152523	0.0152520	0.0152520
0.001	0.0254375	0.0239543	0.0239168	0.0238947	0.0238923	0.0238912	0.0238906	0.0238905
0.01	0.118070	0.102737	0.102488	0.102328	0.102310	0.102302	0.102297	0.102296
0.1	0.548034	0.377269	0.378189	0.377909	0.377802	0.377743	0.377711	0.377704
0.2	0.869950	0.504009	0.506301	0.506351	0.506230	0.506160	0.506121	0.506113

Numerical results for deposition efficiency obtained for large values of N in Table 3.2 are in good agreement with the expression for deposition in short tube i.e. Eq. (8) for small values of the $\hat{x}$. In Table 3.3, the results are obtained for the non-uniform discretization on $\hat{r}$, where more points are selected near the wall boundary compared to the axial center of the tube. Non-uniform discretization on $\hat{r}$ has reduced the computational time greatly in the sense that good accuracy is obtained for the deposition efficiencies for values of N as small as 100 for discretization on $\hat{r}$.

Analytical results for the thermophoretic deposition efficiency in short and long tubes have been previously reported as function of a non-dimensionalized of parameters by several authors [31,41-44,47]. These expressions for deposition efficiency are tabulated in Table 3.3. These formulas are based on the assumption that the wall temperature is constant and the flow at the entrance is fully developed. Deposition efficiencies as $\hat{x} \to \infty$, η_∞ from different equations from previous literature along with the deposition efficiencies from numerical solutions were plotted for different values of $\hat{T}^*$ as shown in Figure 3.2. Here PrK was taken as 1 and Peclet number i.e. RePr was also taken as 1. The approximations proposed by Stratmann et.al. [43] and Batchelor & Shen [42] agree well with our numerical results.

Further, the dependence of deposition efficiency η on K was studied for different $\hat{T}^*$ values of 0.6, 1.0 and 3.0, with other parameters fixed, (we chose, RePr = 1, Sc = 10^4, and T_{wall} = 300 K). The variation in η with K is shown in Figure 3.3, where the dotted lines represent the data obtained from present work and the solid lines represent the approximate expressions for thermophoretic deposition efficiency by Batchelor & Shen [42] and Stratmann et.al. [43]. As the value of $\hat{T}^*$ increases, the deposition efficiency η

decreases with the dependence on *K* becoming more linear. From the present work, it was also observed for very short tubes (very short tube lengths); the deposition efficiency can be considered almost linear in *K*. It is clear still that for the case studied here, the two approximate expressions [36, 46] are quite good.

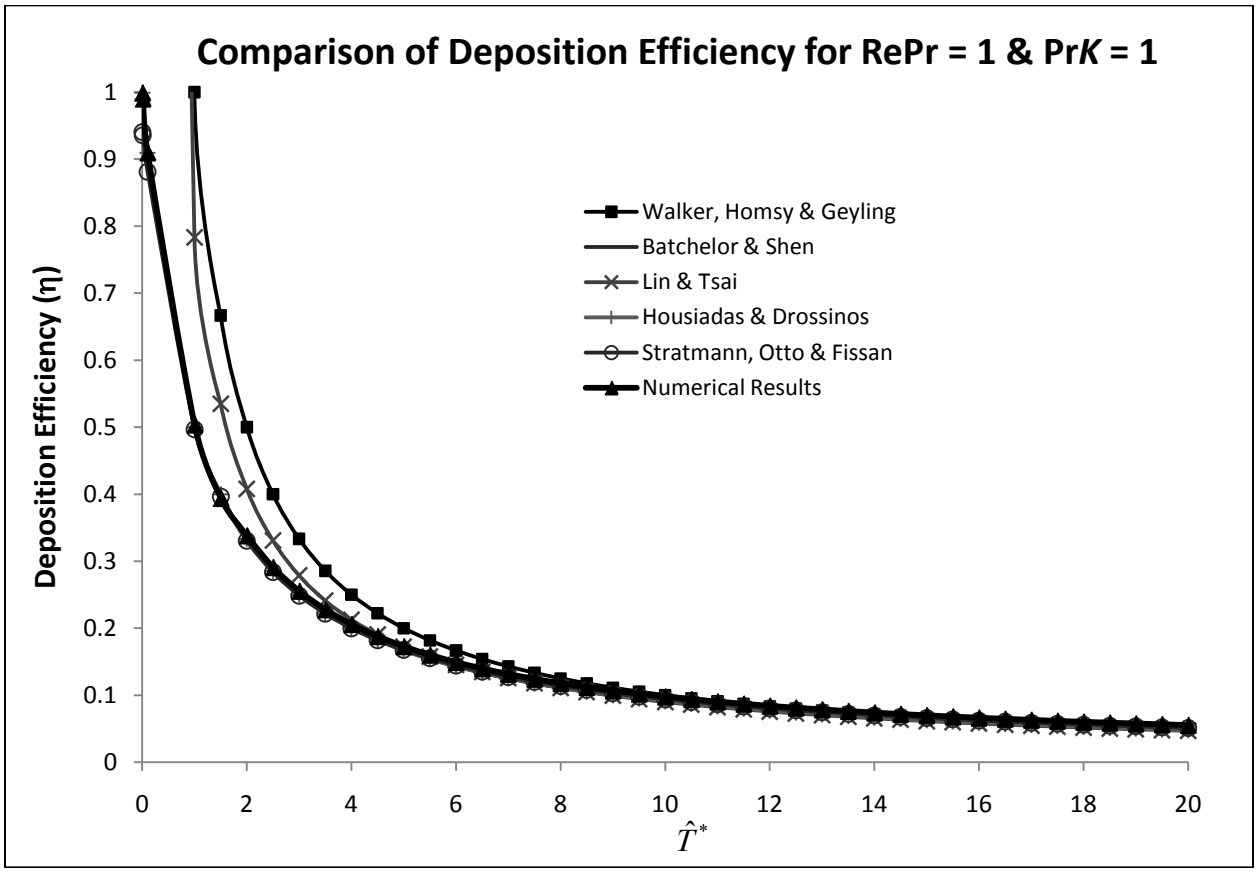

Figure 3.2: Comparison of deposition efficiency obtained from the present numerical method with the theoretical expressions from various authors [35,36,37,46,47] as a function of $\hat{T}^*$, with Pr*K* = 1 and RePr = 1

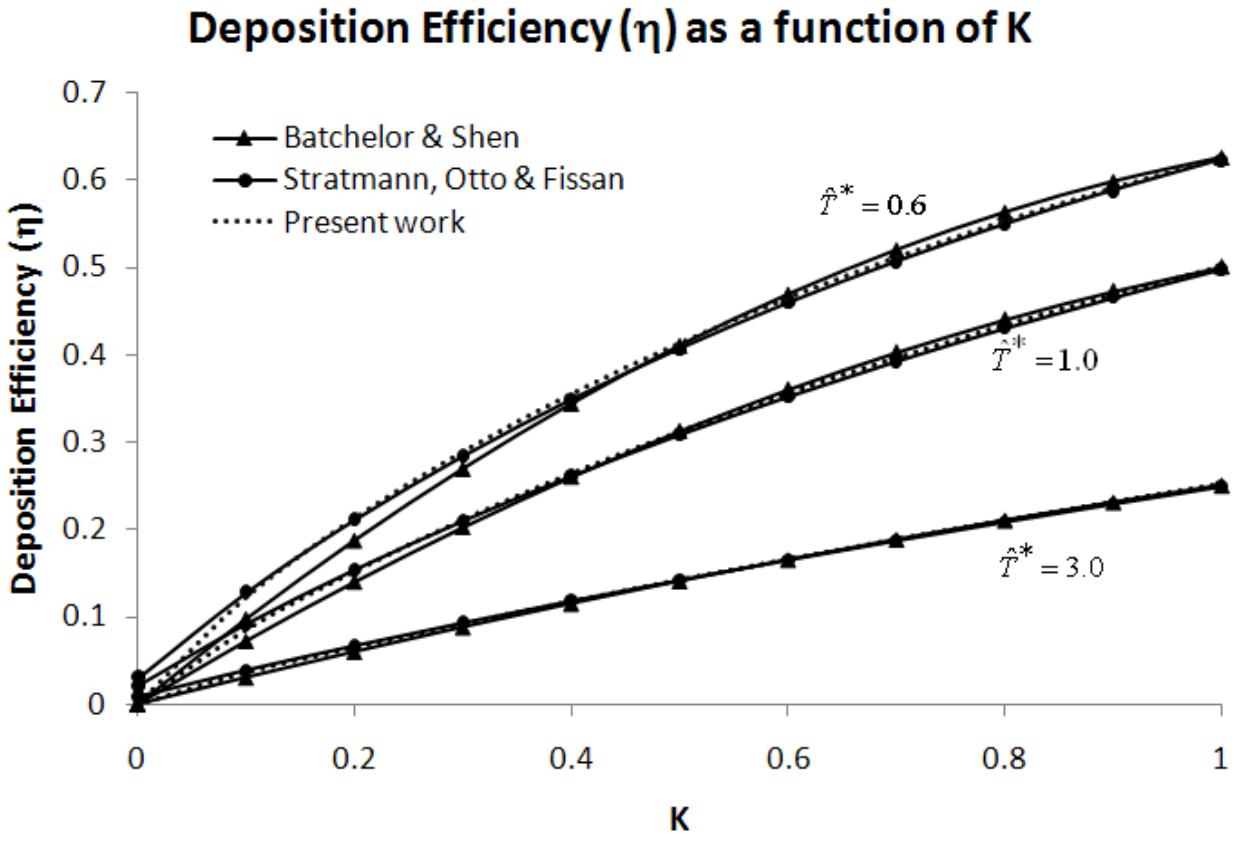

Figure 3.3: Dependence of deposition efficiency (η) as a function of *K* for different $\hat{T}^*$ with all the other parameters same where T_{wall} = 300 K, RePr = 1 and Sc = 10^4

3.2.3 Comparison with Experiments

To compare the numerical results for the deposition efficiencies with published experimental data, the work of Romay et al. [44] was considered. They obtained data for thermophoretic deposition efficiencies for NaCl particles, sizes (diameters) 100 nm and 482 nm, in a vertical cylindrical tube of diameter 0.49 cm and length 96.5 cm. The carrier gas considered was dry air with inlet temperatures 350, 370, 400 and 420 K for the NaCl particles of size 100 nm and with temperatures 335, 365, and 373 K for the NaCl particles of 482 nm. The inlet air flow condition corresponds to a Re = 1380 at 25 °C temperature

and 1 atm pressure. For these particle sizes, thermophoretic coefficient K was calculated using Brock's [7] (see also Talbot et.al. [53]) expression,

$$K = \frac{2C_s C_c}{\left(1+3C_m Kn\right)}\left(\frac{\left(k_g / k_p\right)+C_t Kn}{1+2\left(k_g / k_p\right)+2C_t Kn}\right)$$

where C_c = Cunningham correction factor $= 1 + Kn(1.257 + 0.4e^{-1.1/Kn})$

Kn = Knudsen number ($2\lambda/d_p$); λ = gas mean free path; d_p = particle diameter

k_g = Gas thermal conductivity

k_p = Particle thermal conductivity

C_s, C_t, and C_m are the slip and jump coefficients that depend on intermolecular and molecule-particle surface interactions (accommodation coefficients) [4]. Assuming the accommodation coefficients to be unity, and some assumptions with respect to intermolecular interactions, in this present work, the values of C_s, C_t, and C_m are taken as 1.47, 1.14 and 2.18 respectively. The expression is convenient and contains adjustable parameters and has been used (together with heat/mass transfer analogy which is not appropriate) in several nuclear codes (e.g. CONTAIN [54], MELCOR [55] and VICTORIA [56]), although other expressions should be more appropriate [26,27]. Air (gas) thermal conductivity k_g was calculated from the interpolation of air thermal conductivity data from the CRC handbook [57] as a function of temperature. Particle thermal conductivity k_p of 6 $Wm^{-1}K^{-1}$ was used. Molecular mean free path for air was obtained from the CRC handbook [57]. Calculated values of K corresponding to particle sizes 100 nm and 482 nm are 0.5227 and 0.4456 respectively. These values should not be regarded as the best possible values, but rather as only reasonable. The calculated deposition efficiencies are in close agreement with the available experimental data as

shown in Table 3.4. Also included in this table, are the values of the deposition efficiencies obtained from the expression of Stratmann et.al. [43].

Note that the linear dependence of η on K (with other parameters fixed) also allows one to calculate K from the experimentally measured data for efficiency. For example, consider the case with inlet air temperature T_{in} = 350 K and wall temperature T_w = 293 K, and corresponding $\hat{T}^*$ = 5.14. For the experimental deposition efficiency value of 7%, and from the linear inverse on computed results, the value of K = 0.579.

3.3 Computational Fluid Dynamics Model

In addition to the above work, a CFD code FLUENT was used to compute the deposition efficiencies due to thermophoresis. Computational Fluid Dynamics (CFD) is the science of predicting fluid flow, heat and mass transfer, chemical reactions, and related phenomena by solving numerically the set of governing mathematical equations (Conservation of mass, momentum, energy, species). Contained within the broad field of computational fluid dynamics are activities that cover the range from the automation of well-established engineering design methods to the use of detailed solutions of the Navier-Stokes equations as substitutes for experimental research into the nature of complex flows [58]. In short CFD analysis reduces the total effort required in experimental design and data acquisition. One such CFD code used in this research is FLUENT (Ansys Inc.), a general purpose CFD code which uses the finite volume method for discretizing the governing equations into a set of algebraic equations. The finite volume method uses the integral form of the conservation equations as its starting point. The solution domain is subdivided into a finite number of contiguous control volumes as shown in Figure 3.4, and the conservation equations are applied to each control volume.

As a result, one obtains an algebraic equation for each control volume. The finite volume method can accommodate any type of grid, so it is suitable for complex geometries.

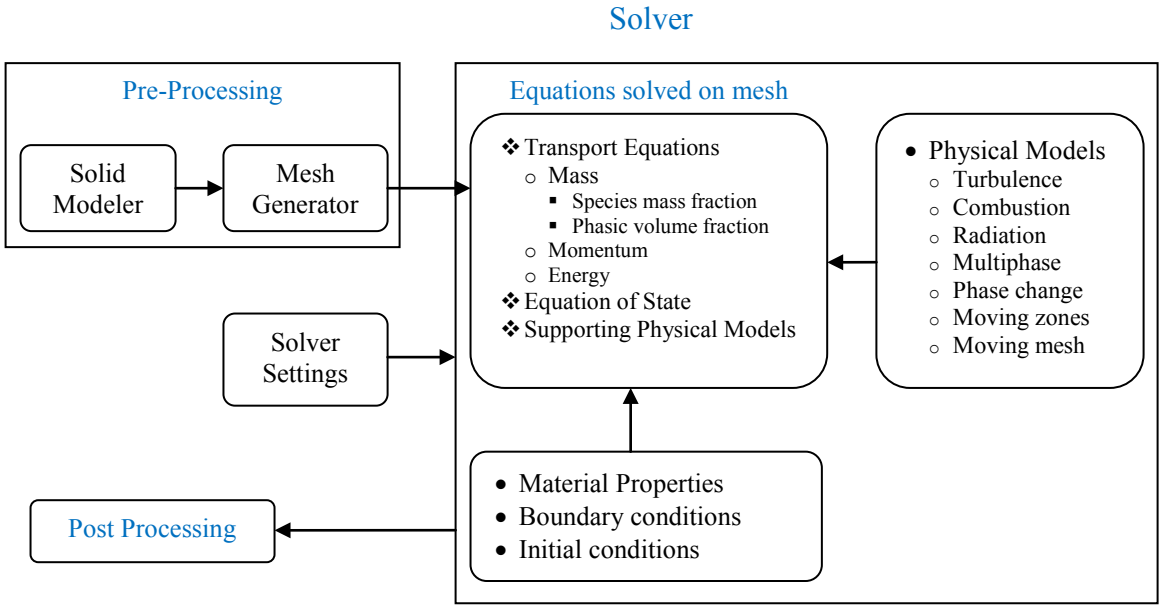

Figure 3.4: CFD modeling overview. Reproduced from FLUENT user guide.

The conditions and parameters corresponding to the above comparison with experimental work for laminar flows in cylindrical tubes were used for computations. Density, viscosity and thermal conductivity of air were defined using a user defined function as a function of temperature based on the interpolation functions obtained in Mathematica (Wolfram®) using published data for the properties of air. Fully developed velocity profile for a cylindrical tube was used as the inlet flow profile. Discrete phase model was used to model the particle flow and thermophoresis with the Brownian diffusion. The thermophoretic coefficient defined in Fluent code is different compared to K, and was redefined with a user defined function using the calculated K value. The cylindrical tube wall temperature was maintained at a constant temperature of 293 K in all cases of inlet temperatures. Four meshes (465,520, 899,160, 2,066,400, 7,029,360

volume cells respectively) were explored in our calculations. Two meshes, one fine and other very fine shown in Figure 3.5 are used for final computations and to report the results.

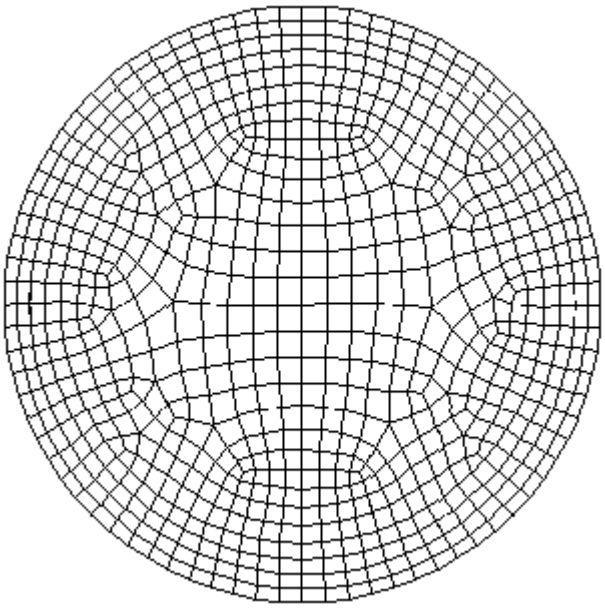

(a)

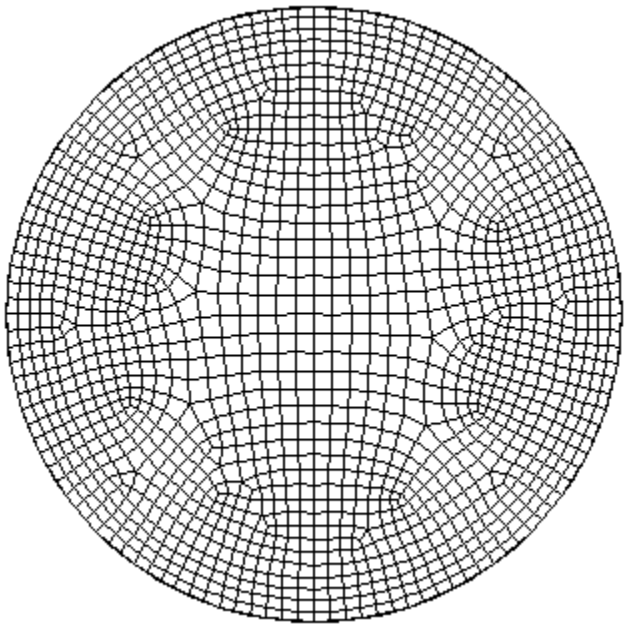

(b)

Figure 3.5: Grid resolution normal to the axis of the tube (0.49 cm dia.) (a) The grid used for the initial set of computations (b) Finer grid near the wall boundary.

Thermophoretic deposition efficiencies computed using the CFD code Fluent are presented in Table 3.4 and compare well with the published experimental data and the numerical data obtained here with some exceptions. For NaCl particles of 100 nm, the deposition efficiencies using fine mesh are very close to the numerical results for inlet temperatures 350 and 370 K. For inlet temperature of 400 K, the deposition efficiency computed was very much similar to that in case of 370 K inlet temperature. Further, for the inlet temperature of 420 K, no result was observed due to error messages during the CFD computation (have tried to decipher the error messages, but have not been able to resolve the situation in discussions with the Fluent developers). For NaCl particles of 482 nm, the deposition efficiencies computed were close to the numerical results in cases where the inlet temperatures were 365 K and 373 K. The deposition efficiency obtained for the case with inlet temperature of 335 K was very small compared to the numerical result as well as the experimental result. It appeared us that the resolution of the mesh near the wall surface (Figure 3.5(a)) was not sufficient enough for such a small temperature gradient compared to other cases, and had therefore explored here use of the finest mesh of 7,029,360 volumes (cells). The results obtained with the use of a fine (2,066,400 volumes) and very fine (7,029,360 volumes) meshes are reported in Table 3.4. Note that finer meshes do progressively improve the results (in some cases rather substantially), and the results converge. For the finer meshes, computational speed was a factor, and had used first a 4-node workstation computer and eventually a 128-node computer cluster.

Table 3.4 Comparison of deposition efficiency computed from numerical method and FLUENT with experimental data from Romay et al. [44] and an approximate expression by Stratmann et al. [43]

T_{in} (K)	Romay et al. [44] Expt. data	Stratmann et al. [43] expression (approximate)	Present Work		
			Numerical Solution of coupled ODE's	CFD code Fluent (mass %)	
				Mesh (a)*	Mesh (b)**
	NaCl aerosols of d_p = 0.1 μm at 5 l/min in 0.49 cm diameter tube				
350	7	7.08	6.27	7.27	7.29
370	10	9.12	8.21	8.36	8.43
400	11.8	11.91	10.93	8.6	9.08
420	12.8	13.62	12.6	--	11.5
	NaCl aerosols of d_p = 0.482 μm at 5 l/min in 0.49 cm diameter tube				
335	4.5	4.76	4.083	1.5	3.73
365	7.1	7.55	6.89	7.05	7.06
373	8.3	8.25	7.35	7.42	7.45

*Mesh (a): Fine mesh with 2,066,400 volume cells

3.4 Thermophoretic Particle Deposition Experiments

Experimental data is required to verify and validate computational models developed. An experiment was designed to study thermophoretic deposition of carbon nanoparticles with state of the art aerosol instrumentation to generate and measure size distribution of carbon nanoparticles. Because of the focus of the present work on computations, we have however, carried out experiments for only one set of measurements, and additional data would need to be acquired in the future.

3.4.1 Carbon Nanoparticle Generation

Carbon nanoparticles are generated using a spark aerosol generator GFG-1000 (Palas® GmBH). A schematic of the electrode arrangement in the spark aerosol generator is shown in Figure 3.6(b). The GFG-1000 was supplied with argon as a carrier gas. The GFG-1000 consists of two electrodes (material of interest for nanoparticles) separated by a 1.8 mm gap. One of the electrodes was connected to a high voltage (3000V) supply in parallel with a capacitor (20nF) [59]. Charge stored in capacitors is discharged across the gap at a set frequency which produces sparks across the electrode gap. Each electric spark locally evaporates the electrode material in the vicinity of the spark. This is followed by rapid cooling which occurs, initially, via adiabatic expansion and then, subsequently, by thermal conduction and convective heat transfer in the argon gas carrier ($5.0\ \mathrm{l.min^{-1}}$) which entrains the particles as it is focused through a narrow slit into the gap between the electrodes. These processes nucleate the evaporated material (atoms/ions) to very fine primary particles which further coagulate and grow via condensation, depending upon their concentrations and the argon gas flow rates, into larger nanoparticles of various sizes. The particle mass flow rate is adjustable over a wide range

by means of the spark frequency. The frequency of the electric sparks between the electrodes can be varied from 2 to 300 Hz. GFG-1000 can generate particles ranging from 5 - 150 nm size, with concentrations > 10^7 particles/cm^3, Argon gas as the primary carrier gas and optional compressed air/nitrogen as dilution gas.

(a)

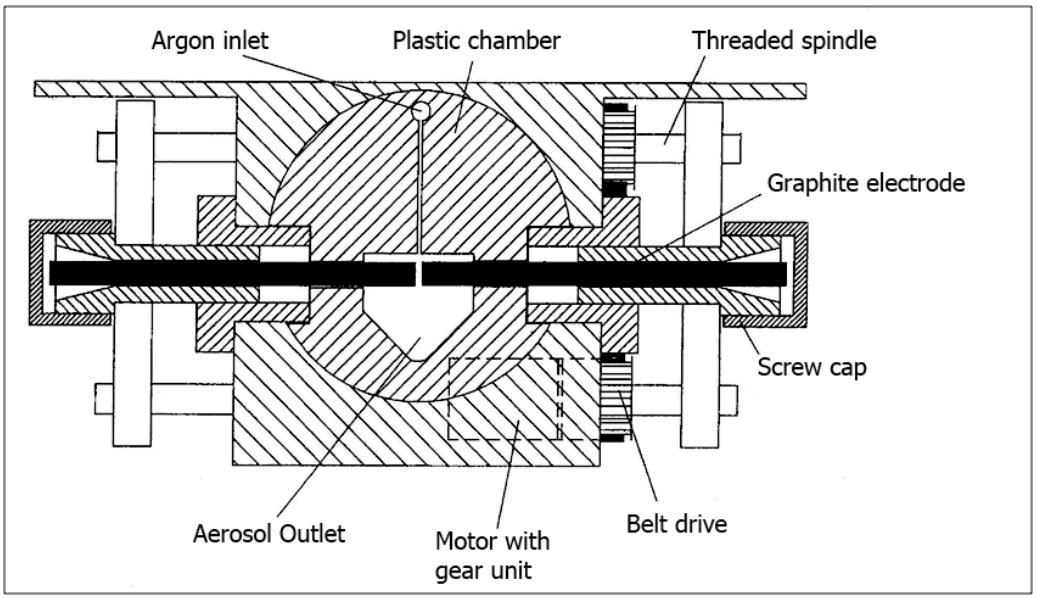

(b)

Figure 3.6: (a) GFG-1000 (Palas) used in this research (b) Schematic of the electrode arrangement in the spark aerosol generator (Palas, GFG-1000). The electrodes are maintained with a gap width of 1.8 mm by an inbuilt motor and gear unit.

3.4.2 Thermophoretic Deposition tube

Thermophoretic deposition tube was designed like a heat exchanger, with the deposition tube in the axial center of a larger diameter (1.5 inch) tube which acts like a cooling jacket. The thermophoretic deposition tube is shown in the Figure 3.7. Cold water circulating in the annulus of heat exchanger is maintained cooler temperature (~ 5 °C) relative to the particle stream, using a Fischer Scientific water chiller bath (Model 9101). The cooling water flow rate can be varied using a valve and a flowmeter with a maximum flow rate of 1.3 $l.min^{-1}$.

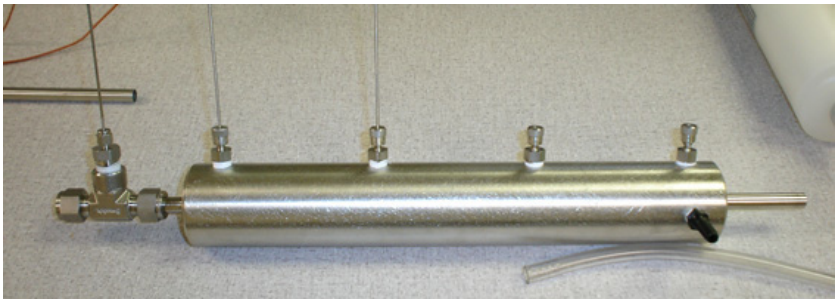

Figure 3.7: Thermophoresis deposition tube (3/8 inch diameter) at the axial center of the heat exchanger type design.

3.4.3 Scanning Mobility Particle Sizer (SMPS) Spectrometer

The SMPS system consists of an electrostatic classifier (TSI model 3080) included with a differential mobility analyzer (DMA, TSI model 3081), and an ultrafine condensation particle counter (CPC, TSI model 3776) with an upper limit of detectable concentration at 3×10^{5} $particles.cm^{-3}$. The purpose of the Electrostatic Classifier shown in Figure 3.8 [60] is to extract a known size fraction of aerosol nanoparticles from the incoming particle stream.

Figure 3.8: Electrostatic Classifier (Model 3080, TSI Inc.). Reprinted with permission from TSI publication ”Series 3080 Electrostatic Classifiers Operation and Service Manual.”

In the Electrostatic Classifier, the aerosol particles enter a neutralizer (Krypton-85 Bipolar charger) which exposes the aerosol particles to high concentrations of bipolar ions. See Figure 3.9 for illustration. The particles and ions undergo frequent collision due to the random thermal motion of the ions. The particles quickly reach a state of charge equilibrium, in which the particles carry a bipolar charge distribution. The charged aerosols pass from neutralizer into the main portion of the Diffusion mobility analyzer (DMA). The DMA contains two concentric metal cylinders. The polydisperse aerosol and sheath air are introduced at the top of the classifier and flow down the annular space between the cylinders. The aerosol surrounds the inner core of sheath air, and both flows pass down the annulus with no mixing of the two laminar streams. The inner cylinder or

the center rod is maintained at a controlled negative voltage, while the outer cylinder is electrically grounded. This creates an electric field gradient between the two cylinders.

The electric field causes positively charged particles to be attracted to the negatively charged center rod (see Figure 3.10). Particles are precipitated along the length of the center rod. The location of the precipitating particles depends on the particle electrical mobility z_p, the Classifier flow rate, and the Classifier geometry.

$$z_p\left(d_p, q\right) = \frac{qeC_c\left(d_p\right)}{3\pi\mu d_p}$$

where

$$C_c\left(d_p\right) \equiv \text{Cunningham Correction factor} = 1 + \frac{\lambda}{d_p}\left(2.514 + 0.8e^{\left(\frac{-0.55d_p}{\lambda}\right)}\right)$$

$d_p \equiv$ particle diameter (m)

$e \equiv$ elementary unit of charge $= 1.602 \times 10^{-19} C$

$q \equiv$ # of charges on the particle

$\hat{z}_p\left(d_p, q\right) \equiv$ electrical mobility of particle $(m^2.V^{-1}s^{-1})$

$\mu \equiv$ gas viscosity $(kg.m^{-1}s^{-1})$

Particles with a high electrical mobility are precipitated along the upper portion of the rod; particles with a low electrical mobility are collected on the lower portion of the rod. A schematic of the working principle of electrostatic classifier is shown in Figure 3.9. Particles within a narrow range of electrical mobility exit with the monodisperse air flow through a small slit located at the bottom of the center rod. These particles are transferred to Ultrafine Condensation Particle Counter to determine the particle concentration. The remaining particles are removed from the Classifier via the excess air flow.

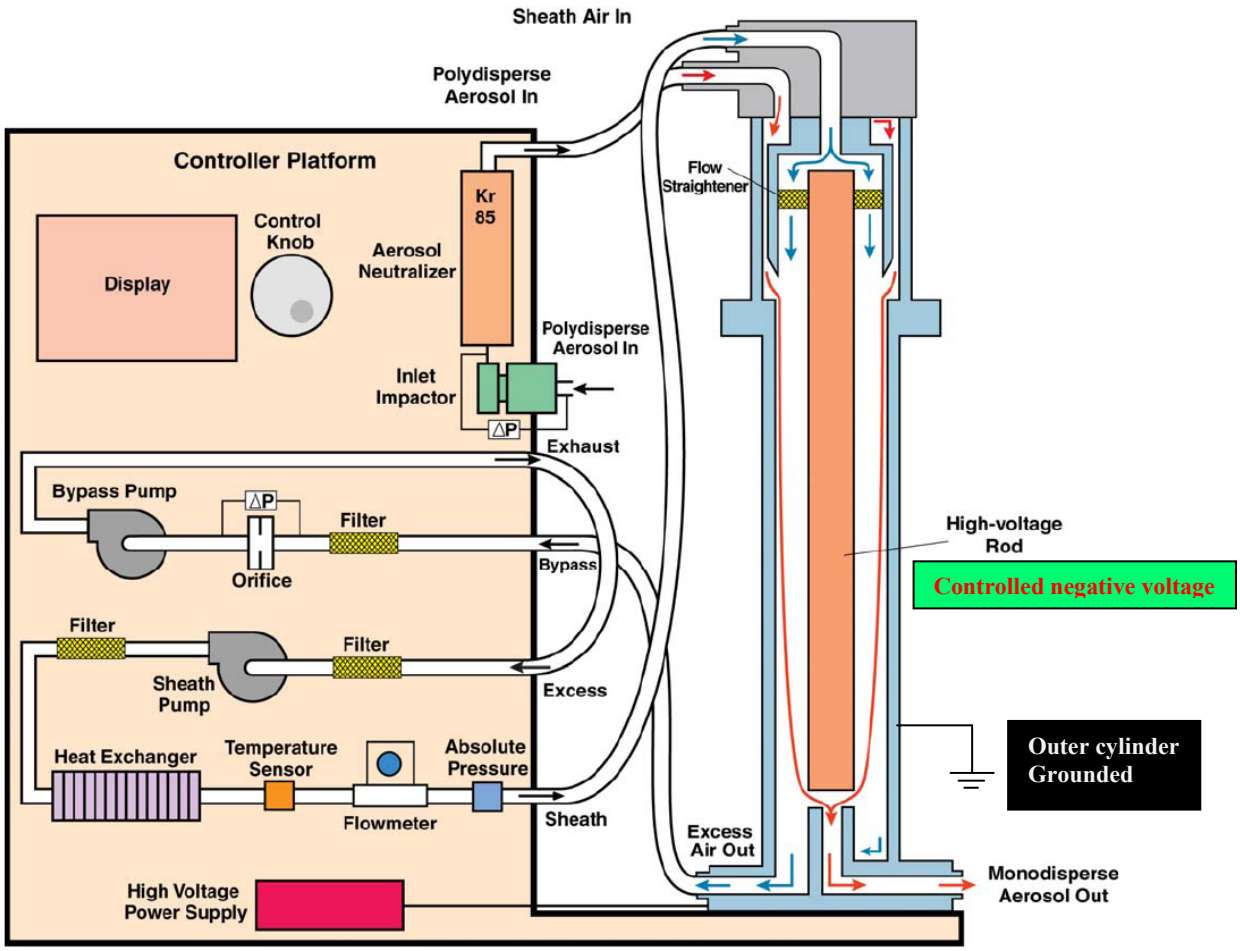

Figure 3.9: Schematic of the working of Electrostatic Classifier (Model 3080, TSI Inc.) Reprinted with permission from TSI publication ”Series 3080 Electrostatic Classifiers Operation and Service Manual.”

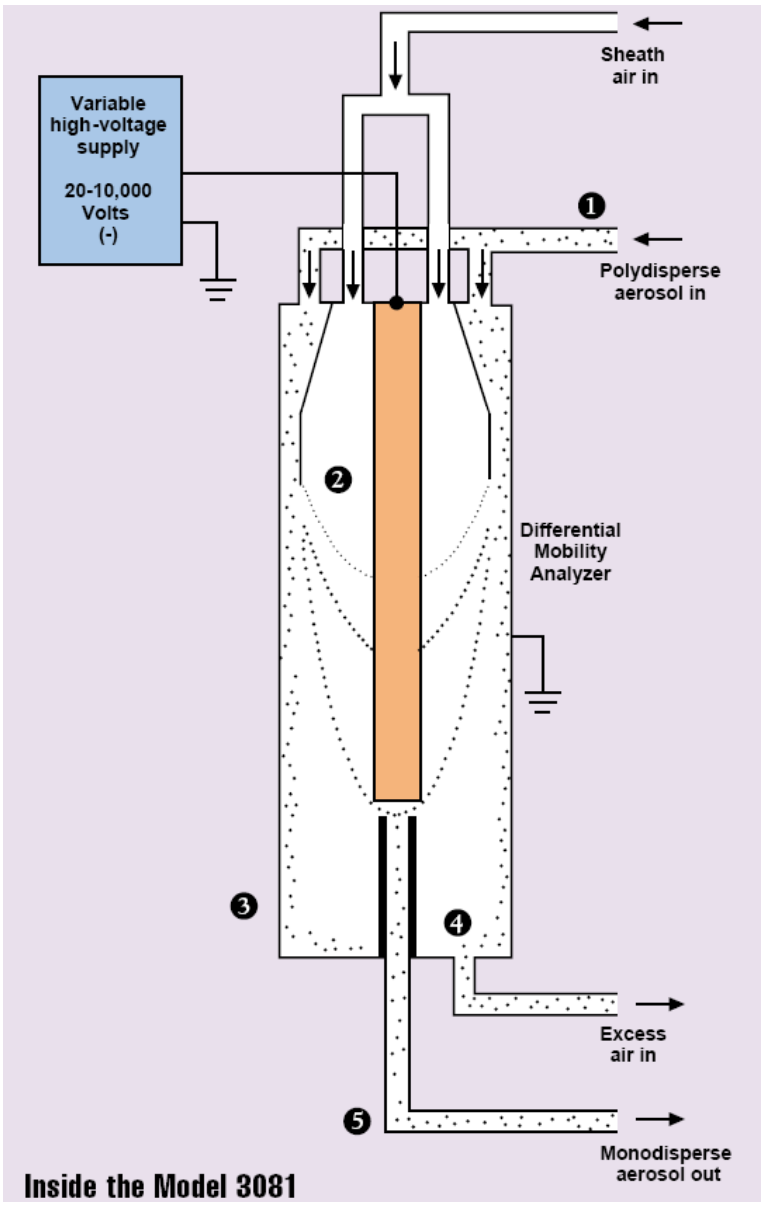

Figure 3.10: Schematic of particle flow inside the DMA column and DMA column working principle. Reprinted with permission from TSI publication 'Series 3080 Electrostatic Classifiers Operation and Service Manual.'

3.4.4 Condensation Particle Counter (CPC)

In the Model 3776 Ultrafine Condensation Particle Counter (UCPC, Figure 3.11), an aerosol sample is drawn continuously through a heated saturator in which, butanol is vaporized and diffuses into the sample stream. Together, the aerosol sample and butanol pass into a cooled condenser where the butanol vapor becomes supersaturated and ready to condense [61]. Particles present in the sample stream serve as condensation nuclei. Once condensation begins, particles that are larger than a threshold diameter quickly grow into larger droplets and pass through an optical detector where they are counted easily.

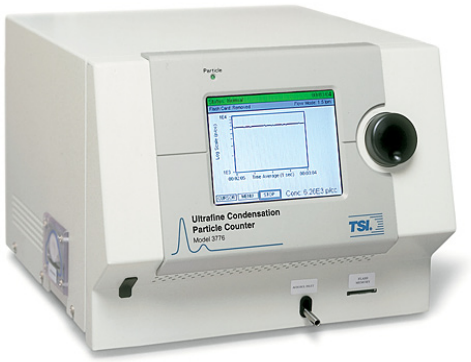

Figure 3.11: Ultrafine Condensation Particle Counter (Model 3776, TSI Inc.) Reprinted with permission from TSI publication ”Model 3776 Ultrafine Condensation Particle Counter Operation and Service manual.”

A schematic of the working mechanism is presented in Figure 3.12. The particle counter detects particles as small as 2.5 nm in diameter, using a unique sheath air flow design that confines the aerosol flow path near the centerline of the condenser. Particles are exposed to the region of highest super-saturation and uniformity of butanol vapor. Even the smallest particles are grown to large droplets for easy optical detection. This unique design greatly enhances measurement response time, produces a sharply defined lower size detection limit (counting efficiency curve) and minimizes diffusion losses of

ultrafine and nanoparticles. The model 3776 UCPC uses a laser-diode light source and diode photodetector to collect scattered light from particles. An internal microprocessor is used for instrument control and data processing (Ref: TSI model 3776 UCPC operation and service manual).

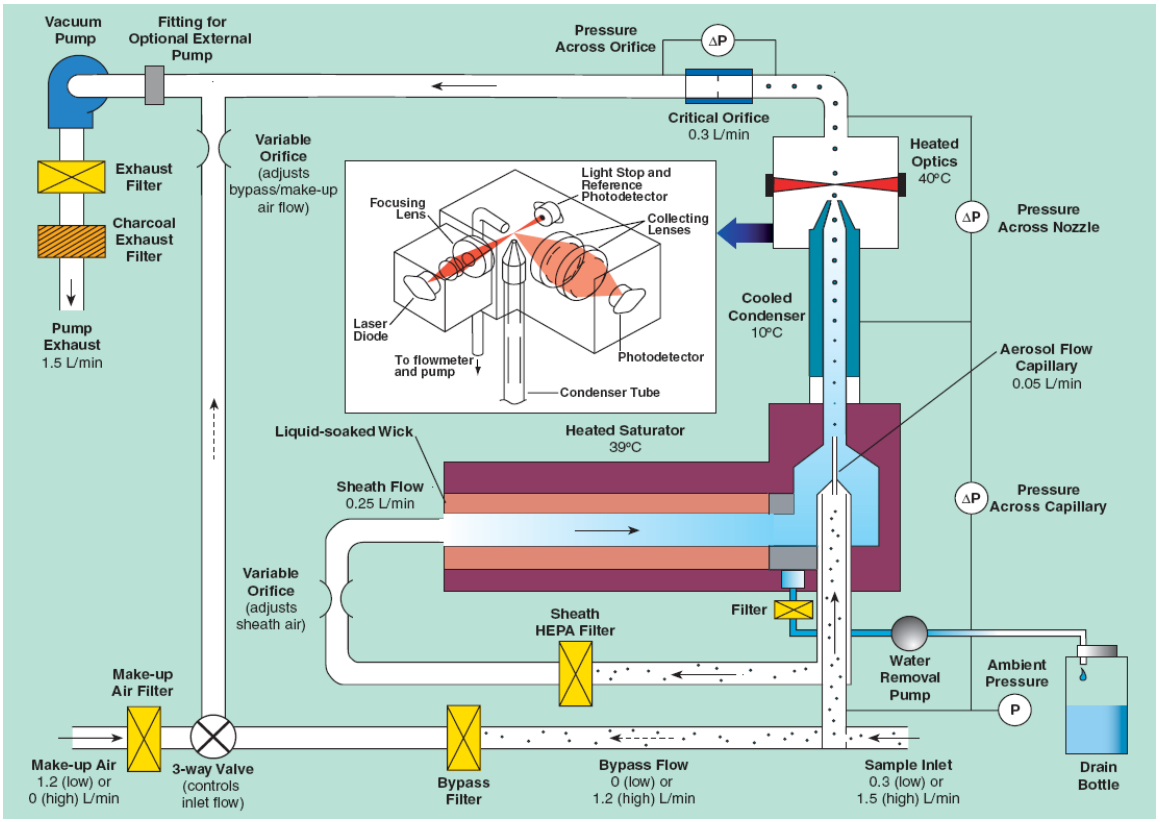

Figure 3.12: Schematic of the working principle of condensation particle counter (Model 3776, TSI Inc.). Reprinted with permission from TSI publication “Model 3776 Ultrafine Condensation Particle Counter Operation and Service manual.”

3.5 Experiment and Results

Argon gas from the GFG-1000 particle generator was heated in a 3/8 inch diameter and 18 inch length pipe that is wrapped with heating tape and insulated around with a heat insulation tape (Figure 3.13).

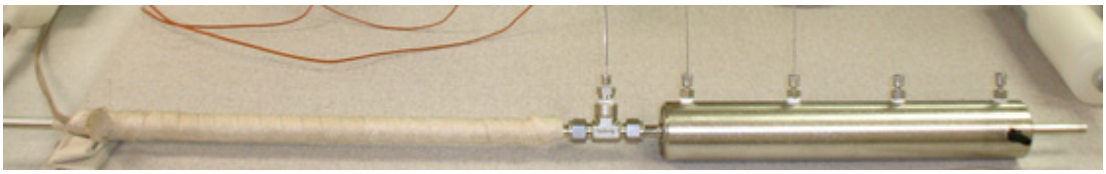

Figure 3.13: Heating tube and thermophoretic deposition tube. Heating tube (18 inch length) is wrapped with heating tape and heat insulation tape around. Active length of thermophoretic deposition tube is 12 inches with 4 thermocouples measuring the tube surface temperature. Another thermocouple inserted into the Swagelok fitting connecting the heating tube and thermophoretic deposition tube measures the inlet gas temperature for thermophoretic deposition tube.

Temperature measurements were made on the surface of the thermophoretic deposition tube, tube inlet and outlet temperatures. The outer surface temperature of the thermophoretic deposition tube was measured using 4 thermocouples (K-type probes) connected to a USB data acquisition system for temperature data. During this measurements, argon gas flow was maintained at 5 l min^{-1} from the GFG-1000 particle generator, flowing through 3/8 inch diameter tube (I.D. = 0.9017 cm) that corresponds to a Re = 899. The cooling water flowing through the annulus around the deposition tube was maintained at temperatures 10 °C and 5 °C at 1 l.min^{-1} flow rate using the Fischer Scientific water chiller bath. The complete experimental setup is shown in Figure 3.14. Alphabetical laebling used for the thermocouples is shown in Figure 3.15.

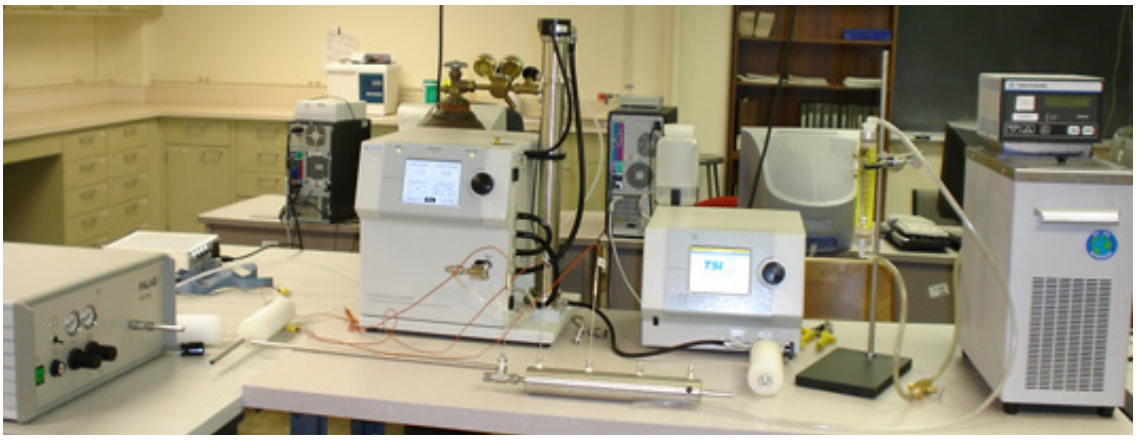

Figure 3.14: Complete experimental setup for thermophoretic deposition of particles that includes a particle generator GFG-1000, electrostatic classifier, ultrafine condensation particle counter, water bath chiller and thermophoretic deposition tube assembly.

Steady temperatures at the inlet, outlet and on the surface of the deposition tube were obtained after about 15 minutes from the start of the experiment. Figure 3.16 shows the temperature measurements for two different surface temperatures on the thermophoretic deposition tube. With the limitations on the fittings that are used in this experiment, the gas can be heated to reach a maximum temperature of 200 °C at the inlet of the deposition tube.

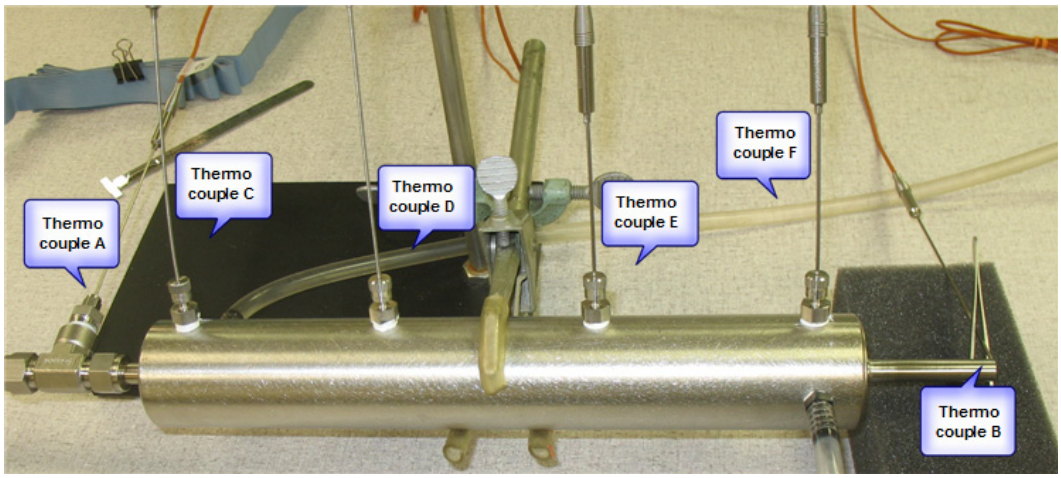

Figure 3.15: Thermocouples arrangement in the experiment and are identified for the inlet flow temperature (thermocouple A), outlet flow temperature (thermocouple B), and deposition tube outer surface temperatures (thermocouples C, D, E, and F)

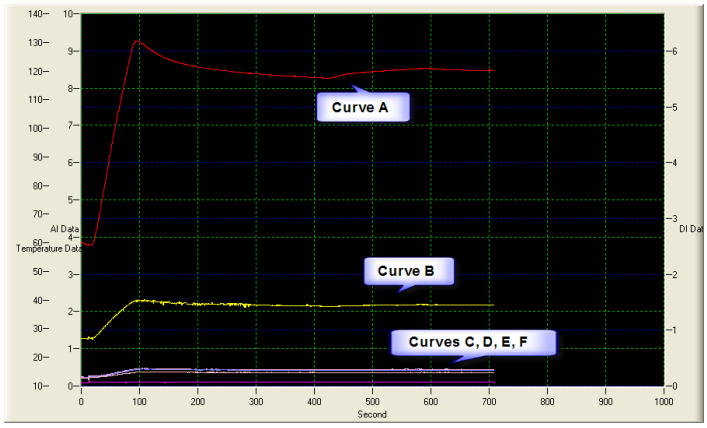

(a)

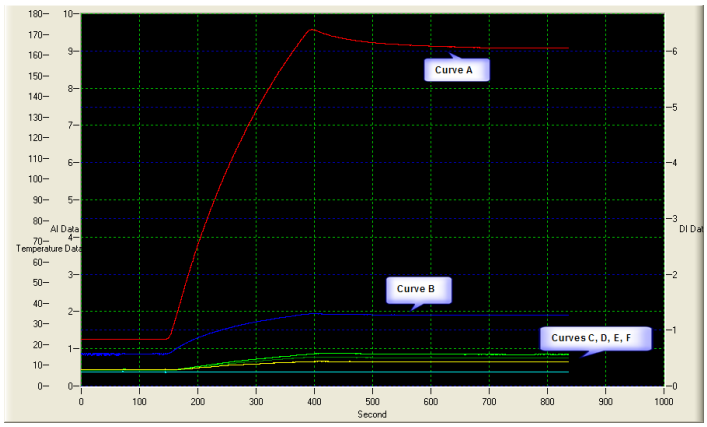

(b)

Figure 3.16: The two sets of measurement of temperatures on the surface of the deposition tube and the inlet and exit temperatures of the gas entering the deposition tube (a) Cooling water at 10 °C and maximum inlet temperature steady at about 120 °C (b) Cooling water at 5 °C and maximum inlet temperature steady at about 160 °C

Carbon nanoparticles generated at a spark frequency of 20 Hz were used in this deposition experiment. The concentration of the particles generated here is very large for the Scanning Mobility Particle Sizer (SMPS) spectrometer and hence need to be diluted. The concentration is diluted by splitting (removing part of the stream) the particle stream and adding particle free clean diluting air. The diluted particle stream was sampled into

the SMPS system and particle size distribution is measured. The diluted stream was then heated to about 120 °C temperature measured at the exit of the heating tube and entering the deposition tube. The heated gas particle stream flows into the thermophoretic deposition section maintained at 5 °C with cold water circulating around the deposition tube. The flow rate of the gas stream from particle generator was maintained at 4 $l.min^{-1}$ all through the experiment.

Particle size distribution of the exiting particle flow from the deposition tube was measured. From measurements of the inlet and outlet particle size distributions, the deposition efficiency can be calculated. Size distribution measurements obtained are shown in Figure 3.17 for the carbon nanoparticle stream entering into and exiting out the thermophoretic deposition tube. From the size distribution measurements, the total thermophoretic deposition efficiency (by number) for particles in the size range 5-50 nm is 77%, for particles in the size range 5-10 nm is 84% and for particles in size range 5-150 nm is 85%. Further, combinations of the particle size peak, inlet particle temperature and thermophoretic deposition tube temperature, would provide better understanding of the deposition behavior.

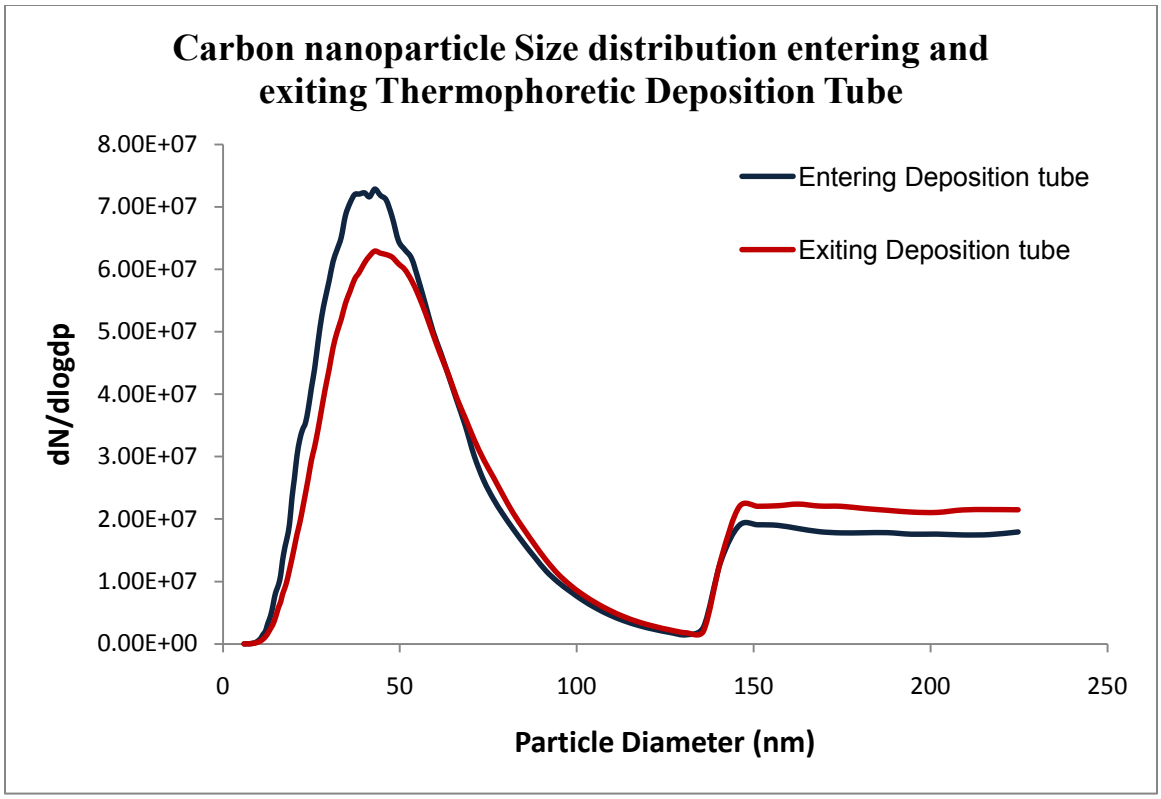

Figure 3.17: Particle size distribution measurements for carbon nanoparticles generated at 20 Hz spark frequency entering into and exiting out the thermophoretic deposition tube. Particle and gas flow rate from the particle generator was maintained at 4 $l.min^{-1}$

CHAPTER 4

PREVIOUS WORK ON PARTICLE DEPOSITION IN LUNG AIRWAYS

4.1 Computations

Aerosol particle deposition in breathing airways was studied experimentally and computationally to a certain extent. The complexity of tracheobronchial tree has defied detailed simulation of the airflow in anything more than small sections. As a result, the majority of work to date on the prediction of particle deposition in the tracheobronchial tree has relied on some form of approximated and idealized airway bifurcation geometry models. Due to limited available computer power, CFD simulations of the structures in the tracheobronchial tree have been limited to the study of simple bifurcations. Kinsara et al. [62] studied computationally the flow profiles and ultrafine particle (Po-218) concentration profiles in 3^{rd} and 4^{th} generation bifurcation CFD model using FIDAP. Several early morphological models were based on symmetric, dichotomously bifurcating systems [14,15]. Mously [22] studied particle deposition in physiologically realistic 3^{rd} and 4^{th} generation bifurcation model using CFD code FLUENT.

Morphometric measurements of the human bronchial airways and models describing their structure have been reported by a number of investigators [14,63-65]. These models lacked information concerning the angles formed by successive branching planes, also known as azimuthal angles. The most complete study of a lung cast, taking into account the asymmetry, published by Horsfield et al. [64], gave only the length,

diameter, and branching angles between the assumed coplanar parent and daughter branches. Some of these models were used to mathematically predict aerosol deposition in the human respiratory tract. Simple geometric configurations, such as single bifurcation or a double bifurcation or triple cascade of bifurcations, led to CFD simulations and gave a first insight into flow profiles and particle deposition in the upper airways. Balashazy et al. [66] have simulated symmetric and asymmetric bifurcations and examined the local deposition patterns under steady inspiratory and steady expiratory flow. Balashazy et al. [67] have also proposed a "deposition enhancement factor" that would indicate the enhanced deposition in the vicinity of a bifurcation over that in the rest of the wall. Balashazy et al. [68] further used his computed deposition enhancement factors to estimate distribution of local deposition and its enhancement factors for lung dosimetry. Hofmann et al. [69] investigated the effect of different modeling approaches on particle deposition, particle clearance, and bronchial cellular doses in a systematic manner for lung dosimetry. Comer et al. [70] and Zhang et al. [71] have calculated this enhancement using CFD models of lung, although their work was limited to generations 3-6 of the Weibel model.

Martonen et al. [72] reviewed particle deposition models presented by various authors for different flow and airway geometry conditions. Human airways have natural structural features like cartilaginous rings and carinal ridges. Such features are clearly present in fiberoptic bronchoscopy examinations [73]. The influences of rings and ridges were examined by Martonen et al. [74-76], where the geometric models used are very unrealistic. It has been pointed out by other researches [77,78] that the precise geometry of the airways has strong influence on the fate of inhaled particles. Nowak et al. [77] have

explored the use of CT based lung airway geometry to simulate aerosol deposition using Discrete Phase Model in FLUENT CFD code. Ertbruggen et al. [79] have proposed a 3D asymmetric computational airway model of the lungs, based on the morphometrical data of Horsfield et al. [64] and studying CT scanner images. They also have studied air flow characteristics and particle deposition efficiencies by performing CFD (FINE/Turbo program) simulations in their developed geometry. Recently, 3-dimensional morphological models of actual lung airways have been developed by reconstructing airway surfaces from high resolution computed tomography images [77,80,81]. However, such CT-based imaging and reconstruction methods are unable to resolve the geometry of very small airways. Cebral et al. [78] investigated the aerodynamics in anatomically realistic lung airways using finite element CFD methods, but was limited to only 3rd generation bifurcations. Most of these published work on particle deposition in lung airways (discussed here), do not consider a real lung airway geometry and in some cases where real airway geometries are considered, only the upper bronchial airway extending up to only few generations were modeled. It is important to consider the geometry with more airway generations to understand the fate of the particles inhaled. Also a comprehensive model including inspiration, expiration, and possible resuspension is required to improve the accuracy of the deposition model.

4.2 Experiments

Smith et al. [82] experimentally determined the particle deposition in tracheobronchial airways using airway casts of young adults and children using molecular clusters of Pb-212 and monodisperse silver particles attached with pb-212 for the deposition study. Zhou et al. [83] experimentally studied the deposition of

monodispersed polystyrene latex fluorescent particles for different inlet flow rates of 15, 30 and 60 l min^{-1}. Experimental measurements of deposition of unattached Po-218 atoms in single bifurcation models [84] have shown that diffusion dominated particle deposition patterns are highly non-uniform, with enhanced deposition along the inside walls of the secondary tubes, while exhibiting local accumulations at the carinal ridge. Su et al. [85] experimentally studied the deposition of MMVF (man-made vitreous fibers) like carbon fibers in two realistic human respiratory tract replicas to investigate the possible factors that could affect the fiber deposition pattern in the human airway.

Carinal regions in the upper bronchial airway bifurcations of the respiratory tract are believed to be the hot spots for nanoparticle deposition. Evidence from animal studies has indicated a higher toxicity from ultrafine particles than from particles of larger size having the same chemical composition [3]. Exposure to radioactive radon progeny in the size range of 1-200 nm causes lung cancer in uranium miners [14] and there have been several studies directed at the elucidation of such deposition [18,19,81]. To estimate the risk from radon exposure, a reliable lung dose model has to be developed, and it is important to know the sites in the lung where particles are deposited.

Lung images obtained by CT-based imaging showed that symmetrical models lack anatomical realism. The anatomy of the tracheobronchial tree is characterized by a three-dimensional asymmetric branching pattern. Therefore, realistic models are preferred over idealized isolated airway bifurcation models. Airflow not only depends strongly on the geometry of the airways but also is intrinsically time-dependent. As a consequence the flow in lung airways is extremely complex. A comprehensive summary of the review of previous computation and experimental work is presented in Table 4.1.

Table 4.1: Review of computational and experimental studies on particle deposition in lung airways and bifurcations

Investigators	**Work summary**	**Comments**
Annapragada, A., Mishchiy, N., (2007) [86]	Use of Large Eddy Simulation method for turbulence modeling, to solve the Navier-Stokes equations for air flow dynamics in lung airways. Used CT scan data for constructing airway geometry.	The airway geometry used for deposition calculations is only up to 4^{th} generation. The particle deposition model is unclear in this work.
Báláshazy I., and Hofmann W., (1993) [87]	Trajectories of aerosol particles (in breathing air) under the simultaneous action of inertial impaction, gravitational settling, Brownian motion and interception were simulated using Monte Carlo techniques.	Finite difference method is used for discretization of the governing equations. Daughters bifurcate at sharp and unrealistic angles. Only inspiratory flow condition.
Báláshazy I., and Hofmann W., (1993) [88]	Local inhomogeneities of aerosol particle deposition under expiratory flow conditions, considering the simultaneous effects of inertial impaction, gravitational settling, Brownian motion and interception. In most cases, deposition hot spots are found downstream of the central bifurcation zone.	Finite difference method is used for discretization of the governing equations. Daughters bifurcate at sharp and unrealistic angles. Only expiratory flow condition.
Báláshazy I., and Hofmann W., (2000) [89]	Quantification of the inhomogeniety of theoretically predicted deposition patterns by local deposition enhancement factors. Local deposition enhancement factors were computed by scanning along the surface of the bifurcation models with prespecified surface area elements.	Deposition patterns of unattached, ultrafine, and attached radon progeny were simulated using FIRE CFD code and particle trajectory model. The 3D model of airway bifurcations is symmetric and non-realistic. Local deposition enhancement factors are important to be considered for dose modeling.
Cebral J.R., and Summers R.M., (2004) [78]	Air flow dynamics in anatomically real lung airways was studied through CFD simulations. Chest CT scan data was used to construct real lung airway geometry model.	This study aims to understand the aerodynamics of ventilation in normal and diseased lung. CFD calculations were performed using FEFLO, an in house flow solver.
Comer J.K., Kleinstreuer C., and Zhang Z., (2001) [90]	Co-planar and non-planar symmetric double bifurcation geometry was used to study the air flow structures and particle deposition patterns for Re=500 and Re=2000, using a commercial CFD code CFX.	Finite volume method based CFD code CFX was used for this simulation study. Anatomically unrealistic symmetric bifurcations were used here.
Ertbruggen C. V., Hirsch C., and Paiva M., (2005) [79]	Developed a 3D asymmetric computational airway model of the lungs, based on the morphometrical data of Horsfield et al. (1971) and studying CT scanner images. Also studied air flow characteristics and particle deposition efficiencies by performing CFD (FINE/Turbo program) simulations.	3D asymmetric model is better than any other constructed model based on morphometric data. Particle tracking was based on Lagrangian model. The size of the particles simulated were atleast 1 μm.

Hofmann W., Bergmann R., and Báláshazy I., (2000) [91]	Investigated the variability in particle deposition in whole lung and individual bronchial airway bifurcations. Uses a stochastic lung and particle deposition model.	Stochastic models do not include the complexity of the lung airway model and complex flow patterns.
Hofmann W., Golser R., and Báláshazy I., (2003) [92]	Computational study. Investigated the inspiratory deposition efficiency of ultrafine particles (1 – 500 nm). Proposed a Linear-quadratic function in diffusion coefficient D and flow rate Q for deposition efficiency.	3^{rd} and 4^{th} generation bifurcation model was used. Inspiratory flow rates used were 1.25, 7.5 and 15 l min^{-1}. Linear-quadratic function in diffusion coefficient D and flow rate Q for deposition efficiency based on the numerical results was not convincing after looking at the comparison with other published data.
Horsfield K., Dart G., Olson D.E., Filley G.F., and Cumming G., (1971) [64]	Morphometric model of human lung airway was developed using lung casts with detail of branch lengths, diameters, and branching angles until 16 generations of bifurcating airways.	The most complete morphometric model of human lung airway, taking into account the asymmetry of the bifurcations. The author gave only the length, diameter, and branching angles between the assumed coplanar parent and daughter branches.
Kim C.S., Fisher D.M., Lutz D.J., and Gerrity T.R., (1994) [93]	Experimentally studied the local deposition efficiencies and deposition patterns in single bifurcation tube models with varying geometry (branching angle, daughter to parent tube diameter ratio, and local obstruction). Also proposed a formula for particle deposition efficiency from his data.	The proposed formula for particle deposition efficiency was obtained a curve fitted to the data as a function of stokes number.
Kinsara A.A., Loyalka S.K., Tompson R.V., Miller W.H., and Holub R.F., (1995) [84]	Experimentally measured the local deposition of radon progeny (Po-218) in the molecular size range sampled through an aluminum model for 3^{rd} and 4^{th} generation bifurcation.	Reported the local deposition velocities along the length of the daughter tubes. Deposition was measured along the inside, outside, top, and bottom walls of secondary (daughter) tubes.
Kinsara, A.A.; Tompson, R. V.; Loyalka, S. K., (1993) [62]	Studied computationally the flow profiles and ultrafine particle (Po-218) concentration profiles in 3^{rd} and 4^{th} generation bifurcation CFD model using FIDAP	The bifurcation geometry was Weibel A model, symmetric and idealistic in dimensions.
Martonen T., Isaacs K., and Hwang D., (2005) [73]	Developed *in silico* computational models of particle dosimetry which is more focused on a computer code that yields 3D visualization of human lungs.	Also described the topics in brief to be considered while modeling particle deposition in lung airways. The model developed here still is unrealistic with straight tubes and sharp bifurcation angles.
Martonen T.B., Musante C.J., Segal R.A., Schroeter J.D., Hwang D., Dolovich M.A., Burton R., Spencer R.M., and Fleming J.S., (2000) [72]	Reviewed lung airway models and particle deposition within presented by various authors for different flow and airway geometry conditions.	Review includes strengths and limitations of models with matter of concept and involved technicalities.

Nowak N., Kakade P.P., and Annapragada A.V., (2003) [77]	Computationally studied the flow patterns and deposition of particles in an anatomically realistic bifurcation model. Bifurcation model was developed using CT scan based image data.	Used CFD code FLUENT for computations. Most part of the published work concentrates on Weibel (1963) model (symmetric airway model). In this case CT based airway model was limited to four generations.
Smith S., Cheng Y.S., and Yeh H. C., (2001) [82]	Experimentally determined the ultrafine particle deposition in tracheobronchial airways using airway casts of young adults and children.	Used molecular clusters of Pb-212 and monodisperse silver particles attached with pb-212 for the deposition study, and compared the deposition data with theoretical predictions based on the diffusional deposition in circular tubes assuming fully developed parabolic or plug flow.
Su W.C., and Cheng Y.S., (2006) [85]	Experimentally studied the deposition of MMVF (man-made vitreous fibers) like carbon fibers in two realistic human respiratory tract replicas to investigate the possible factors that could affect the fiber deposition pattern in the human airway.	Three inspiratory flow rates of 15 L/min, 43.5 L/min and 60 L/min were used. The results showed that fiber length (mass) and inspiratory flow rate (fiber velocity) are two factors that can change the fiber deposition pattern considerably.
Yamada Y., Koizumi A., and Inaba J., (1998) [74]	Investigated new methods to cast lung airways for experimental studies. CAD data was used to construct casts by stereo-lithography method using curable resin. Experimentally measured deposition in the lung cast models prepared.	Innovative method to build lung airway casts from CAD data. Polydisperse NaCl aerosols were used for the experiment to measure deposition efficiency.
Zhang Y. and Finlay W.H., (2005) [95]	Experimentally measured effect of cartilaginous rings on particle deposition. Particles ranging between 2.9-6.3 µm for inhalation flow rates of 30 l min^{-1} and 60 l min^{-1}.	Lung airway models are produced using stereo-lithography (3D printing). Particle deposition measurements were based on gravimetric technique.
Zhang Z., Kleinstreuer C., and Kim C.S., (2002) [96]	Studied unsteady (time-dependent) micron size particle transport and deposition in a symmetric idealized triple bifurcation model for laminar inhalation flow condition. Computational simulation using CFX (CFD code).	Use of time dependent inspiratory flow condition was better than steady inlet flow condition. The geometry model used is symmetric and idealized.
Zhang Z., Kleinstreuer C., Kim C.S., and Cheng Y.S., (2004) [97]	Computationally investigated the effect of curved inlet tubes on air flow and particle deposition patterns in triple bifurcating lung model. Used a 90° and 30° bent inlet tubes.	Used a parabolic uniform inlet velocity profile. CFX (CFD code) was used.
Zhou Y., and Cheng Y.S., (2005) [83]	Experimentally studied the deposition of monodispersed, polystyrene latex fluorescent particles in human airway replica with different flow rates of 15, 30 and 60 l min^{-1}.	Human airway replica was made from an adult cadaver including the oral cavity, pharynx, larynx, trachea and four generations of bronchi.

CHAPTER V

PARTICLE DEPOSITION IN LUNG AIRWAY BIFURCATIONS: SIMPLE GEOMETRIES

Aerosols get transported into the lung airways when we inhale during breathing, and many would deposit on the airway surfaces. Particle deposition models were developed using CFD code FLUENT (Ansys Inc.) for the local deposition patterns and overall deposition efficiencies for certain aerosols of interest in human lung airways. Deposition in symmetric bifurcation geometry was first studied and then explored realistic bifurcation and real airway geometries. It was noted that, realistic geometry consideration is the only way to obtain accurate estimates on the particle deposition efficiencies in human lung airways. Models developed here assume rigid airway walls and this approximation, which is common to most experimental and numerical models, is acceptable in normal quiet breathing condition during which, variations of the length and diameter of the airways remain moderate. In rapid and deep breathing, the flow may change significantly and this assumption may not be appropriate.

To verify the computational model used in this study, particle deposition patterns and efficiencies in the 3^{rd} and 4^{th} generations of lung airway bifurcations were first studied. The 3^{rd} and 4^{th} generations of airway bifurcations are chosen as there are published experimental and computational results for particle deposition efficiency in simplified geometry models. Symmetric and realistic geometries will be constructed and used in these computational models. The results obtained from our computational model

were compared against published experimental data (Kinsara et al., 1995) for symmetric geometry lung bifurcations.

5.1 Computational Fluid Dynamics Model

CFD code FLUENT was used to model particle deposition and compute deposition efficiencies in human lung airways. Models developed here assume rigid airway walls. This approximation, which is common to most experimental and numerical models, is acceptable in normal quiet breathing since variations of the length and diameter of the airways remain moderate. In rapid and deep breathing, the flow may change significantly and this assumption may not be appropriate.

5.1.1 Modeling Polonium-218 deposition for inspiratory flow condition: species transport model

Deposition of radon (Rn-222) progeny i.e. decay product Po-218 in lung airways is modeled. Po-218 was considered in the decay chain of Rn-222, as it has a small decay half-life of 3.1 min and contributes to a large amount of the radiation dose from radon dose. To model Po-218 in the gas phase, Po-218 molecules were considered as gaseous species in the CFD model and used species transport & reaction model in the CFD code FLUENT. A constant air flow rate at steady state is considered in this model to simulate inspiratory phase of breathing. Air flow rate at the inlet depends on the breathing parameters tidal volume (air inspired during a normal breath), and breathing frequency (number of breaths per minute), that vary with physical activity performed by the individual. The airflow rate into the trachea spans from 100 $cm^3.s^{-1}$ at rest to 2000 $cm^3.s^{-1}$ for heavy exercise conditions (NCRP report 125). Light activity breathing

conditions were considered with 1 $m.s^{-1}$ air velocity at the inlet of 3rd airway bifurcation (Kinsara et al., 1995) corresponding to a Reynolds number Re = 370. Hence, the air flow at the parent inlet is assumed to be fully developed laminar.

For the gas flow fields through the bifurcation, the governing equations are the continuity equation

$$\frac{\partial \rho}{\partial t} + \nabla \bullet (\rho \mathbf{u}) = 0$$

and the momentum equation

$$\rho \frac{\partial \mathbf{u}}{\partial t} + \rho \mathbf{u} \bullet \nabla \mathbf{u} = -\nabla p + \mu \nabla^2 \mathbf{u}$$

where, ρ is the mass density, t is the time, p is the static pressure **u** is velocity vector and μ is the dynamic viscosity. The above equations are solved at steady state conditions for fluid flow profiles in the bifurcation geometry.

N_2 is the bulk gas in the flow fields with Po-218 particles being represented as a gaseous trace species. The polonium particles defined here are molecular phase Po-218 (Kinsara et al., 1995), decay product of radon gas. Mass fraction of Po-218 species is 1×10^{-8} in accordance with the typical range of radon concentrations in the air. Particle deposition was defined as a reaction between polonium gas species and sites to form Po-218 solid species. The density of deposition sites is 1×10^{-6} $kmol.m^{-2}$ (0.218 $g.m^{-2}$) on the wall surface, that corresponds to a monolayer of defined deposition site species. The Po-218 solid species deposits permanently on the wall surface following the reaction. The reaction is

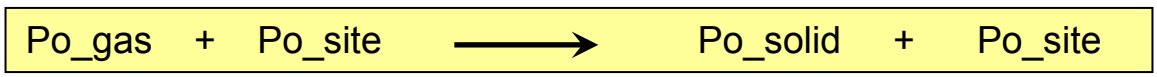

Species concentration and the total flux are determined from the following equations

$$\rho\left(\frac{\partial C}{\partial t}+\mathbf{u}.\nabla C\right)=\rho\nabla\bullet\left(D\nabla C\right)$$

and

$$\frac{\partial\rho}{\partial t}\left(\rho C\right)+\nabla\bullet\left(\rho\mathbf{u}C\right)=-\nabla\bullet J$$

where C is the mass fraction of the species, D is the particle diffusion coefficient and J is the diffusion flux of the species. For transport of polonium species (particles defined as species in the model), the species conservation equation for species mass fraction at steady state are solved.

5.2 Results

5.2.1 Symmetric airway geometry for 3rd and 4th generation bifurcation

Weibel (1963) lung model's 3rd and 4th generation bifurcation was considered, which is symmetric in nature and is the simplest geometry. According to Weibel (1963), each parent tube in the human tracheobronchial tree branches dichotomously into two equal tubes with smaller diameters. The geometry shown in Figure 5.1 represents typical dimensions (see Table 5.1) and shape of bronchial bifurcations similar to Weibel's model of the 3rd and 4th airway generations. The 3rd and 4th generations of airway bifurcations are chosen as there are published experimental and computational results for particle deposition efficiency. The geometry in this case is symmetric with daughter bifurcations branching out at 45 degree angles from the axis of 3rd generation airway. This geometry was constructed in GAMBIT (a preprocessor to FLUENT CFD) and the geometry was

discretized into small compute volumes by the meshing process shown in Figure 5.1. The meshed geometry was exported for further computation. The results obtained from our computational model were compared against published experimental data (Kinsara et al., 1995) for symmetric lung bifurcation geometry model.

Downstream from the parent tube, the velocity profiles in the plane of the bifurcation become heavily skewed. The surface deposition patterns of Po-218 on the wall surface are shown in Figure 5.2. The increased deposition in the vicinity of the carina is due to the large velocity and concentration gradients near the carina.

Particle deposition velocities are calculated from the wall surface deposition rates for Po-218. A plot of Po-218 particle deposition velocities along the line of intersection of the inner wall of the daughter tube with the plane of the bifurcation is shown in Figure 5.3. The deposition velocities obtained here are in close agreement with the experimental data (Kinsara et al, 1995) shown in Table 5.2.

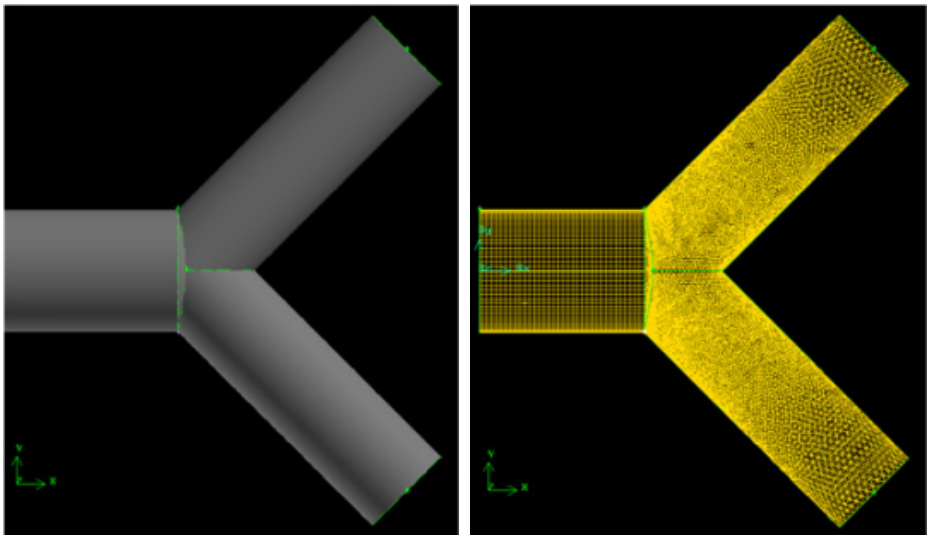

Figure 5.1: Symmetric idealized 3rd and 4th airway generations geometry and mesh generated for the geometry

Table 5.1: Symmetric 3rd and 4th bifurcation model dimensions

	Length	**Diameter**	**Branching angle**
Parent	0.76 cm	0.56 cm	N/A
Daughter A	1.27 cm	0.45 cm	45°
Daughter B	1.27 cm	0.45 cm	45°

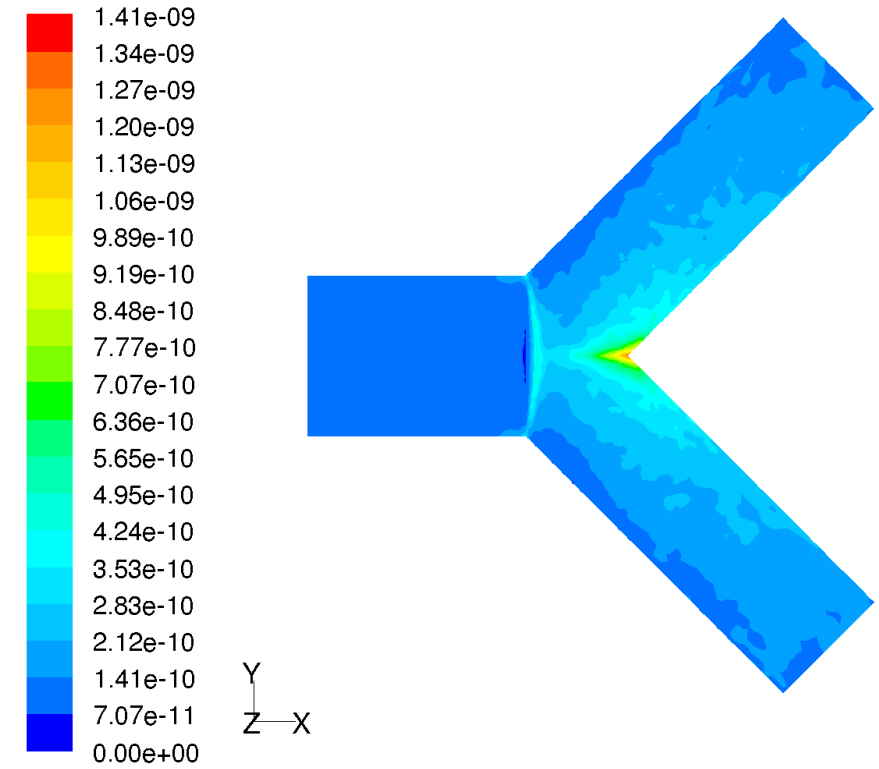

Figure 5.2: Contour plot of surface deposition rate of Po-218 for symmetric airway bifurcation geometry

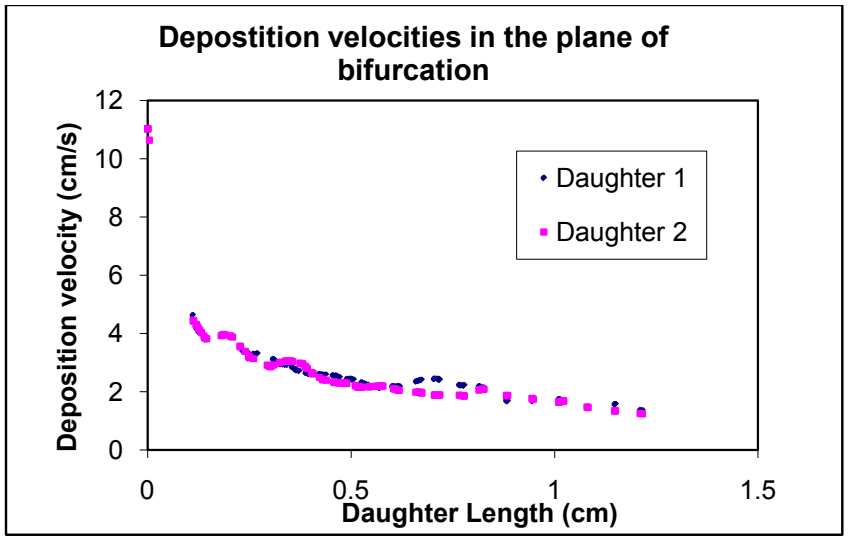

Figure 5.3: The deposition velocities are calculated from the deposition rates obtained from the FLUENT computations and are plotted along the length of the daughter tube.

Table 5.2: Comparison of deposition velocities from FLUENT computations with published experimental data

Daughter 1 length (cm)	Deposition Velocity (cm/s)	
	Experimental data (Kinsara et al.)	FLUENT computation
0.15	4.5	3.8
0.45	2.8	2.57
0.72	1.7	2.41
1.0	1.75	1.75
1.3	1.5	1.37

5.2.2 Realistic airway bifurcation model for the 3rd and 4th generation bifurcation

A more realistic bifurcation geometry was constructed using more realistic dimensions for 3rd and 4th generations bifurcation and are presented in the Table 5.3. These dimensions are obtained from Horsfield et al. (1971). The constructed geometry from these dimensions is shown in the Figure 5.4. The same deposition model in CFD code FLUENT was used to study the deposition patterns and surface contours of Po-218

particle deposition rate are shown in Figure 5.5. Particle deposition velocities are calculated from the wall surface deposition rates for Po-218. A plot of Po-218 particle deposition velocities along the line of intersection of the inner wall of the daughter tube with the plane of the bifurcation is shown in Figure 5.6.

Table 5.3: Asymmetric 3rd and 4th bifurcation (realistic) model dimensions

	Length	**Diameter**	**Branching angle**
Parent	0.76 cm	0.56 cm	N/A
Daughter A	1.27 cm	0.45 cm	35°
Daughter B	0.76 cm	0.36 cm	55°

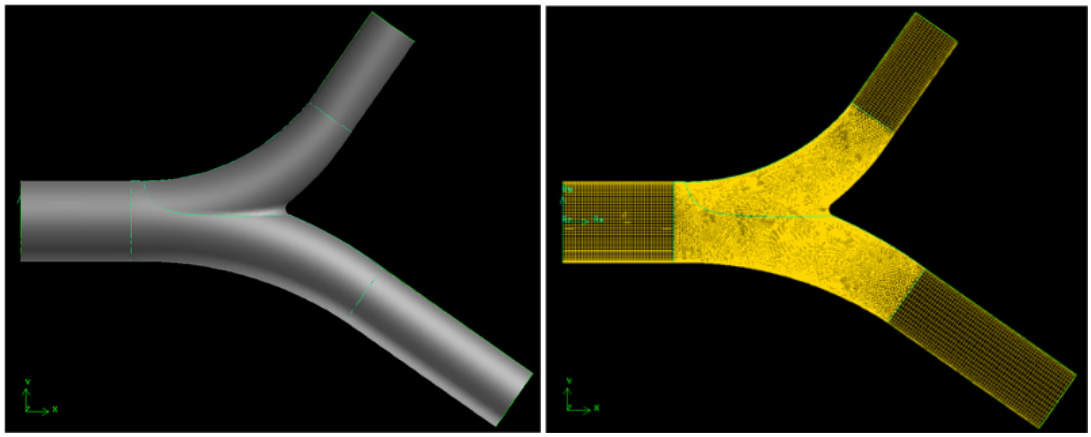

(a) (b)

Figure 5.4: Realistic 3rd and 4th generation airway bifurcation (a) geometry and (b) mesh generated for the volume

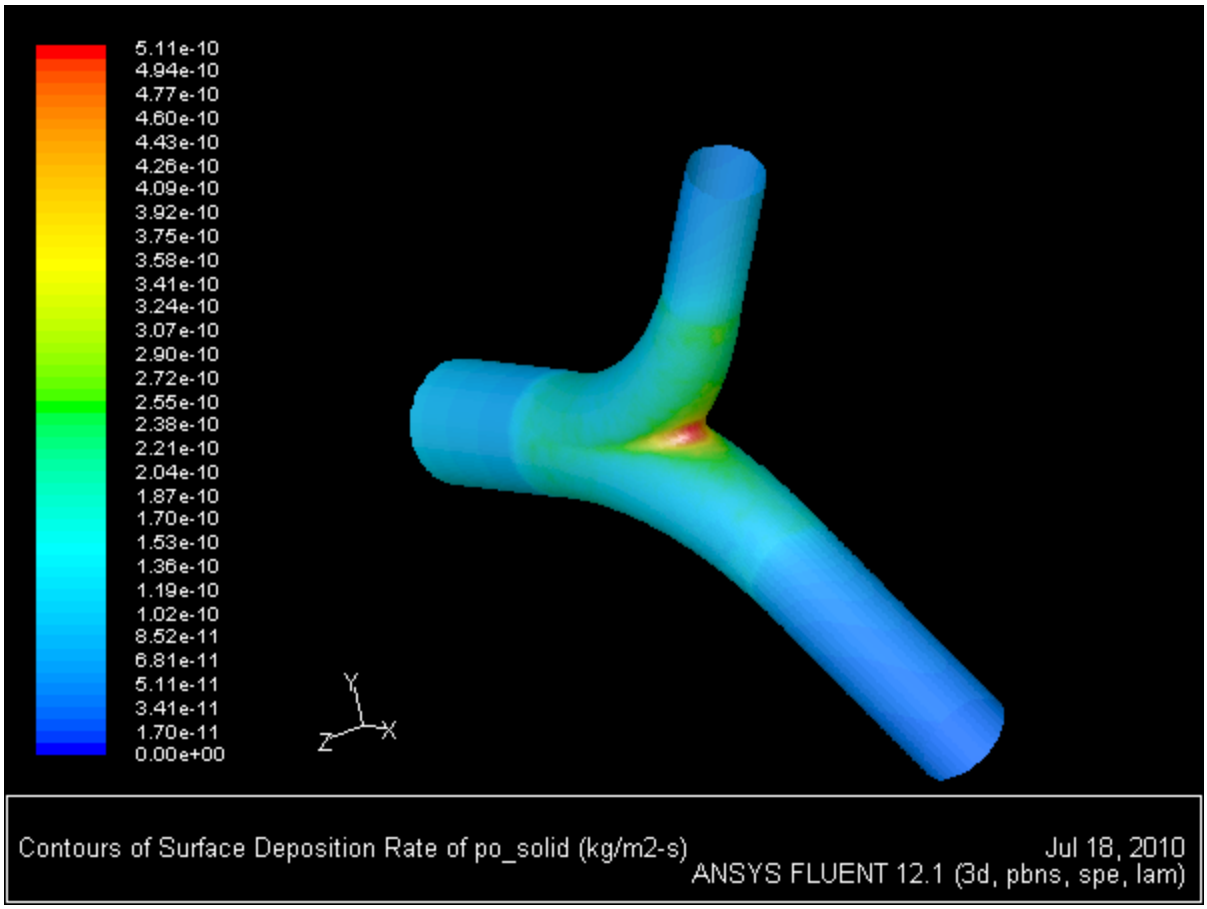

Figure 5.5: Surface contours of deposition rate of Po-218 particles in the realistic 3rd and 4th generation airway bifurcation

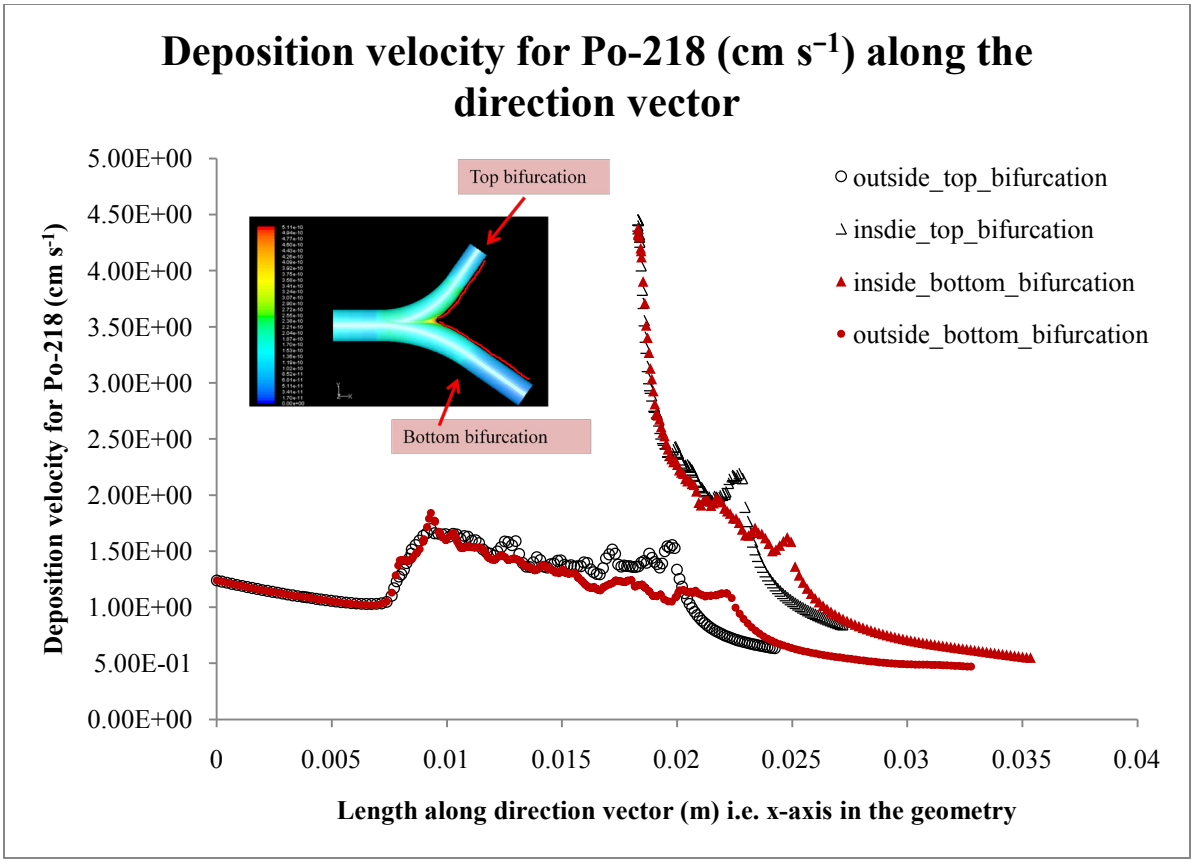

Figure 5.6: Deposition velocities plotted along the direction vector of the parent tube as shown in the inset of the graph here.

CHAPTER VI

PARTICLE DEPOSITION IN REAL AIRWAY GEOMETRY

Anatomically based airway geometry models can be obtained from CT based image data and MRI based image data. Chest CT scan image data was used which was obtained from University Hospitals at University of Missouri, of patients without patient identification information (deidentified) in accord to the Health Insurance Portability and Accountability Act (HIPAA). CT image data works better than MRI data because one can get better resolution and good contrast between air and tissue. From the chest CT image data, the real lung airway surface geometry was extracted using the CT image data analysis and volume rendering software's Amira (Visage Imaging) and Mimics (Materialise). Particle transport and deposition models described in previous chapter were used to study the deposition patterns in real airways using FLUENT CFD code.

6.1 Real lung airway geometry extraction

Lung airway geometry was extracted using commercially available software programs. Two software programs Amira (Visage Imaging®) and Mimics (Materialise) were used in this work. To extract the desired surface geometry from CT image data, one needs to contour or mark the regions of interest on every CT image (2D image) known as segmentation process to obtain a 3D volume or surface of interest. The extracted surface from image segmentation was analyzed for surface abnormalities and errors during image

segmentation, and processed further for use in CFD code FLUENT to study particle deposition patterns and efficiencies. Mimics program has very easy to use and helpful tools compared to Amira to analyze and process the airway surface obtained from image segmentation.

6.1.1 Image Segmentation and Surface Extraction

The chest CT scan image data obtained from University Hospitals at University of Missouri are in dicom (Digital Imaging and Communications in Medicine) format. The dicom image data set consists of two dimensional images of the chest slices and the data is opened in Amira program. The resolution on the image data is 0.6 mm i.e. each CT image or slice is 0.6 mm distance apart. Figure 6.1 displays the CT data read into Amira program as 2D images in XY, YZ and ZX planes.

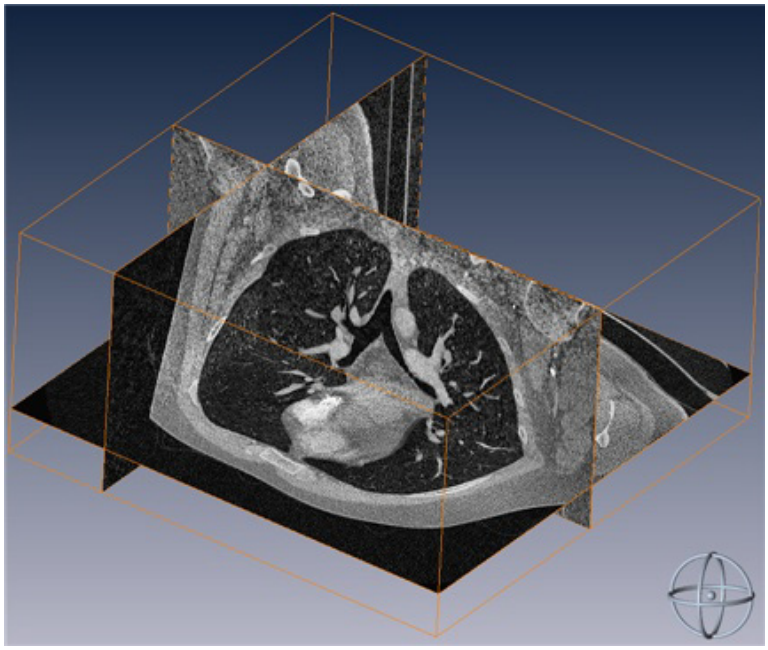

Figure 6.1: Chest CT scan data images displayed in XY, YZ and ZX planes

Using the image segmentation feature in Amira, contouring is done by selecting lung airway regions on each of the 2D image slice in XY, YZ and XZ views of the data at the same time and save the selection. Our selection can be viewed in 3D in another window as illustrated in Figure 6.2. Segmentation process is easier by applying a threshold on the image intensity which is measured in Hounsfield Units. The Hounsfield unit (HU) scale is a linear transformation of the original linear attenuation coefficient measurement in which the radiodensity of distilled water at standard pressure and temperature (STP) is defined as zero Hounsfield units (HU), while the radiodensity of air at STP is defined as −1000 HU. In Figure 6.2, most of the region is black which corresponds to very low HU number close to −1000 HU. This is because, most of lung is filled with air and the region in light gray or white color is mostly lung tissue. For this reason, the selection of the lung airway surface becomes very tedious, which needs careful analysis of each 2D image in all planes. CT scan image quality and scan resolution limits the depth of the airway generations that can contoured and selected for generating the airway surface. A three dimensional airway surface is generated from the selected and saved airway region from the image segmentation process as shown in Figure 6.3. This 3D surface is exported in dicom file format for further analysis and processing in Mimics program.

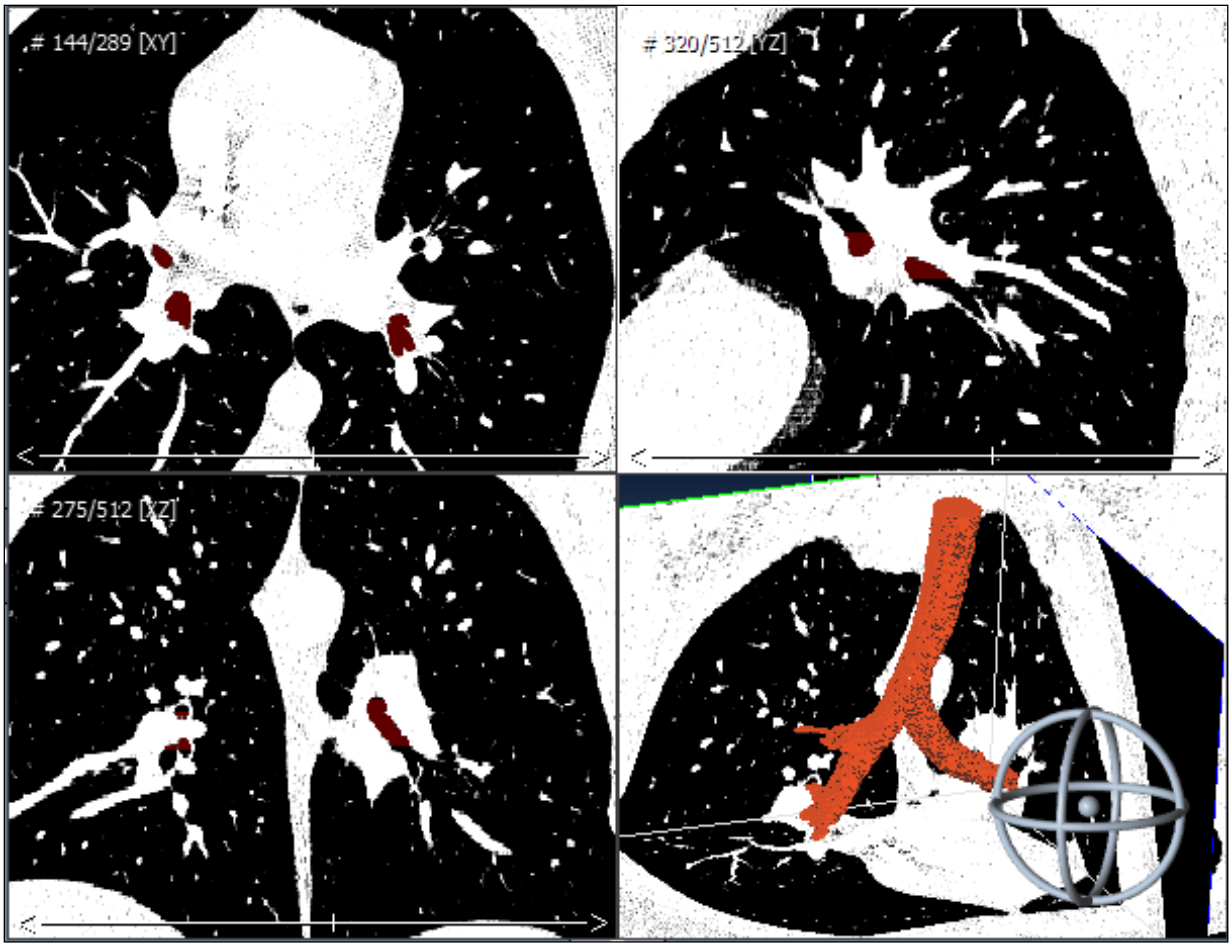

Figure 6.2: Image segmentation of chest CT data in Amira program in XY, YZ, and XZ planes along with 3D viewing of the selected airway region

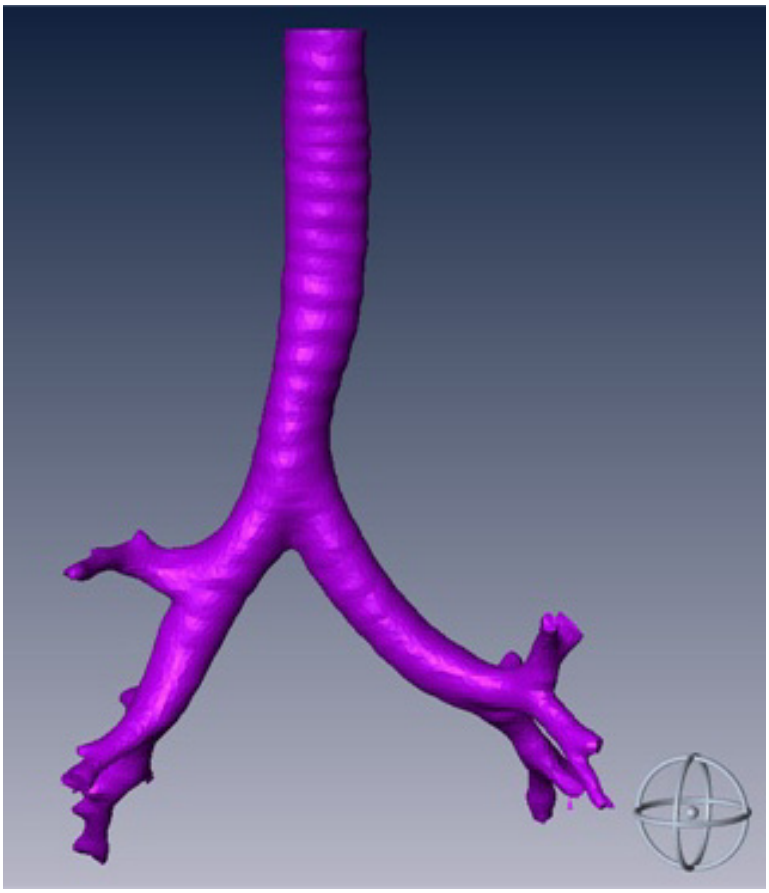

Figure 6.3: Surface of airway geometry extracted from image segmentation of the chest CT scan image data in the CT data analysis program AMIRA (Visage Imaging®).

6.1.2 Lung Airway Surface Analysis and Processing

The new dicom image data is opened in Mimics program and the airway surface is displayed as shown in Figure 6.4. It is clearly observed that the surface has roughness, protrusions and small dents on the surface which were caused during the image segmentation process. This extent of the surface roughness and imperfections obtained during image segmentation process is based on the image quality and resolution where one is actually selecting voxels (similar to pixels) on each dicom image (512 voxels x 512 voxels). High resolution CT data will provide more number of image slices per unit length that helps to reduce these imperfections from image segmentation to some extent.

Mimics software has built in tools (surface smoothing algorithms) that will smooth out the surface without compromising the anatomical details on the surface. Before the surface is smoothened, some airway extremities had to be eliminated as the anatomical detail is unclear or lost at these extremities in the geometry shown in Figure 6.4. Using a split/cut tool in the program the undesired parts of the geometry were removed. Similarly, plane surfaces that represent air flow outlets for each of the end bifurcations were created.

The airway geometry after removing the undesired portions of the surface geometry is shown in Figure 6.5(a). This surface was then smoothed to remove surface imperfections caused during image segmentation. The smoothed airway surface is shown in Figure 6.5(b). The airway surface is then meshed to represent the surface in mathematical form for finite element or finite volume computing.

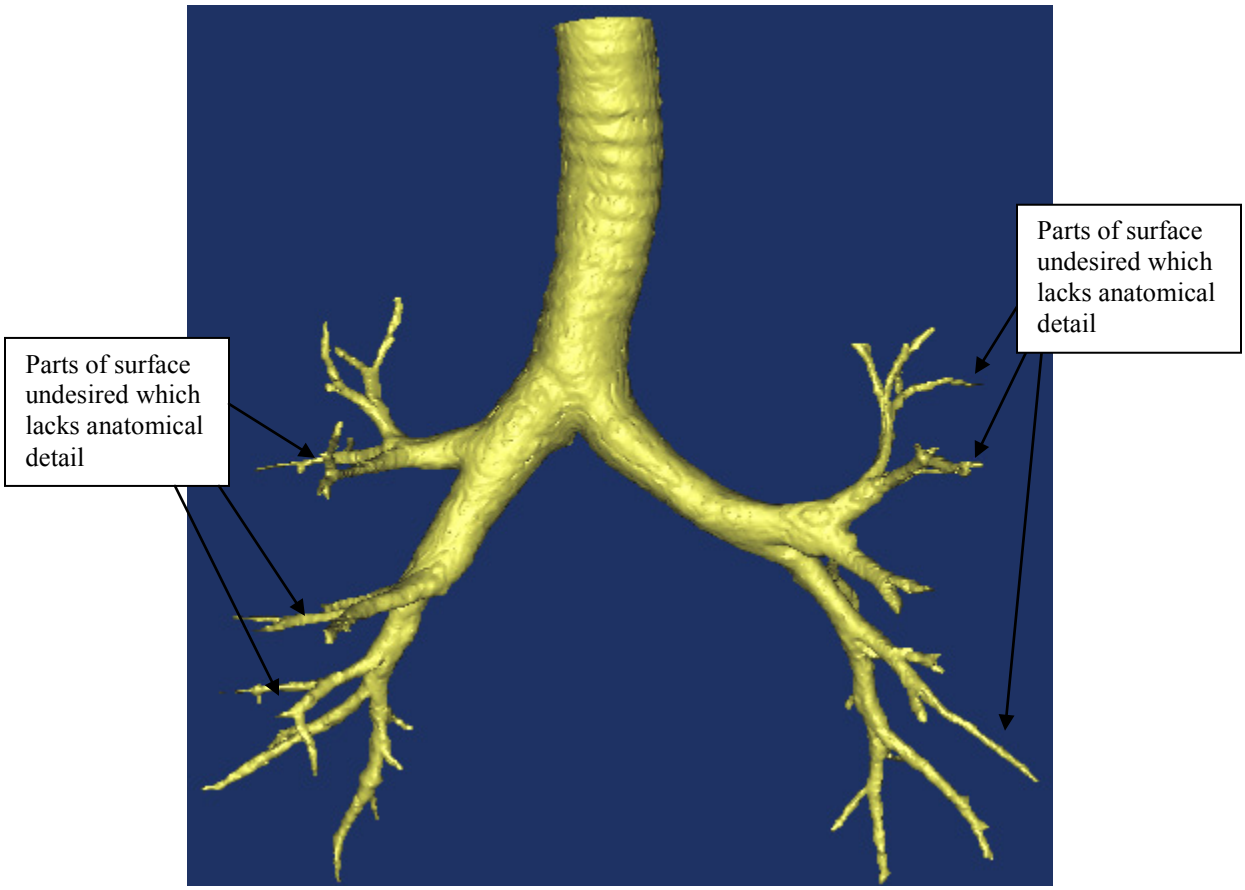

Figure 6.4: Airway surface displayed in mimics (Materialise) program that was generated from image segmentation in Amira (Visage Imaging®) program

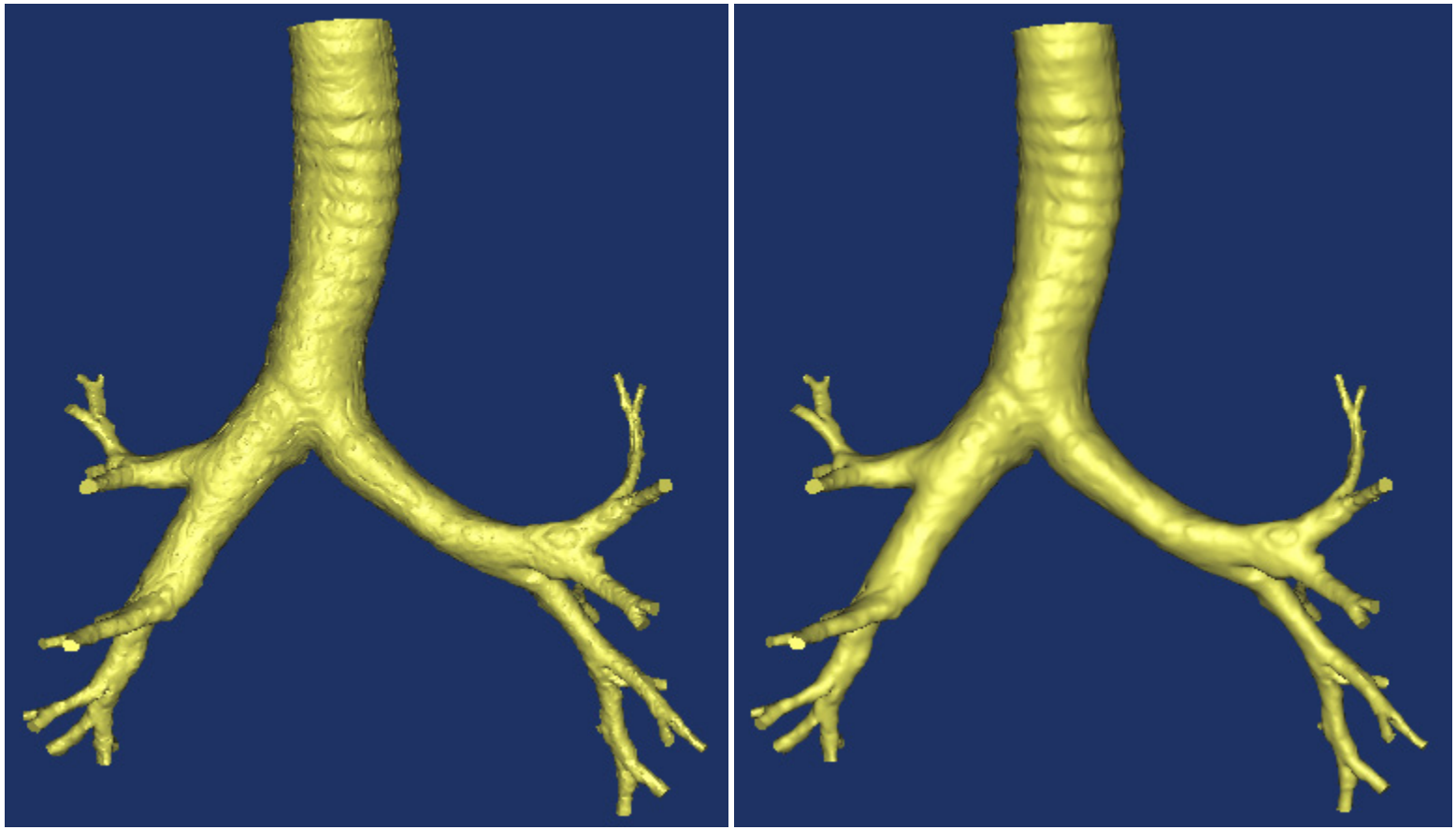

(a) (b)

Figure 6.5: (a) Lung airway surface obtained in Mimics program after removing the undesired sections of the airway geometry that is lacking anatomical detail. (b) Lung airway surface obtained after smoothing the surface shown in (a)

Meshing creates nodes (points with co-ordinate information) on the geometry surface and represents the surface with triangles formed by the nodes on the surface. More the nodes on the surface, the better is the quality of the surface which matches closely to the original surface before meshing. The quality of the surface is measured on a scale of 0 to 1, and a quality factor of 0.97 or above is considered best. A surface mesh with a quality factor of 0.98 was generated and exported as a mesh file (.msh file format). This mesh file can be readily used in GAMBIT (pre-processor for CFD code FLUENT) program to create a flow volume, generate volume mesh and define surfaces and boundaries for particle deposition computations using FLUENT.

6.2 Volume Mesh Generation

The 3D surface mesh was read into GAMBIT and was analyzed for open edges and overlapping edges and faces. The identified defects on the surface are cleaned up using the tools available in GAMBIT program. A clean surface was obtained with well defined inlet and outlets for air flow as shown in Figure 6.6. To generate a good quality surface mesh, tools in GAMBIT were used, where the user can control the mesh generated for the airway volume and on all edges and surfaces. The number of nodes on each edge of the faces defining inlet and outlets for the airway geometry were custom defined. The face mesh is first generated on all the outlet faces and the inlet face using the boundary mesh defined near the wall boundaries of the faces. Since the surface is complicated with many bifurcations that are small in diameter compared to the trachea, the volume mesh generation created errors like lack of sufficient computer memory. This might have happened because of the controlled meshing parameters on a very complex surface geometry. The boundary layer mesh was removed and the surface was meshed

again to successfully obtain a meshed surface and further a meshed (or discretized) volume for CFD computations in GAMBIT after surface topology analysis and cleanup. The meshed surface is shown in Figure 6.7. The mesh detail on the airway branches is shown in Figures 6.8 – 6.11.

To including the boundary layer meshing which gives more controlled surface mesh and thus volume mesh, the airway geometry was simplified by removing some of the airway bifurcations. This also allowed the computations to speed up as the mesh is more controlled and the skewness in the mesh was reduced. The simplified airway geometry prepared in Mimics programs by cutting some more end bifurcations on the geometry in Figure 6.5 (b) is shown in Figure 6.12. This geometry was exported as a triangular surface mesh file to be processed in GAMBIT.

Using GAMBIT, the simplified airway surface was cleaned up for surface topological defects and shown in Figure 6.13(a). The inlet and outlet faces were meshed using boundary layer meshing on the faces. The airway volume was meshed or discretized into small computational volumes/cells. This meshed or discretized computational domain shown in Figure 6.13(b) of the real airway geometry developed using chest CT scan data was exported as a mesh file with defined inlet, outlets, flow domains and wall surfaces for CFD modeling.

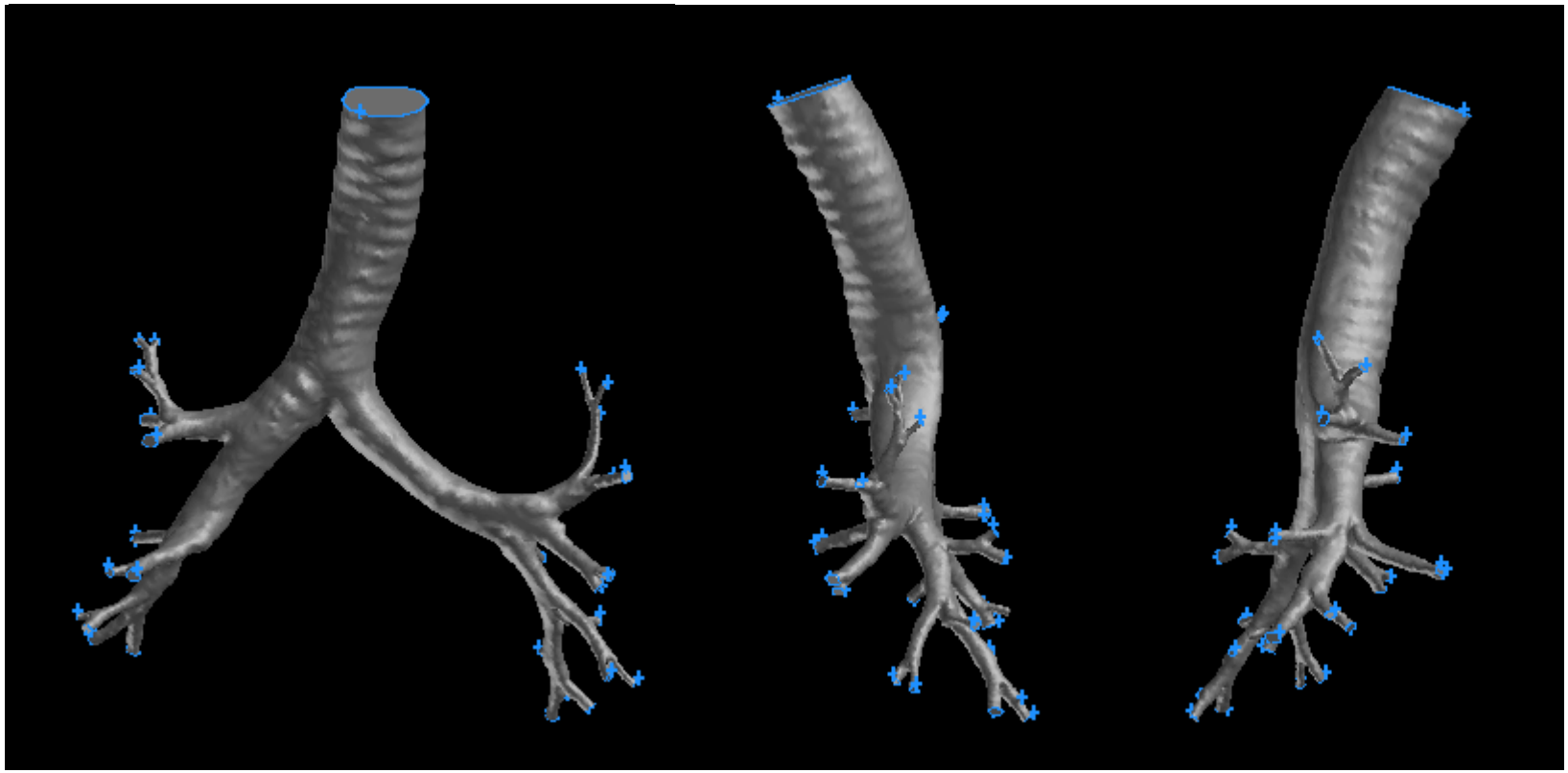

(a) front view (b) right view (c) left view

Figure 6.6: Rendered surface geometry of human lung airway from CT scan image data imported into GAMBIT

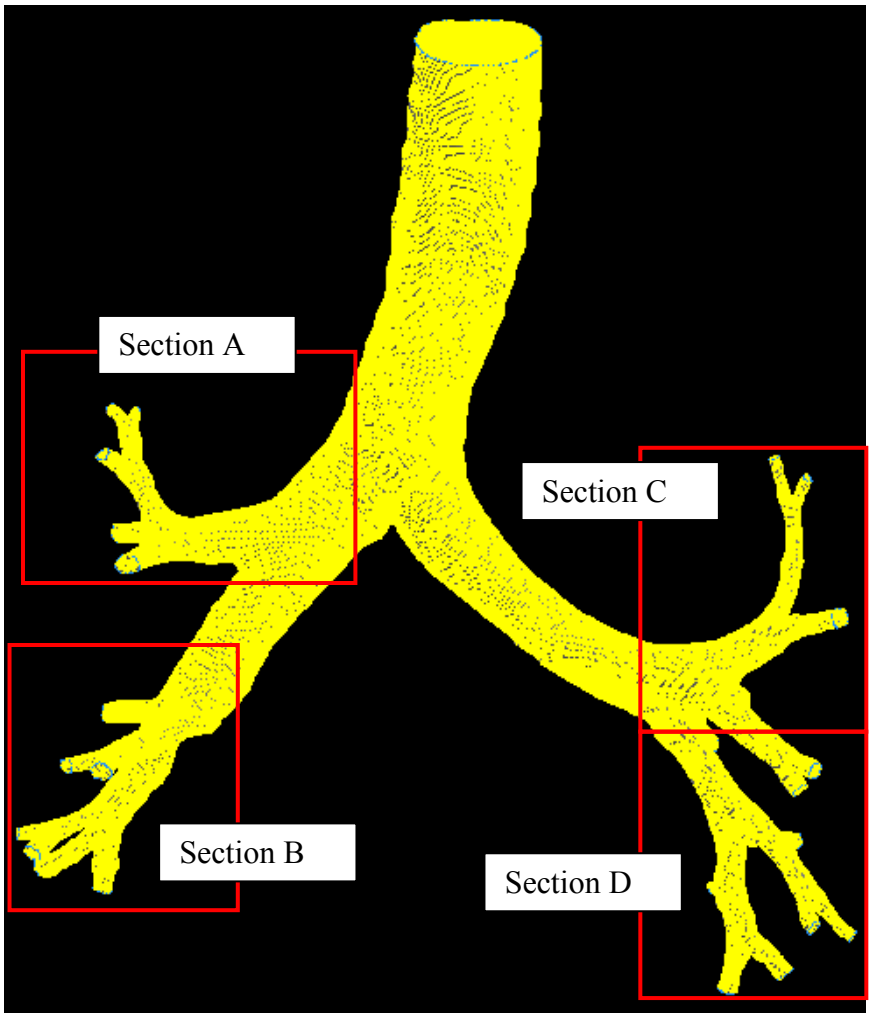

Figure 6.7: Surface volume mesh generated in GAMBIT for the real airway geometry. The geometry was extracted using chest CT image data obtained from University Hospitals at University of Missouri.

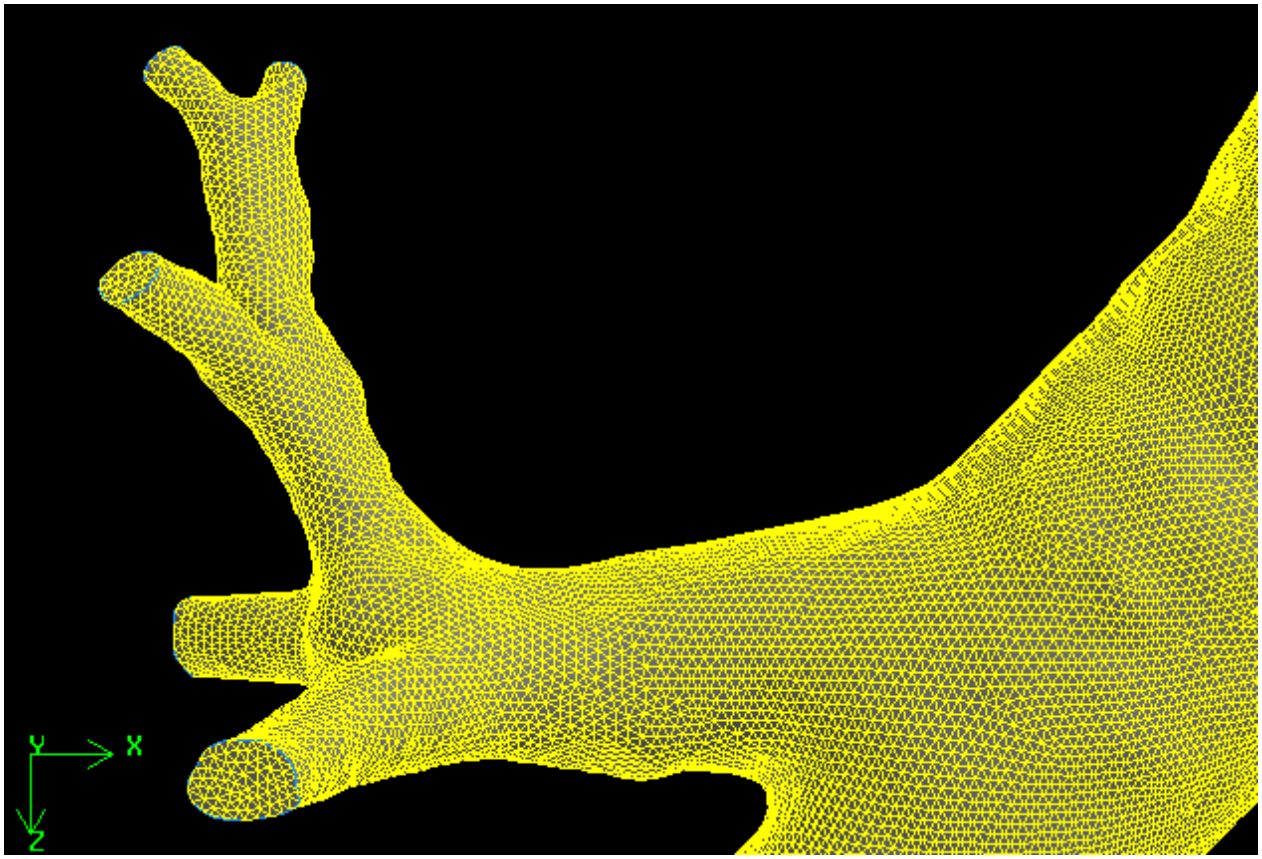

Figure 6.8: Detail on the section A in Figure 6.7

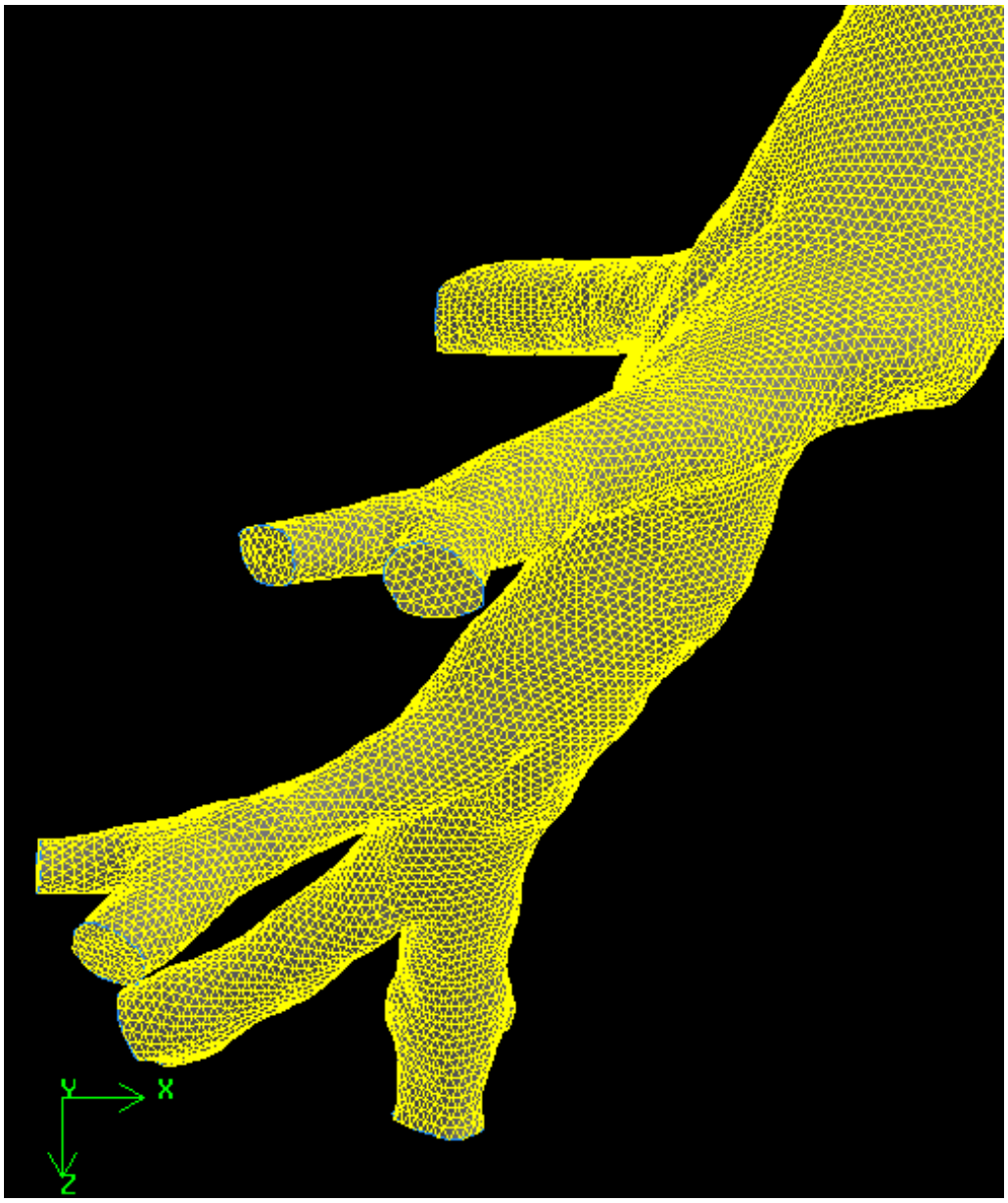

Figure 6.9: Detail on the section B in Figure 6.7

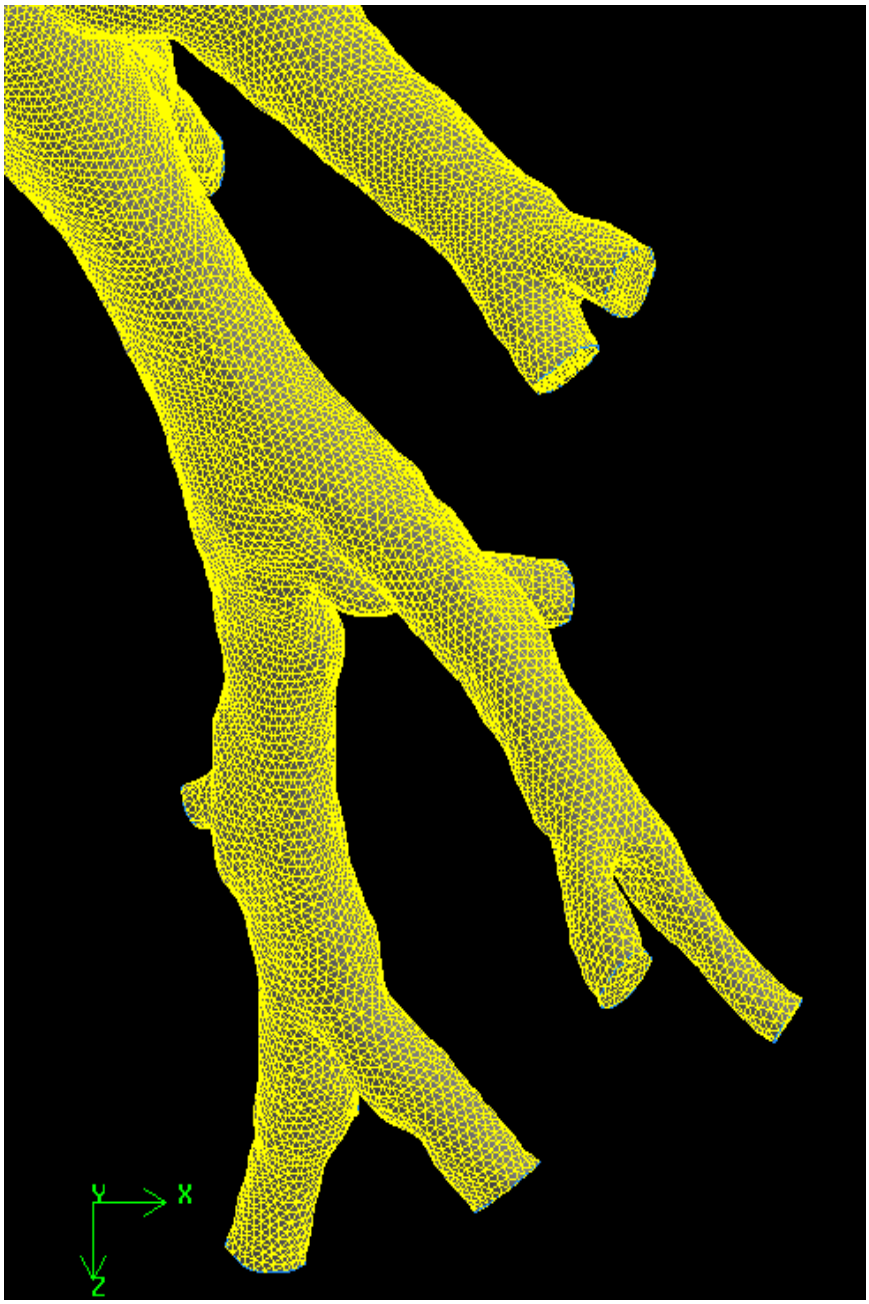

Figure 6.10: Detail on the section C in Figure 6.7

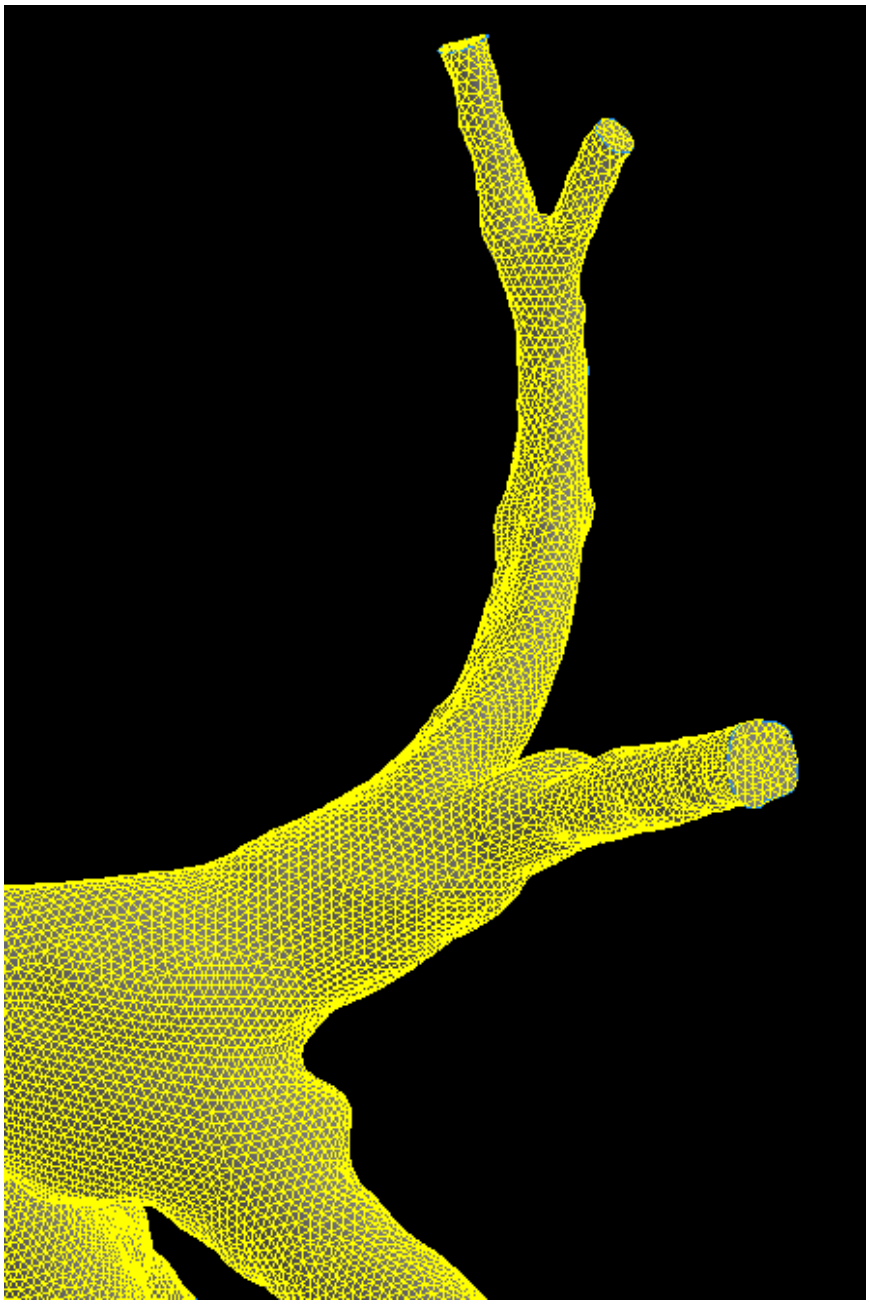

Figure 6.11: Detail on the section D in Figure 6.7

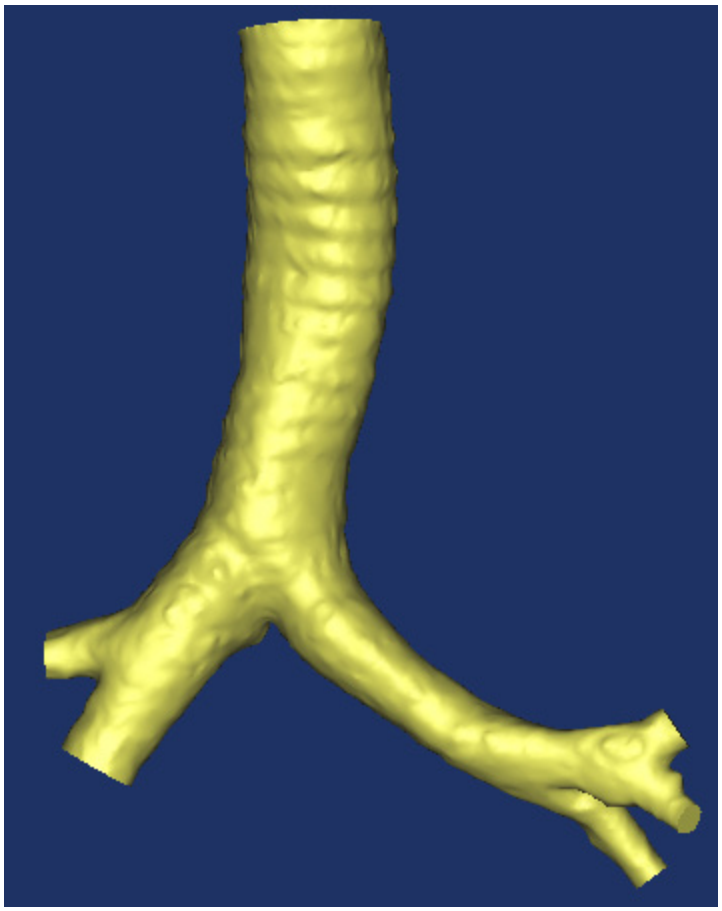

Figure 6.12: Simplified geometry after cutting and removing the end bifurcations on the geometry in Figure 6.5 (b)

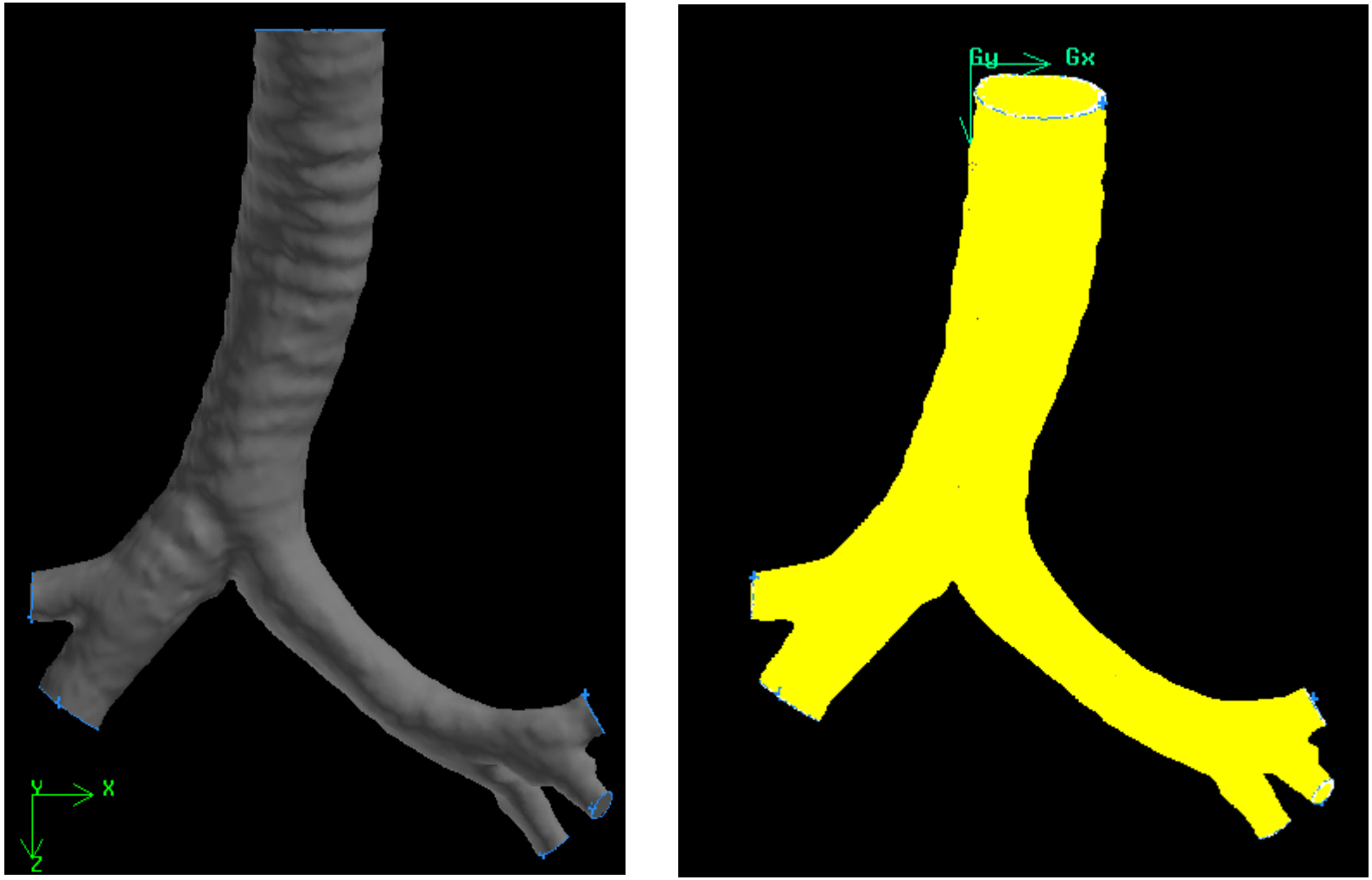

(a) (b)

Figure 6.13: (a) Lung airway geometry trimmed to fewer bifurcations. The ridged airway surface is clearly visible in this picture. (b) Volume mesh generated for the finalized airway geometry

6.3 CFD Computation

The mesh file generated from GAMBIT pre-processor with defined inlet, outlet and wall surfaces was imported into FLUENT program. The geometry was scaled down 1000 times in dimension as the initial data was provided in mm whereas the default units in FLUENT is meters (m). Air flow was modeled to study the flow patterns in this geometry initially. The inlet boundary condition is defined with flow velocity of 1 $m.s^{-1}$ at room temperature. FLUENT computation was run and the results obtained are discussed.

The simplified real lung airway volume has 8213456 computational volumes or cells. This large number of computational cells is very demanding in terms of computational resources. The contours of flow velocity magnitude are presented in Figure 6.14 on surfaces parallel to XZ plane intersection the lung airway volume. It is observed that the flow velocity has increased considerably in small bifurcations. Figure 6.15 shows the flow path lines in the flow domain and clearly observe the increase in flow velocity in smaller airway bifurcations.

6.3.1 Species Transport and Reaction model for Po-218 deposition

Using the species transport and reaction model for Po-218 deposition discussed in previous chapter, surface deposition rates of Po-218 species are computed on the lung airway wall surface as shown in Figure 6.16. Light breathing activity is considered with inspiratory flow rate of 350 $cm^3.s^{-1}$ corresponding to an average tidal volume of 750 cm^3. The average inlet air flow speed calculated for these conditions is 0.75 $m.s^{-1}$. Other deposition model parameters remain the same as in the simple bifurcation geometries.

6.3.2 Discrete phase model

Particle deposition was also studied using Discrete Phase Model (DPM) in to get predict the deposition efficiencies for 100 nm carbon nanoparticles entering the airway at 1 $m.s^{-1}$ (slightly higher inspiratory flow rate as compared to Po-218 deposition model for real lung airway geometry) and a mass flow rate of 1×10^{-7} $kg.s^{-1}$. Figure 6.13 shows the contours of particle concentration on the wall surface of the airway geometry obtained from the DPM model. DPM model was used to study carbon particle deposition efficiency in the real lung airway geometry for different particle sizes. The inlet air flow rate was 1 $m.s^{-1}$ and particle mass flow rate was 1×10^{-7} $kg.s^{-1}$ in all cases. The deposition efficiencies obtained are tabulated and presented in Table 6.1.

The complete airway geometry extracted in this research will provide better understanding of the particle deposition. We have used the complex airway geometry to study the airflow and particle deposition using DPM model. Airflow pathlines in the complex airway geometry are shown in Figure 6.19. Particle deposition was also studied using DPM model to predict the deposition efficiencies for 100 nm carbon nanoparticles entering the airway at 1 $m.s^{-1}$ and a mass flow rate of 1×10^{-7} $kg.s^{-1}$. Figure 6.20 shows the contours of particle concentration on the wall surface of the airway geometry obtained from the DPM model.

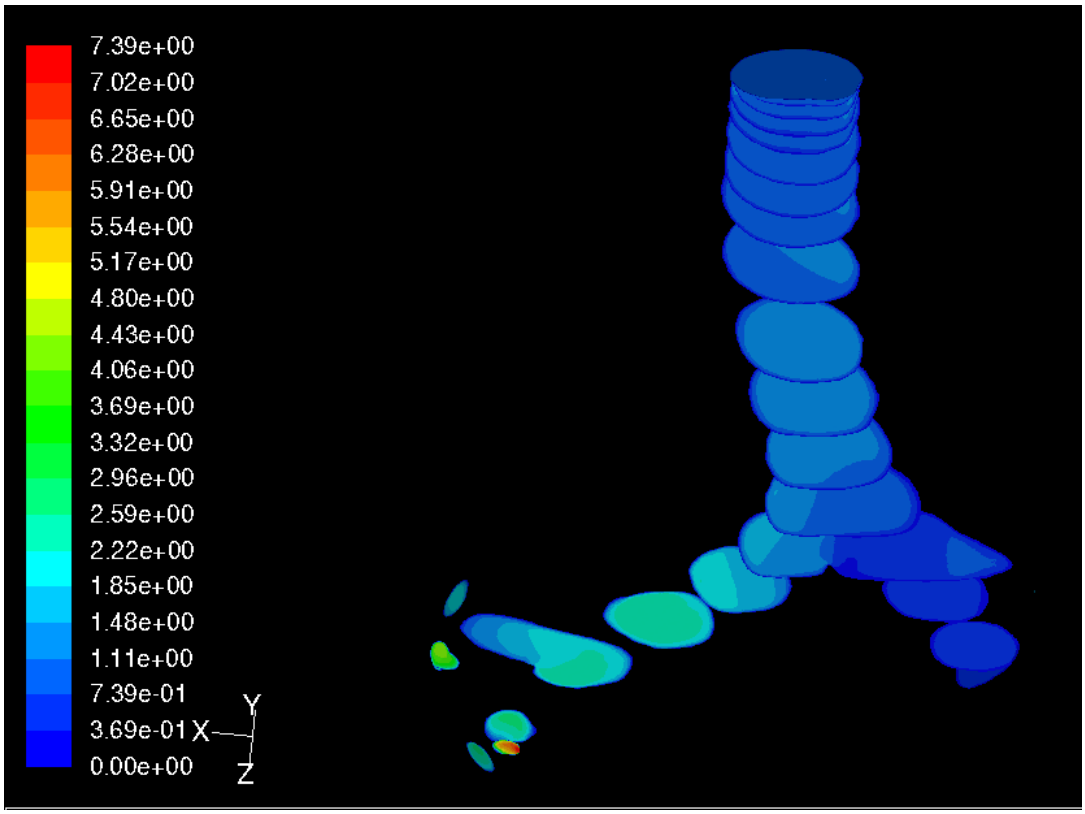

Figure 6.14: Contours of velocity magnitude for air flow in the simplified real lung airway geometry

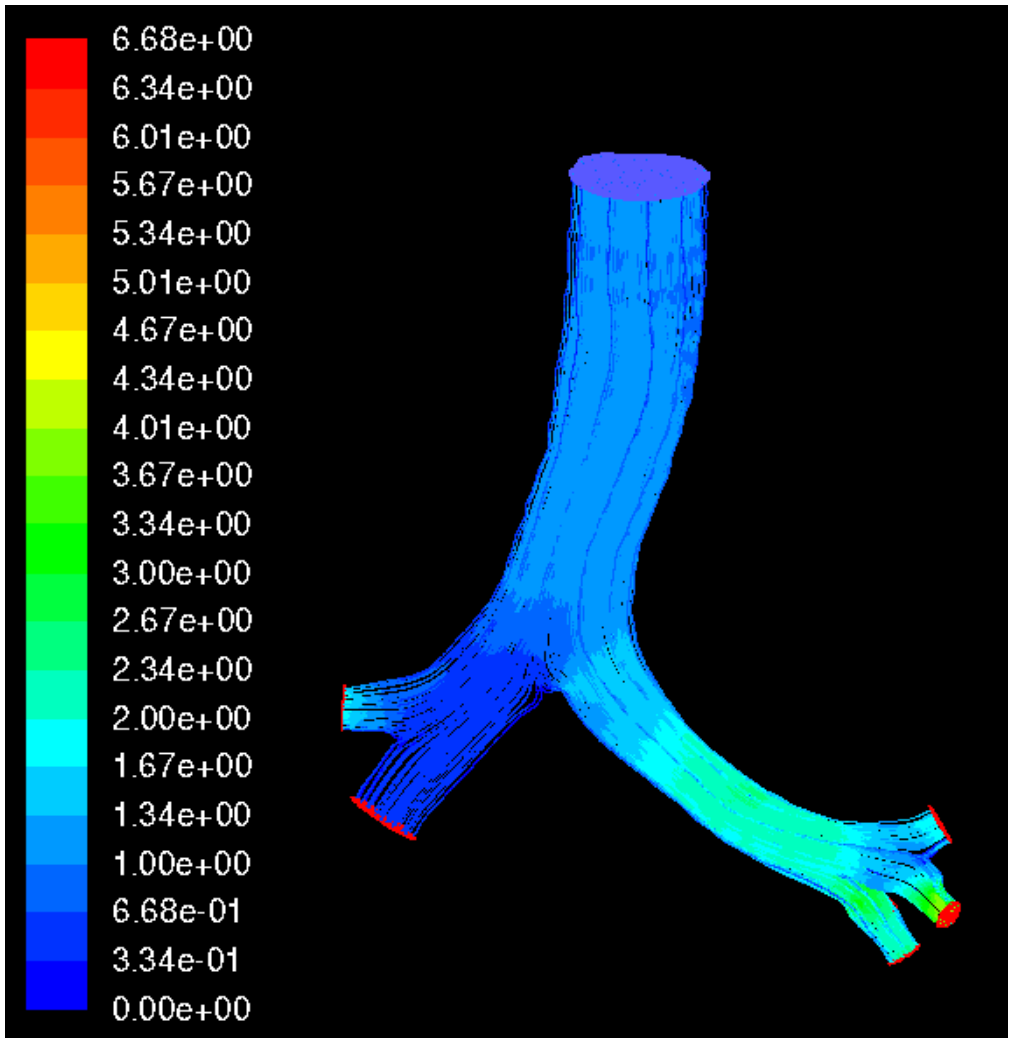

Figure 6.15: Air flow pathlines in the simplified real lung airway geometry for inlet flow velocity of 1 m s^{-1}

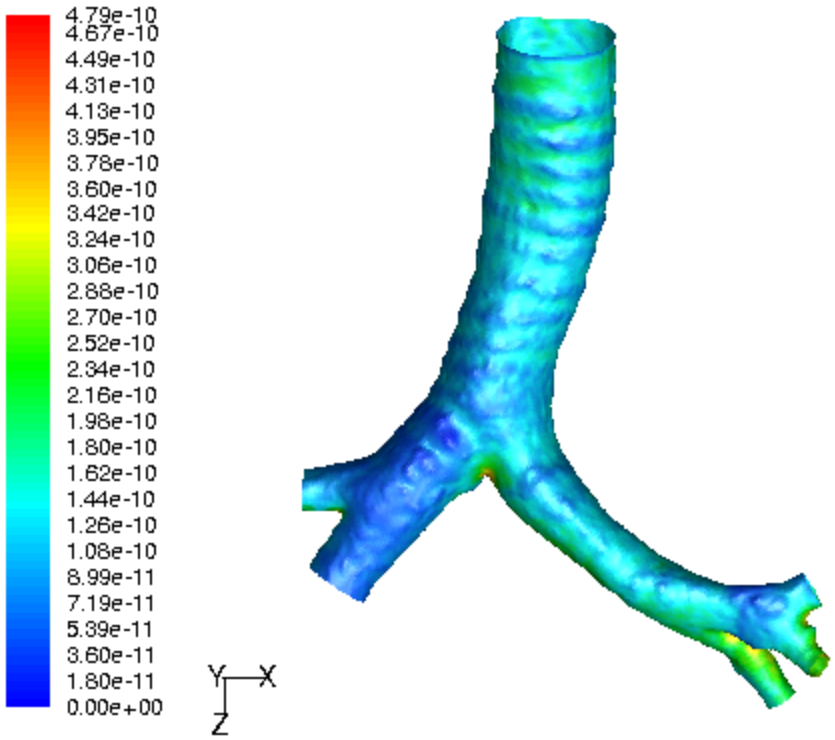

Figure 6.16: Surface contours of deposition rate of Po-218 species on the simplified real lung airway geometry developed here. The inlet flow direction is perpendicular to the inlet face and is fully developed with an average inlet speed of 0.25 $m.s^{-1}$ corresponding to light activity breathing rate of 454 $cm^3.s^{-1}$.

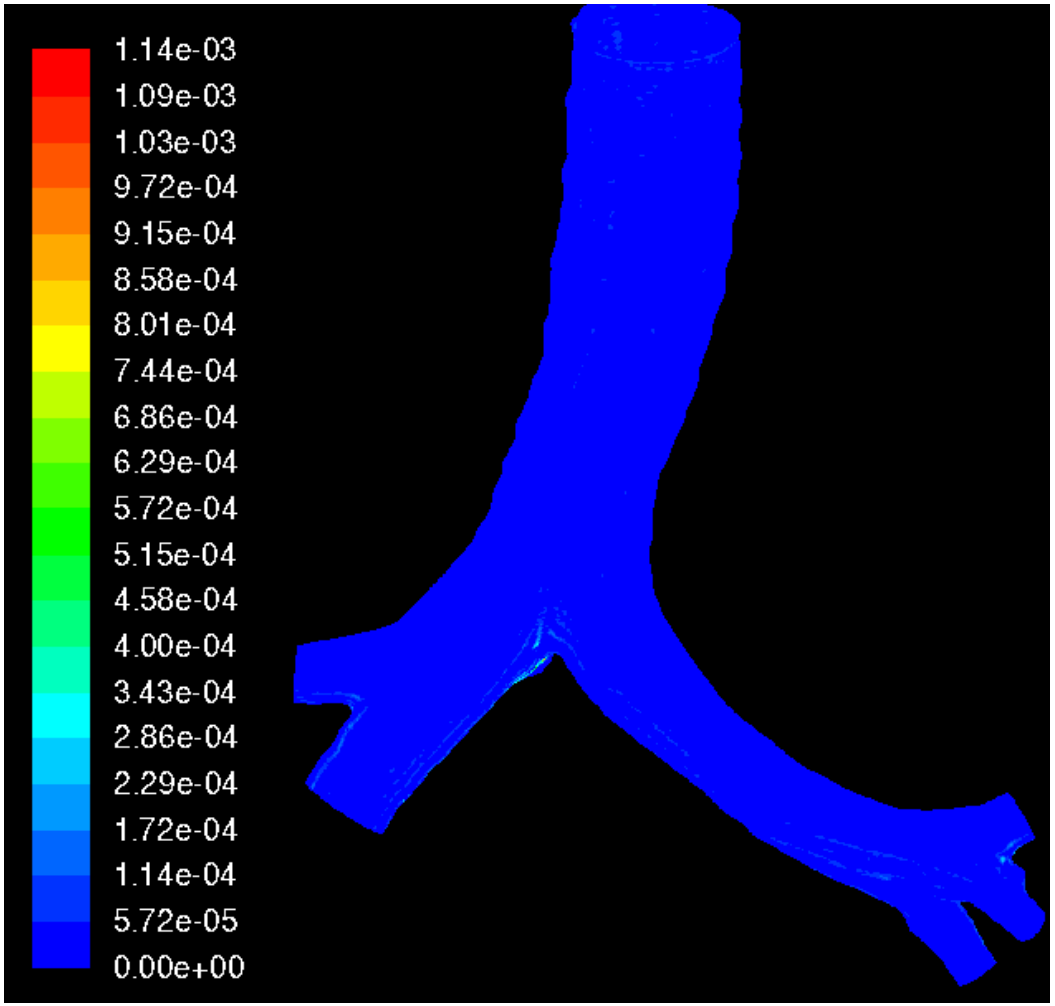

Figure 6.17: Contours of surface concentration of 100 nm carbon particles deposited on the wall surface that were injected at the inlet face with mass flow rate of 1×10^{-7} kgs^{-1} in DPM model

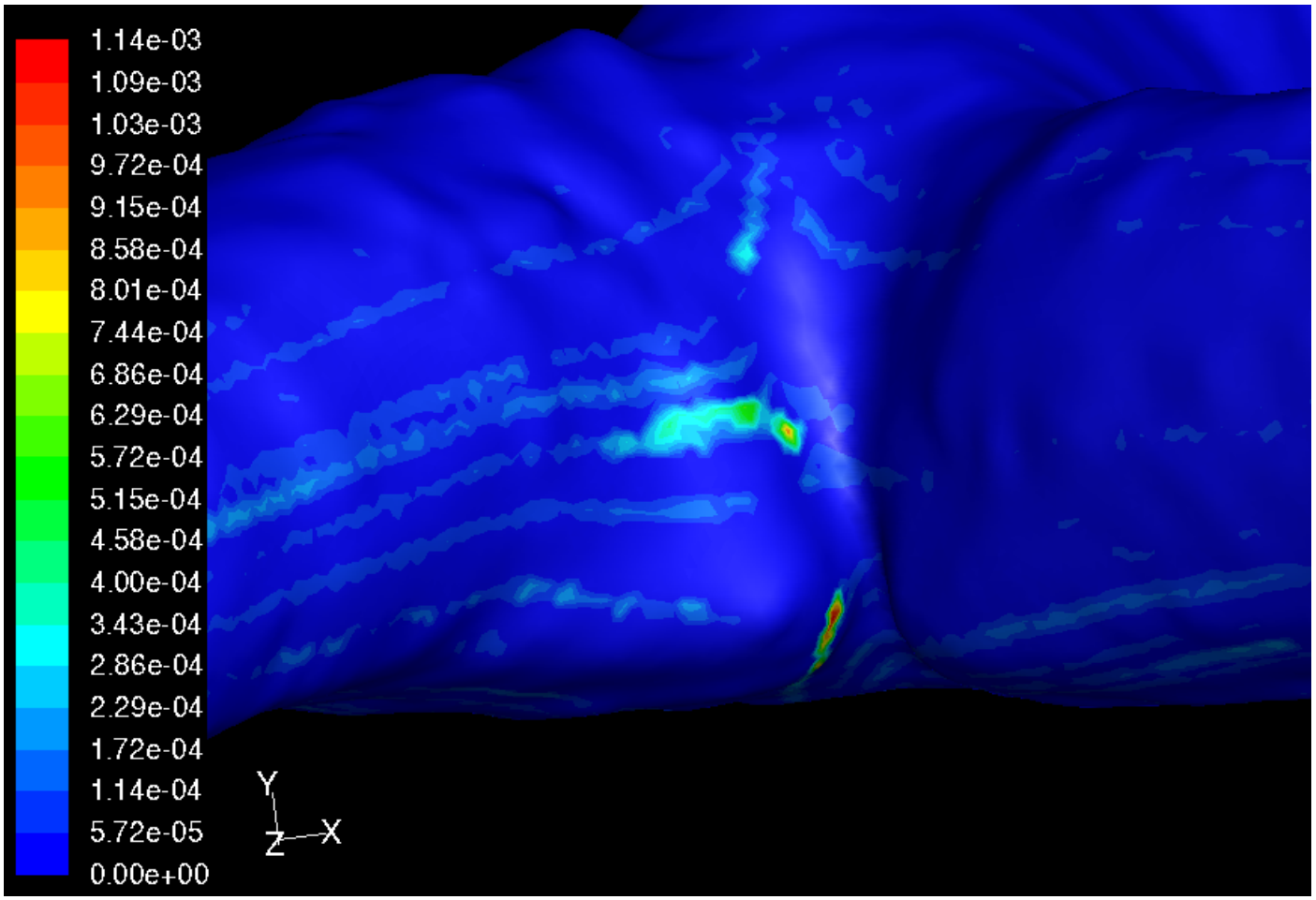

Figure 6.18: Contours of surface concentration at the carina of 100 nm carbon particles deposited on the wall surface that were injected at the inlet face with mass flow rate of 1×10^{-7} kgs^{-1} in DPM model

We have used this DPM model to study carbon particle deposition efficiency in the real lung airway geometry for different particle sizes. The inlet air flow rate was 1 $m.s^{-1}$ and particle mass flow rate was 1×10^{-7} $kg.s^{-1}$ in all cases. The deposition efficiencies obtained are tabulated and presented in Table 6.1

Table 6.1: Carbon nanoparticle deposition efficiencies computed using DPM model in FLUENT CFD code in simplified real lung airway geometry

Carbon nanoparticle size (nm)	**Computed deposition efficiency (%)**
100	2.32
200	2.3
400	2.32
600	2.36
800	2.46
1000	2.46

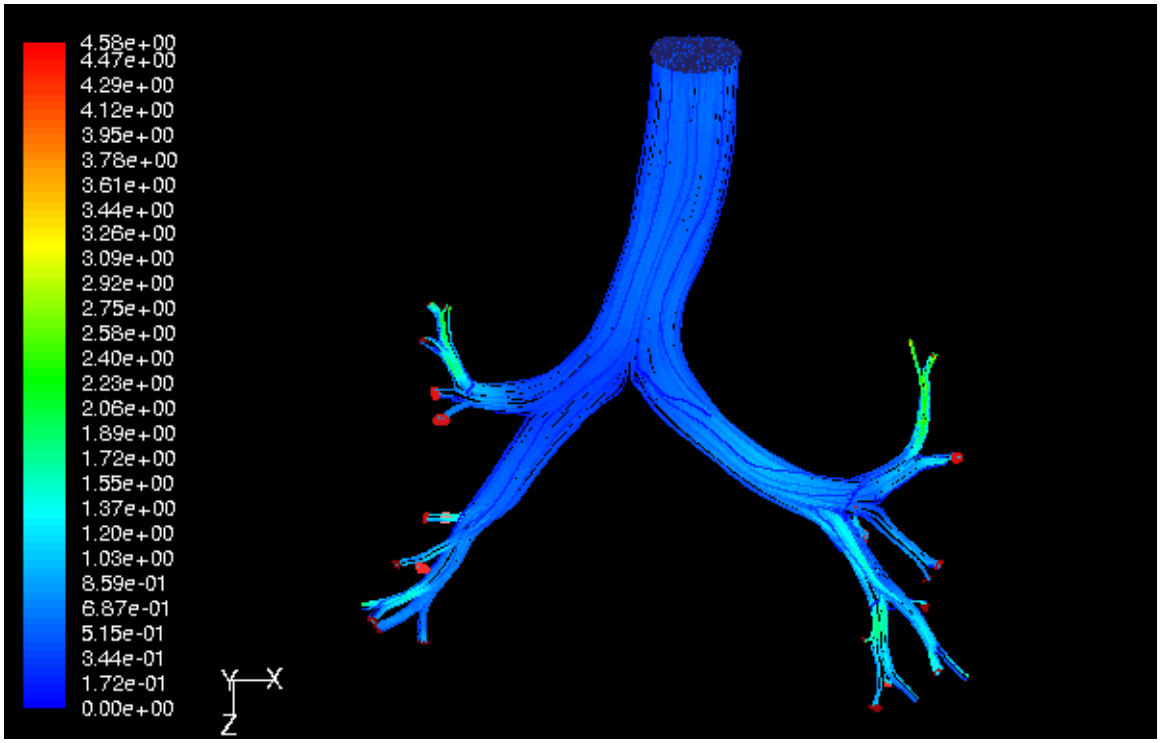

Figure 6.19: Air flow pathlines in real lung airway geometry for inlet flow velocity of 1 m s^{-1}

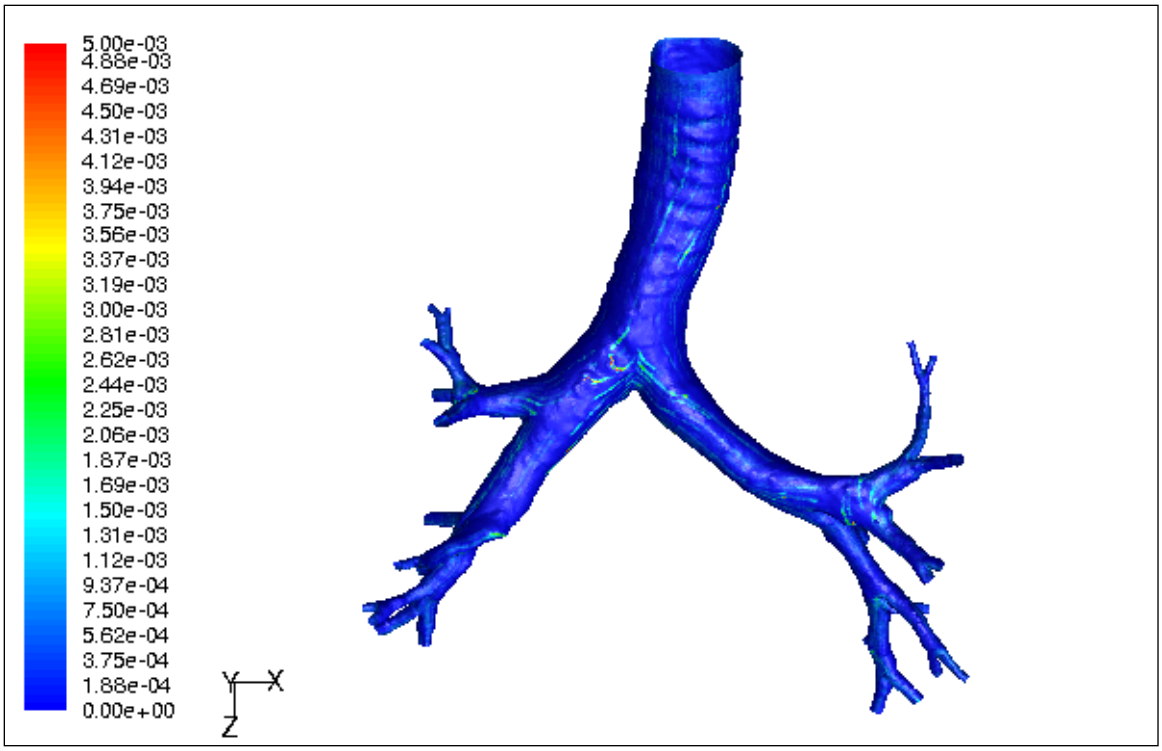

Figure 6.20: Contours of surface concentration at the carina of 100 nm carbon particles deposited on the wall surface that were injected at the inlet face with mass flow rate of 1×10^{-7} kg.s^{-1} in DPM model

CHAPTER VII

DISCUSSIONS AND CONCLUSIONS

This research was directed towards modeling deposition of aerosols particles due to thermophoresis and in lungs. Some limited experiments were conducted to study thermophoretic deposition in straight cylindrical tubes.

A numerical technique was explored to solve the coupled equations for solving the energy and particle continuity equations included with thermophoresis effect to obtain accurate results for thermophoretic deposition. The numerical technique was verified with the analytical solution of Graetz equation for temperature profiles in a cylindrical tube. Deposition efficiencies computed from the present numerical technique compare well with the values calculated from the theoretical expressions published [31,42,49] and also with the experimental data (with some assumptions with respect to the thermophoretic coefficient) from Romay et.al. [44]. CFD code Fluent was also used to calculate the thermophoretic deposition efficiency and results from Fluent computations compared well with that from our numerical work, but in some cases very fine mesh near the tube wall surface was required for accurate results.

It is to be noted that currently some major research efforts are directed towards high end computing (up to 100000 processors) and creation of advanced computer codes that eventually will replace the existing codes in many areas of nuclear engineering. The programs will focus on fine grid computations (among other areas), as it is being realized that coarse meshes with some grid adaptations also at times miss out on actual physics. Thermophoresis is one of such problems as one encounters a double boundary layer. The

mesh resolution near the wall does affect the results as the thermophoretic layer is rather thin and our work indeed clarifies that the dependence of results on grid resolution, and found that very fine grid is needed to resolve the boundary layer, and hence for accurate results. This work is planned to PBMR geometries where geometries are complex, and particles are present in the flow systems even under regular operating conditions.

Particle deposition model developed for polonium-218 deposition compared very well with the available experimental data by Kinsara et.al. This gives the confidence in the deposition model developed in this work. Further, realistic airway geometry for 3^{rd} and 4^{th} generation bifurcation was constructed and deposition patterns were computed.

Successfully real human lung airway geometry from chest CT scan image data was successfully completed using image segmentation tools in Amira software program. The procedure of CT scan image segmentation followed by surface generation is very laborious and time consuming. Every image of the data has to be carefully analyzed and contoured for the selection of the lung airway geometry. The surface analysis and cleanup process in mimics program was also laborious but simple to use with the available tools and surface quality testing algorithms. The volume generation in GAMBIT program was the toughest with respect to the technique and procedure involved. This volume creation technique was self developed after continuous testing of different techniques and methods. The volume mesh generated 8213456 computational volumes or cells, which is a large and is demanding on the computer hardware resources.

The deposition efficiencies calculated using the DPM model in FLUENT code for carbon nanoparticles of diameters ranging from 100 nm to 1000 nm were very similar

ranging from 2.32 % to 2.46 %. In this computation, the volume is re-meshed for a coarse mesh with only 1813432 volume cells. Volume re-meshing was performed to let the computations run faster for quicker results. The deposition efficiencies obtained here clearly indicate that the mesh resolution should be finer to get more accurate numbers for deposition efficiencies.

REFERENCES

1. Fuchs, N. A., **The Mechanics of Aerosols**, Pergamon Press, Oxford, 1964.
2. Davis, E. J. and Schweiger, G., **The Airborne Microparticle**, Springer, Berlin, 2002.
3. Friedlander, S. K., **Smoke, Dust and Haze**, 2nd edition, Oxford University Press, New York, 2000.
4. Ivchenko, I. N., Loyalka, S. K. and Tompson, R. V., **Analytical Methods for Problems of Molecular Transport**, Springer, Dordrecht, Netherlands, 2007.
5. Williams, M. M. R. and Loyalka, S. K., **Aerosol Science: Theory and Practice, with Special Applications to the Nuclear Industry**, Pergamon Press, Oxford, 1991.
6. Hinds W. C., **Aerosol Technology: Properties, Behavior, and Measurement of Airborne Particles**, John Wiley & Sons Inc., 1982.
7. Brock, J. R., "On the Theory of Thermal Forces Acting on Aerosol Particles," *Journal of Colloid and Interface Science*, **17**, 768 (1962).
8. Tompson, R.V. and Loyalka, S.K., "Condensational growth of a spherical droplet: free molecular limit," *Journal of Aerosol Science,* **17**(4), 723-728 (1986).
9. Loyalka, S.K. and Hamoodi, S.A., "Poiseuille flow of a rarefied gas in a cylindrical tube: solution of linearized Boltzmann equation," *Physics of Fluids: A-Fluid Dynamics*, **2**(11), 2061-2065 (1990).
10. Zheng, F., "Thermophoresis of spherical and non-spherical particles: a review of theories and experiments," *Advances in Colloid and Interface Science*, **97**, 255 (2002).

11. Hyder, J. and Gehr, P., **Particle-Lung Interactions (Lung Biology in Health and Disease – Vol. 143,** Marcel Dekker, Inc., New York, 2000.

12. ICRP publication 66, "Human Respiratory Tract Model for Radiological Protection, *Annals of ICRP*, 24, 1995.

13. NCRP report No. 125, "Deposition, Retention and Dosimetry of Inhaled Radioactive Substances" (1997).

14. Harley, N.H and Harley J.H., "Potential lung cancer risk from indoor radon exposure". *CA: A Cancer Journal for Clinicians*, **40**(5), 265-275 (1990).

15. Hofmann W., "Overview of Radon Lung Dosimetry," *Radiation Protection Dosimetry*, **79**, 229-236 (1998).

16. Hofmann W., Heistracher T., and Báláshazy I., "Deposition of Inhaled Radon Decay Products in Human Bronchial Airway Bifurcations," *Environmental International*, **22**, S935-S940 (1996).

17. Burton, R.T., Issacs, K.K., Fleming, J.S., Martonen, T.B., "Computer Reconstruction of Human Lung Boundary Model From Magnetic Resonance Images," *Respiratory Care*, **49**(2), 180-185 (2004).

18. Zhang Y., Finlay W.H., "Measurement of the Effect of cartilaginous Rings on Particle Deposition in a Proximal Lung Bifurcation Model," *Aerosol Science and Technology*, **39**, 394-399 (2005).

19. Broday D.M., "Deposition of Ultrafine Particles at Carinal Ridges of the Upper Bronchial Airways," *Aerosol Science and Technology*, **38**, 991-1000 (2004).

20. Sauret V., Halson P.M., Brown I. W., Fleming J. S., Bailey A. G., "Study of the three-dimensional geometry of the central conducting airways in man using computed tomographic (CT) images," *Journal of Anatomy*, **200**, 123-134 (2000).

21. Weibel, E.R., **Morphometry of the Human Lung,** Academic Press, New York, 1963.

22. Weibel, E. R., **Design of airways and blood vessels as branching trees, in The Lung: Scientific Foundations**, Vol. I, Crystal, R.G., West, J.B., Barnes, P.J., Cherniak, N.S., and Weibel E.R., Raven Press, New York, 1991.

23. Mously K. A., **Numerical Modeling of Po-218 Deposition in Physiologically Realistic Lung Bifurcation Model**, Ph.D. dissertation, University of Missouri, 1997.

24. Koblinger L., and Hofmann W., "Analysis of human lung morphometric data for stochastic aerosol deposition calculations," *Physics in Medicine and Biology*, **30**(6), 541-556 (1985).

25. Liu Y, So R.M.C., Zhang C.H., "Modeling the bifurcating flow in an asymmetric human lung airway," *Journal of Biomechanics*, **36**, 951-959 (2003).

26. Loyalka, S.K., "Thermophoretic Force on a Single Particle – I. Numerical Solution of the Linearized Boltzmann Equation," *Journal of Aerosol Science*, **23**(3), 291 (1992).

27. Li, W. and Davis, E.J., "Measurement of the thermophoretic force by electrodynamic levitation: Microspheres in air," *Journal of Aerosol Science*, **26**(7), 1063, (1995).

28. Brock, J.R., "The Thermal Force in the Transition Region," *Journal of Colloid Science*, **23**, 448, (1967).

29. Stratmann, F. and Fissan, H., "Convection, Diffusion, and Thermophoresis in Cooled Laminar Tube Flow," *Journal of Aerosol Sciences*, **19**, 793, (1988).

30. Montassier, N., Boulaud, D., Stratmann, F. and Fissan, G., "Comparison between experimental study and theoretical model of thermophoretic particle deposition in laminar tube flow," *Journal of Aerosol Science*, **21**(suppl. 1), S85, (1990).

31. Montassier, N., Boulaud, D. and Renoux, A., "Experimental study of thermophoretic particle deposition in laminar tube flow," *Journal of Aerosol Science*, **22**(5), 677, (1991).

32. He, C. and Ahmadi, G., "Particle Deposition with Thermophoresis in Laminar and Turbulent Duct Flows," *Aerosol Science and Technology*, **29**, 525, (1998).

33. Shimada, M., Okuyama, K. and Asai, M., "Deposition of Submicron Aerosol Particles in Turbulent and Transitional Flow," *AIChe Journal*, **39**, 17, (1993).

34. Ye, Y., Pui, D. Y. H., Liu, B. Y. H., Opiolka, S. and Fissan, H., "Thermophoretic effect of particle deposition on a free standing semiconductor wafer in a clean room," *Journal of Aerosol Science*, **22**, 63, (1991).

35. Boyack, B.E., Corradini, M.L., Denning, R.S., Khatib-Rahbar, M., Loyalka, S.K., and Smith, P.N., CONTAIN Independent Review, LA-12866, 1995.

36. Loyalka, S.K., Tompson, R.V., and Sher, R., "Thermophoretic Aerosol Deposition: Some Modeling Considerations," *Transactions American Nuclear Society*, **65**, 373 (1992).

37. Fernandes, A. and Loyalka, S.K., "Modeling of Thermophoretic Aerosol Deposition in Nuclear Reactor Containment," *Nuclear Technology*, **116**(3), 270 (1996).

38. V.R. Gutti, and S.K. Loyalka, "Thermophoretic Deposition in a Cylindrical Tube: Computations and Comparison with Experiments," *Nuclear Technology,* **166**, 121-133 (2009).

39. Byers, R.L. and Calvert, S., "Particle Deposition from Turbulent Streams by means of Thermal Force," *Industrial & Engineering Chemistry Fundamentals*, **8**(4), 646 (1969).

40. Nishio, G., Kitani, S., and Takahashi, K., "Thermophoretic deposition of aerosol particles in a heat-exchanger pipe," *Industrial & Engineering Chemistry Process Design and Development*, **13**(4), 408 (1974).

41. Walker, K.L., Homsy, G.M. and Geyling, R.T., "Thermophoretic deposition of small particles in laminar tube flow," *Journal of Colloid and Interface Science*, **69**(1), 138 (1979).

42. Batchelor, G.K. and Shen, C., "Thermophoretic deposition of particles in gas flowing over cold surface," *Journal of Colloid and Interface Science*, **107**(1), 21 (1985).

43. Stratmann, F., Otto, E. and Fissan, H., "Thermophoretic and diffusional particle transport in cooled laminar tube flow," *Journal of Aerosol Science*, **25**(7), 1305 (1994).

44. Romay, F.J., Takagaki, S.S., Pui, D.Y.H. and Liu B.Y.H., "Thermophoretic deposition of aerosol particles in turbulent pipe flow," *Journal of aerosol Science*, **29**(8), 943 (1998).

45. Lin, J.-S. and Tsai, C. –J., "Thermophoretic deposition efficiency in a cylindrical tube taking into account developing flow at the entrance region," *Journal of Aerosol Science*, **34**, 569 (2003).

46. Housiadas, C. and Drossinos, Y., "Thermophoretic Deposition in Tube Flow," *Aerosol Science and Technology*, **39**, 304 (2005).

47. Lin, J.-S., Tsai, C. –J. and Chang, C. –P., "Suppression of particle deposition in tube flow by thermophoresis," *Journal of Aerosol Science*, **35**, 1235 (2004).

48. Peter, Frolkovic, "Tricks of the Trade: Discretized PDE," *The Mathematica Journal*, **5**(2), (1995).

49. Shah, R.K. and London, A.L., **Laminar Flow Forced Convection in Ducts: A Source Book for Compact Heat Exchanger Analytical Data**, Academic Press, NewYork, 1978.

50. Kays, W.M., **Convective Heat and Mass Transfer**, McGraw-Hill, NewYork, 1980.

51. Davis, E.J., "Exact Solutions for a Class of Heat and Mass Transfer Problems," *The Canadian Journal of Chemical Engineering*, **51**(5), 562 (1973).

52. Lauwerier, H.A., "The use of confluent hupergeometric function in mathematica physics and the solution of an eigenvalue problem," *Applied Scientific Research*, **2**(1), 184 (1951).

53. Talbot, L., Cheng, R.K., Schefer R.W. and Willis D.R., "Thermophoresis of particles in a heated boundary layer," *Journal of Fluid Mechanics*, **101**, 737 (1980).

54. "CONTAIN 1.2 Code Manual, A Computer Code for Severe Accident Analysis," Sandia national Laboratories, Albuquerque, New Mexico. Prepared for U. S. Nuclear Regulatory Commission (1993).

55. Gauntt, R., "MELCOR Computer Code manuals: Primer and User's Guide," Version 1.8.5, Rev.2, Vol. 1 (2000).

56. Bixler, N., "VICTORIA 2.0: A Mechanistic Model for Radionuclide Behavior in a Nuclear Reactor Coolant System under Severe Accident Conditions," (1998).

57. Lide, D. R., "*CRC Handbook of Physics and Chemistry*," 88th Edition, (2007).

58. Ferziger J.H. and Peric M., **Computational Methods for Fluid Dynamics**, Springer-verlag Berlin, 1996.

59. Graphite Aerosol Generator User Guide, Palas® GmbH.

60. Series 3080 Electrostatic Classifiers Operation and Service Manual, TSI Inc.

61. Model 3776 Ultrafine Condensation Particle Counter Operation and Service manual, TSI Inc.

62. Kinsara, A. A.; Tompson, R. V.; Loyalka, S. K., "Computational Flow and Aerosol Concentration Profiles in Lung Bifurcations," *Health Physics*, **64**, 13-22 (1993).

63. Davies C.N., "A formalized anatomy of the human respiratory tract," in **Inhaled Particles and Vapors**, edited by Davies C.N. Permagon Press, Oxford, UK, 1961, pp. 82-87.

64. Horsfield K., Dart G., Olson D.E., Filley G.F., and Cumming G., "Models of the human bronchial tree," *Journal of Applied Physiology*, **31**(2), 207-217 (1971).

65. Yeh H.C., and Schum, G.M., "Models of human lung airways and their application to inhaled particle deposition," *Bulletic of Mathematical Biology* **42**(3), 461-480 (1980).

66. Báláshazy I., and Hofmann W., "Deposition of aerosols in asymmetric airway bifurcations," *Journal of Aerosol Science*, **26**, 273-292 (1995).

67. Báláshazy I., Hofmann W., and Heistracher T., "Computation of local enhancement factors for the quantification of particle deposition patterns in airway bifurcations," *Journal of Aerosol Science*, **30**, 185-203 (1999).

68. Báláshazy I., Hofmann W., and Heistracher T., "Local Particle Deposition Patterns may Play a Key Role in the Development of Lung Cancer," *Journal of Applied Physiology*, **94**, 1719-1725 (2003).

69. Hofmann W., Mainelis G., Mohamed A., Báláshazy I., Vaupotic J., and Kobal I., "Comparison of different Modeling Approaches in current Lung dosimetry Models," *Environmental International*, **22**, S965-S976 (1996).

70. Comer J.K., Kleinstreuer C., and Kim C.S., "Flow structures and particle deposition patterns in double-bifurcation airway models. Part2. Aerosol transport and deposition," *Journal of Fluid Mechanics*, **435**, 55-80 (2001).

71. Zhang Z., Kleinstreuer C., and Kim C.S., "Cyclic micron-size particle inhalation and deposition in a triple bifurcation lung airway model," *Journal of Aerosol Science*, **33**, 257-281 (2002).

72. Martonen T.B., Musante C.J., Segal R.A., Schroeter J.D., Hwang D., Dolovich M.A., Burton R., Spencer R.M., and Fleming J.S., "Lung Models: Strengths and Limitations," *Respiratory Care*, **45**(6), 712-736 (2000).

73. Martonen T.B., Isaacs K., and Hwang D., "Three-Dimensional Simulations of Airways within Human LungsCell," *Biochemistry and Biophysics*, **42**, 223-249 (2005).

74. Martonen T.B., Yanh Y., and Xue Z., "Influences of cartilaginous rings on tracheobronchial fluid dynamics," *Inhalation Toxicology*, **6**, 185-203 (1994).

75. Martonen T.B., Zhang Z., and Yang Y., "Airway surface irregularities promote particle diffudion in the human lung," *Radiation Protection Dosimetry*, **59**, 5-14 (1995).

76. Martonen T.B., Zhang Z., and Yang Y., "particle diffusion from developing flows in rough-walled tubes," *Aerosol Science and Technology*, **26**, 1-11 (1997).

77. Nowak N., Kakade P.P., and Annapragada A.V., " Computational Fluid Dynamcis Simulation of Airflow and Aerosol Deposition in Human Lungs," *Annals of Biomedical Engineering*, **31**, 374-390 (2003).

78. Cebral J.R., and Summers R.M., "Tracheal and Central Bronchial Aerodynamics Using Virtual Bronchoscopy and Computational Fluid Dynamics," *IEEE Transactions on Medical Imaging*, **23**(8), 1021-1033 (2004).

79. Ertbruggen C.V., Hirsch C., and Paiva M., "Anatomically Based Three-Dimensional Model of Airways to Simulate Flow and particle Transport Using Computational Fluid Dynamics," *Journal of Applied Physiology*, **98**, 970-980 (2005).

80. Aykac D., Hoffman E.A., McLennan G., Reinhardt J.M., "Segmentation and analysis of the human airway tree from three-dimensional x-ray CT images," *IEEE Transactions on Medical Imaging*, **22**(8), 940-950 (2003).

81. Perzl M.A., Schulz H., Paretzke H.G., Englmeier K.H., Hyder J., "Reconstuction of the lung geometry for the simulation of aerosol transport," *Journal of Aerosol Medicine*, **9**(3), 409-418 (1990).

82. Smith S., Cheng Y.S., and Yeh H.C., "Deposition of Ultrafine Particles in Human Tracheobronchial Airways of Adults and Children," *Aerosol Science and Technology*, **35**, 697-709 (2001).

83. Zhou Y., and Cheng Y.S., "Particle Deposition in a Cast of Human Tracheobronchial Airways," *Aerosol Science and Technology*, **39**, 492-500 (2005).

84. Kinsara A.A., Loyalka S.K., Tompson R.V., Miller W.H., and Holub R.F., "Deposition Patterns of Molecular Phase Radon Progeny (218Po) in Lung Bifurcations," *Health Physics*, **68** (3), 371-382 (1995).

85. Su W.C., and Cheng Y.S., "Fiber Deposition Pattern in Two Human Respiratory Tract Replicas," *Inhalation Toxicology*, **18**, 749-760 (2006).

86. Annapragada, A., Mishchiy, N., "In silico modeling of aerosol deposition in lungs," *Drug Discovery Today: Disease Models*, **4**(3), 155-161 (2007).

87. Báláshazy I., and Hofmann W., "Particle Deposition in airway bifurcations-I. Inspiratory Flow," *Journal of Aerosol Science*, **24**(6), 745-772 (1993).

88. Báláshazy I., and Hofmann W., "Particle Deposition in airway bifurcations-II. Expiratory Flow," *Journal of Aerosol Science*, **24**(6), 773-786 (1993).

89. Báláshazy I., and Hofmann W., "Quantifications of Local Deposition Patterns of Inhaled Radon Decay Products in Human Bronchial Airway Bifurcations," *Health Physics*, **78**(2), 147-158 (2000).

90. Comer J.K., Kleinstreuer C., and Zhang Z., "Flow structures and particle deposition patterns in double-bifurcation airway models. Part 1. Air flow fields," *Journal of Fluid Mechanics*, **435**, 25-54 (2001).

91. Hofmann W., Bergmann R., and Báláshazy I., "Variability and Inhomogeneity of Radon Progeny Deposition Patterns in Human Bronchial Airways," *Journal of Environmental Radioactivity*, **51**, 121-136 (2000).

92. Hofmann W., Golser R., and Báláshazy I., "Inspiratory Deposition Efficiency of Ultrafine Particles in a Human Airway Bifurcation Model," *Aerosol Science and Technology*, **37**, 988-994 (2003).

93. Kim C.S., Fisher D.M., Lutz D.J., and Gerrity T.R., "Particle Deposition in Bifurcating Airway Models with Varying Airway Geometry," *Journal of Aerosol Science*, **25**(30), 567-581 (1994).

94. Yamada Y., Koizumi A., and Inaba J., "A New Method of Casting Human Respiratory Tract for Aerosol Deposition Studies," *Radiation Protection Dosimetry*, **79**, 269-272 (1998).

95. Zhang Y. and Finlay W.H., "Experimental Measurements of Particle Deposition in Three Proximal Lung Bifurcation Models with an Idealized Mouth-Throat," *Journal of Aerosol Medicine*, **18**(4), 460-473 (2005).

96. Zhang Z., Kleinstreuer C., and Kim C.S., "Aerosol Deposition Efficiencies and Upstream Release Positions for Different Inhalation Modes in an Upper Bronchial Airway Model," *Aerosol Science and Technology*, **36**, 828-844 (2002).

97. Zhang Z., Kleinstreuer C., Kim C.S., and Cheng Y.S., "Vaporizing Microdroplet Inhalation, Transport, and Deposition in a Human Upper Airway Model," *Aerosol Science and Technology*, **38**, 36-49 (2004).

VITA

Veera Rajesh Gutti was born in 1981 in Hyderabad, India. He received his high school education at Atomic Energy Junior College, Hyderabad, India. He obtained B.Tech in Chemical Engineering at the Osmania University, India in 2002. He obtained his M.S. degree in Nuclear Engineering (Health Physics emphasis) in 2005, and his Ph.D. in Nuclear Engineering in 2010 from the University of Missouri-Columbia.

His other experience includes one semester of post graduate diploma training in Plastics Engineering at CIPET, Hyderabad, India; radiation safety training at Radiation Safety Office, Environmental Health & Safety (EHS), University of Missouri-Columbia; and Co-op/internship with the Callaway Nuclear Power plant, Fulton, Missouri.

LIST OF PUBLICATIONS

PEER-REVIEWED JOURNAL PUBLICATIONS:

- S.R. Boddu, **V.R. Gutti**, R.M. Meyer, T.K. Ghosh, R.V. Tompson, S.K. Loyalka, "Gold, Silver, and Palladium Nanoparticle Generation, Collection, and Characterization Using a Spark Generator and a Thermophoretic Deposition Cell," *(Submitted to J. Nanoparticle Res.)*.
- M. P. Simones, **V. R. Gutti**, R. M. Meyer, S. K. Loyalka, "Aerosol Charge and Size Distribution Measurements: Carbon, Gold, Palladium and Silver Nanoparticles," *(Submitted to Nuclear Technology)*.
- S.R. Boddu, **V.R. Gutti**, R.M. Meyer, T.K. Ghosh, R.V. Tompson, S.K. Loyalka, "Carbon Nanoparticle Generation, Collection, and Characterization Using a Spark Generator and a Thermophoretic Deposition Cell," *Nuclear Technology (Accepted for Publication)*.
- **V.R. Gutti**, S.K. Loyalka, "Thermophoretic Deposition in a Cylindrical Tube: Computations and Comparison with Experiments," *Nuclear Technology,* **166**, 121-133 (2009).
- G.A. Johnson, **V.R. Gutti**, S.K. Loyalka, K.A. O'Beirne, S.K. Cochran, H.M. Dale, G.R. Kracke, "***Albuterol metered dose inhaler performance under hyperbaric pressures,***" *Undersea and Hyperbaric Medicine*, **36**(1), 55-63 (2009).

CONFERENCE PRESENTATIONS:

- **V. R. Gutti**, R. V. Tompson, S. K. Loyalka, "Localized Deposition Patterns of Molecular Phase Po-218 in Lung Bifurcations", HPS annual meeting, Providence, RI, June 2006.
- **V. R. Gutti**, R. V. Tompson, S. K. Loyalka, "Simulation of Molecular Phase Localized Deposition Patterns in Lung Bifurcations", ANS Transactions, June 2006.
- **V. R. Gutti**, L. Ross, W. H. Miller, T. K. Ghosh, "Development of a Chitosan Based Adsorbent for Arsenic Removal", ANS Transactions, June 2005.
- **V. R. Gutti**, S. Hasan, T. K. Ghosh, "Removal of Strontium from Aqueous Solutions using Fuller's Earth Beads", ANS Transactions, June 2004.